Large-eddy simulation of atmospheric flow over complex terrain

Bechmann, Andreas

Publication date:
2007

Document Version
Publisher's PDF, also known as Version of record

RISØ

Risø-PhD-thesis

Large-Eddy Simulation of Atmospheric Flow over Complex Terrain

Andreas Bechmann

Risø-PhD-28(EN)

Risø National Laboratory
Technical University of Denmark
Roskilde, Denmark
November 2006

DTU

Author: Andreas Bechmann
Title: Large-Eddy Simulation of Atmospheric Flow over Complex Terrain
Department: Wind Energy Department

This thesis is submitted in partial fulfilment of the requirements for the Ph.D. degree at the Technical University of Denmark (DTU)

Abstract (max. 2000 char.):
The present report describes the development and validation of a turbulence model designed for atmospheric flows based on the concept of Large-Eddy Simulation (LES). The background for the work is the high Reynolds number k - ε model, which has been implemented on a finite-volume code of the incompressible Reynolds-averaged Navier-Stokes equations (RANS). The k - ε model is traditionally used for RANS computations, but is here developed to also enable LES.
LES is able to provide detailed descriptions of a wide range of engineering flows at low Reynolds numbers. For atmospheric flows, however, the high Reynolds numbers and the rough surface of the earth provide difficulties normally not compatible with LES. Since these issues are most severe near the surface they are addressed by handling the near surface region with RANS and only use LES above this region. Using this method, the developed turbulence model is able to handle both engineering and atmospheric flows and can be run in both RANS or LES mode.
For LES simulations a time-dependent wind field that accurately represents the turbulent structures of a wind environment must be prescribed at the computational inlet. A method is implemented where the turbulent wind field from a separate LES simulation can be used as inflow. To avoid numerical dissipation of turbulence special care is paid to the numerical method, e.g. the turbulence model is calibrated with the specific numerical scheme used. This is done by simulating decaying isotropic and homogeneous turbulence. Three atmospheric test cases are investigated in order to validate the behavior of the presented turbulence model. Simulation of the neutral atmospheric boundary layer, illustrates the turbulence model ability to generate and maintain the turbulent structures responsible for boundary layer transport processes. Velocity and turbulence profiles are in good agreement with measurements. Simulation of the flow over the Askervein hill is also performed. Speed-up and turbulence intensities show good agreement with measurements, except 400m downstream of the hill summit where speed-up is underestimated. Flow over a cube in a thick turbulent boundary layer is the final test case. The turbulence model ability to capture the physics of the large separated region downstream of the cube is demonstrated. The turbulence model is, however, shown to have trouble with very large values of roughness.

Risø-PhD-28(EN)
November 2006

ISBN 87-550-3556-6

Contract no.:

Group's own reg. no.:

Sponsorship:

Cover :

Pages: 106
Tables: 20
References: 75

Information Service Department
Risø National Laboratory
Technical University of Denmark
P.O.Box 49
DK-4000 Roskilde
Denmark
Telephone +45 46774004
bibl@risoe.dk
Fax +45 46774013
www.risoe.dk

Acknowledgements

This thesis is submitted in partial fulfillment of the requirements for the Danish PhD degree at the Technical University of Denmark (DTU). The thesis documents the author's research carried out during the period of October 2004 to November 2006 at the Wind Energy Department, Risø National Laboratory and to a lesser extent at the Department of Mechanical Engineering, Technical University of Denmark (MEK/DTU). The work was carried out under the supervision of Prof. J.N. Sørensen (MEK/DTU), Prof. N.N. Sørensen, Senior Researcher J. Johansen and Prof. J. Mann (Risø). I would like to thank them for qualified supervision.

The CFD computations were made possible by the use of the Risø 240 nodes MARY PC-cluster, and the computational resources of the Danish Centre for Scientific Computing at MEK/DTU in Lyngby.

I would like to express my gratitude to my supervisors, Prof. N.N. Sørensen and Senior Researcher J. Johansen who gave me the opportunity to undertake the PhD program. I am very grateful for the support. Thank you for always having time to answer my questions. I would also like to thank Prof. J. Mann and my fellow students F. Zahle and J. Berg for many helpful discussions.

Last, but not least, thanks to my wife Dorthe for all the support and patience.

November 2006

Andreas Bechmann

Nomenclature

Abbreviations

ABL	Atmospheric Boundary Layer
$CDS2$	Second-order central difference scheme
$CDS4$	Fourth-order central difference scheme
CFD	Computational Fluid Dynamics
CFL	Courant-Friedrich-Levy-number
DES	Detached-Eddy Simulation
HT	The Askervein hill's highest point
LES	Large-Eddy Simulation
MM	Mixed model
MPI	Message Passage Interface
$PISO$	Pressure-Implicit with Splitting of Operators
$QUICK$	Quadratic upstream interpolation for convective kinetics scheme
$RANS$	Reynolds-Averaged Navier-Stokes
RS	The Askervein hill's reference site upstream
SGS	Subgrid-scales
SL	Surface Layer
SSM	Scale-similarity model
$TDMA$	Tri-Diagonal Matrix Algorithm
TKE	Turbulent kinetic energy
UDS	First-order upwind difference scheme
$URANS$	Unsteady RANS

Greek Letters

α	The Kolmogorov constant
α_B	Correlation coefficient for backscatter model
Δ	Cutoff length, filter width
δ_{ij}	Kronecker delta or identity tensor
ΔS	Speed-up ratio
Δt	Time step
Δx	Grid spacing in x-direction
Δy	Grid spacing in y-direction
Δz	Grid spacing in z-direction
ϵ	Total turbulent dissipation rate
Γ	Adiabatic lapse rate
κ	The von Karman constant
$\langle\tilde{\epsilon}\rangle$	Mean modeled turbulent dissipation rate
ν	Kinematic molecular viscosity
ν_T	Eddy viscosity
ω	Angular velocity of earth

Ω_i	Angular velocity vector of the earth's rotation
$\overline{\tau}$	Resolved shear stress
$\overline{\tau}_{ij}$	Resolved turbulent stress tensor
ϕ	Latitude
ϕ_ϵ	Dimensionless dissipation of turbulent kinetic energy
ϕ_k	Dimensionless turbulent kinetic energy
ϕ_m	Dimensionless wind shear
ρ	Density
σ_ϵ	Constant for turbulence model
σ_k	Constant for turbulence model
$\sigma_u, \sigma_v, \sigma_w$	Standard deviation in (x_1, x_2, x_3) directions
τ	Total shear stress
τ_0	Total wall stress
τ_{ij}	Unfiltered or full turbulent stress tensor
θ	Cross-isobaric angle
$\tilde{\epsilon}$	Modeled turbulent dissipation rate
$\tilde{\tau}$	Modeled shear stress
$\tilde{\tau}_{ij}$	Unresolved or SGS-stress tensor
ε_{ijk}	Permutation tensor

Roman Letters

$\langle B_\epsilon \rangle$	Mean energy backscatter
$\langle p \rangle$	Ensemble averaged pressure
$\langle u_i \rangle$	Ensemble averaged velocity vector
$\overline{f}_i$	Resolved body force vector
$\overline{G}$	Explicit spatial filter
$\overline{k}$	Resolved turbulent kinetic energy
$\overline{p}$	Resolved pressure
$\overline{S}$	Local resolved strain rate
$\overline{u}_i$	Resolved velocity vector, filtered (LES) Reynolds-ave.(RANS)
$\tilde{k}$	Subgrid turbulent kinetic energy
$\tilde{l}$	Length scale, switches between the RANS and LES length
$\tilde{v}$	Characteristic turbulent velocity scale
A	Similarity constant for geostrophic resistance laws
B	Similarity constant for geostrophic resistance laws
B_ϵ	Energy backscatter
C_D	Dimensionless drag coefficient
C_p	Pressure coefficient
c_p	Specific heat at constant pressure
C_Δ	Constant for turbulence model
$C_{\epsilon 1}$	Constant for turbulence model
$C_{\epsilon 2}$	Constant for turbulence model

C_μ	Constant for turbulence model
C_B	Constant for backscatter model
C_{DES}	Constant for DES model
C_s	Constant for Smagorinsky model
f	Frequency
f_c	Coriolis parameter
F_i	One point one-sided spectrum as function of wavenumber
f_i	Body force vector
$f_{C,i}$	Coriolis acceleration vector
G	Geostrophic wind
g	Gravitational acceleration
H	Height of computational domain
h	Height (or depth) of the boundary layer
h_c	Cube height
I	Turbulence intensity
k	Total turbulent kinetic energy
k_1, k_2, k_3	Wavenumbers in (x_1, x_2, x_3) directions
L	Length of computational domain
L_t	Length scale used in turbulence generator
l_{LES}	Characteristic turbulent length scale for LES
l_{RANS}	Characteristic turbulent length scale for RANS
M	Horizontal wind speed
M_g	Wind tunnel grid spacing
N	Number of computational cells
N_T	Number of time steps
N_x	Number of computational cells in x-direction
N_y	Number of computational cells in y-direction
N_z	Number of computational cells in z-direction
p	Local pressure, perturbation around hydrostatic pressure
p_∞	Reference pressure
Re	Reynolds number
S	Grid Stretching ratio
S_i	One point one-sided spectrum as function of frequency
S_{ij}	Strain rate tensor
T	Temperature
t	Time
T_{SGS}	Timescale characteristic for the SGS-scales
u_i'	Resolved velocity fluctuation
u, v, w	Unfiltered velocity components, w is in the vertical
u_*	Local characteristic velocity scale
u_0	Mean inlet velocity
u_g	Geostrophic wind in x-direction

u_h	Velocity at cube height
u_i	Unfiltered velocity vector, using Einstein notation
u_{*0}	Friction or shear velocity evaluated at the wall
u_{ref}	Reference velocity
v_g	Geostrophic wind in y-direction
W	Width of computational domain
x, y, z	Cartesian coordinates, z is the vertical coordinate
x_i	Position vector, using Einstein notation
z_0	Surface roughness height of momentum
z_1	Height of the first near-wall grid cell
z_{ml}	Distance from wall where model goes from RANS to LES

List of Figures

List of Tables

Contents

1 Introduction

1.1 Motivation and background

The wind properties throughout the atmospheric boundary layer (ABL) are important in many applications. Loads on buildings, dispersion of pollutants and agricultural production are just a few applications, which are dependent on accurate weather predictions. Accurate information on the wind is also crucial for wind engineers to accurately determine loads on wind turbines. Since, topographic features, such as hills, ridges and escarpments can greatly alter the the character of the wind, site-specific wind information is necessary.

Even though on-site wind measurements are preferred, computational wind simulations are often a great supplement to field experiments. Measurements obtained from field experiments are a result of many simultaneous effects and processes being superimposed and it can be difficult to isolate or focus on a specific process. For numerical simulations, however, the effect of changing a single parameter can easily be investigated. Furthermore, when on-site measurements are sparse, engineers must rely on computations. Therefore, is it important with a robust numerical simulation tool that can accommodate the complexity of atmospheric flows and provide accurate wind forecasts. The development of such a tool is the aim of this work.

This section starts with a short description of some of the fundamental processes occurring in the atmospheric boundary layer - meant only to give the most basic physical insight. Hereafter, the background for the present study is described, together with some general simplifications necessary to make numerical simulations of the ABL possible. Finally, an overview of the report is given.

The atmospheric boundary layer

With heights of around 500m the tallest structures of the world rise impressively towards the sky - reaching the lowest part of the atmosphere known as the atmospheric boundary layer (ABL). The ABL is the part of the atmosphere that is in direct vicinity of the earth's surface and most transport processes, e.g. of momentum or heat, happens in this layer. Due to the mechanisms of turbulence, responses to changes in surface characteristics are fast - of about an hour or less, and the influence of surface friction and heating is quickly transmitted to the entire ABL. Since turbulence is characteristic for the ABL, the top of the ABL is often defined as the height where turbulence disappears.

The height of the ABL and the scales of turbulence is greatly depended on the thermal stratification. During the day, surface heating drives large thermal motions, that steadily increases the boundary layer height - sometimes to heights of 3000m in the late afternoon. The stratification is said to be unstable. During the night, cooling of the surface results in suppression of the turbulent scales and the boundary layer height decrease to about 100m. The stratification is then stable. At times, often in late afternoon and during strong winds, turbulence is not generated by surface heating but is mainly mechanically generated (by the wind gradient). The stratification can then be said to be neutral. Due to heating and cooling of the air, both the ABL height and turbulent scales experiences strong diurnal variations.

At the top of the ABL, wind speed equals the wind speed of the free atmosphere (the geostrophic wind) and at the ground surface friction reduces the air speed to zero. Due to the balance of pressure, friction and Coriolis forces the wind speed and direction changes through out the ABL. At the bottom 10% of the ABL,

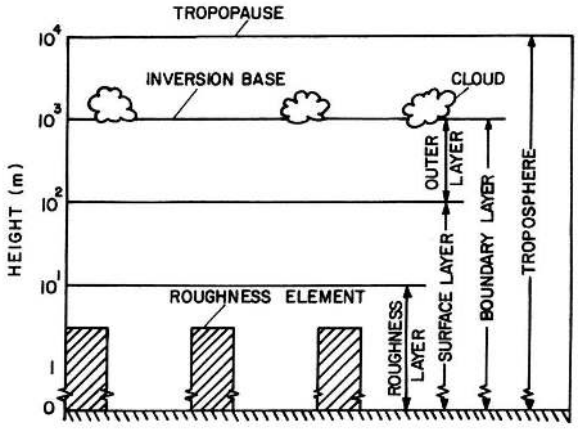

Figure 1. Schematic of the atmospheric boundary layer, with scales typical for near-neutral stability. (Figure is from Arya [2])

turbulent fluxes can be considered constant and Coriolis forces are unimportant - turning of the wind with height is here negligible. This layer is called the ***surface layer*** (SL). The SL is directly influenced by roughness elements like grass and trees, which covers the surface of the earth, and most structures of engineering interest are located in the surface layer. Above the SL lies the outer layer, which can be considered independent of the surface conditions but is influenced by the rotation of the earth. A schematic of the ABL under neutral conditions is shown on figure 1. For Additional reading about the ABL see [2, 23, 62]

Background for the present work

The present work is a collaboration between the Section of Fluid Mechanics at the Technical University of Denmark and the Wind Energy Department at Risø National Laboratory. At the Department of Wind Energy, the research topics connected to the atmospheric boundary layer are mostly related to wind turbines. These topics might be load prediction or siting of wind turbines in complex terrain. The present work is a direct evolution of the computational fluid dynamics (CFD) tools developed for numerical prediction of atmospheric flow over complex terrain.

The CFD code EllipSys3D developed by Michelsen [37][38] and Sørensen [56] is the fundament for this work. The EllipSys3D code was developed specifically to compute flow over terrain but is today used for a wide range of applications, e.g. for airfoil flows [6, 22, 58, 59]. The code is a finite-volume discretisation of the Reynolds averaged incompressible Navier-Stokes (RANS) equations and uses curvilinear coordinates that can accurately describe the terrain. When terrain simulations are performed, the turbulence is modeled by the high Reynolds number $k - \epsilon$ model [26].

The Ellipsys3D code is robust and has successfully been used for assessment of wind-potentials for several sites. The computations give estimates of the mean velocity and the mean level of turbulent kinetic energy at a location of interest. The flow is normally driven by a constant velocity profile at the computational boundaries and stratification is constant and assumed neutral. The scale of the terrain investigated is limited by the size of the computational domain. A standard domain might be about 1km in the vertical direction and about 5km in horizontal directions - the scales often denoted, microscales.

1.2 The present study

Design fatigue loading of wind turbines is traditionally determined from aeroelastic simulations, where a structural model is exposed to a synthetic generated wind field. Significant differences in wind turbine fatigue loading occur using different methods for generating the turbulent wind fields, which is why a realistic turbulent wind field containing realistic coherent structures is important. Since time dependent effects like wind gusts are important, ensemble averaged mean flow is insufficient for this kind of problem. Furthermore, wind turbines are often placed in hilly and complex terrain, which put great demand on the wind field generator.

If the EllipSys3D code is to handle transient problems, like wind gusts, further development is necessary - this is the aim of this work. More specifically the work is focused on developing a tool, which can deliver realistic turbulent wind fields of flow over complex terrain. The adopted approach, is to apply the technique of Large-Eddy Simulation (LES). Contrary to RANS, which give time-averaged wind fields, LES provide transient winds and resolves a large range of turbulent structures. Furthermore, though RANS correctly predicts the mean flow in many cases, it often fails in more complex flows where unsteady flow features dominate. The disadvantage of going from RANS to LES is, however, the dramatic increase in necessary computer resources. Despite computational cost, the timing for development of a LES code seems right. The rapid increase in computer power during the last 10 years, including the computational capacity of parallel computers, and the constant need for improved and physically detailed wind predictions, justifies this decision. Computational solutions does have deficiencies. But weather the variability of the results are larger than full-scale measurements is an interesting question. We believe that the reliability of computational solutions have reached a level close to full-scale measurements.

In order to numerically simulate atmospheric flows simplifications are necessary. In this work only cases of neutral stratification are considered i.e. the diurnal variations of heating and cooling of the earth's surface are not simulated. Furthermore, solving the flow-equations in a computational domain leads to approximate conditions at the domain boundaries. The rough surface of the earth is one example. Since the individual roughness elements cannot be resolved by a numerical mesh, the effect of roughness must be modeled. To do this we follow the methodology of the high Reynolds number $k-\epsilon$ model [26], which applies a wall-function in order to model surface roughness. The wall-function is implemented so that it handles both smooth and rough walls, which we characterize as industrial and atmospheric flows. Furthermore, effects like condensation and precipitation are not allowed in the present simulations.

The specific improvements to the existing solver, done in this work, lies in the development of a LES turbulence model. The model builds on the existing high Reynolds number $k-\epsilon$ model, and is constructed to enable both RANS and LES computations. More than providing transient wind data, better results are also expected in complex terrain. This owes to, that for RANS the turbulence is modeled as isotropic, while LES resolves the anisotropy of the turbulence. This work describes the development of a general purpose turbulence model, that can be used for both RANS and LES and is applicable for both Atmospheric and industrial flow. For a historical overview and the prospects of LES of wind over complex terrain we refer to Wood [71].

Overview

This report starts in chapter 2 by deriving the governing flow equations for both RANS and LES. The equations are derived from the Navier-Stokes equations and lead to a turbulent stress term, which need to be modeled - this is the well known closure problem.

Chapter 3 describes how turbulence modeling has been performed in this work. The classical high Reynolds number $k-\epsilon$ RANS model is modified so it can be changed into a LES model. When equilibrium between shear production and dissipation of turbulent kinetic energy exists, the model is shown to reduce to the well known Smagorinsky model [55]. In order to reduce numerical cost, a method is proposed, where the near-wall flow is solved using RANS. This RANS region is connected to the outer flow handled by LES in a similar way as Detached-Eddy Simulation (DES) proposed by Spalart et al. [61]. In order to improve results the chapter also presents a backscatter model.

Chapter 4 deals with different numerical aspects of simulating atmospheric flows using LES. First, the EllipSys3D code is shortly described. Here, aspects like the importance of choosing the right differencing scheme and numerical time step is explained. The boundary conditions used for LES simulations are then described. The methodology behind generation of transient inflow by running a precursor simulation is one example. The chapter ends by presenting how the computational grids are generated. Here, the effect of changing domain dimensions are investigated, and the computational cost of the precursor based on grid spacing is estimated.

Chapter 5 to 8 deals with the validation of the proposed turbulence model. Each of the test cases simulated are presented in separate chapters. The first validation case described in chapter 5, is simulation of decaying isotropic homogeneous turbulence. Simulation of decaying turbulence is necessary in order to calibrate the turbulence model, but also important when determining the solvers ability to capture the correct energy dissipation as a whole.

Chapter 6 considers wind simulation of the neutral atmospheric boundary layer over flat but rough terrain. Results from the proposed LES model are compared to the traditional $k-\epsilon$ RANS model. Special attention is made to insure that the calculated mean velocity profiles agree with the logarithmic profile found from similarity theory. The effect of applying the backscatter model is presented. Higher order statistics are also compared with similarity theory.

To evaluate the solvers ability to capture flow over topography two test cases are considered. The first case described in chapter 7, considers flow over the Askervein hill located at the Hebrides. The hill is a widely used test case, because it is a relatively isolated hill, where intensive field measurements under neutral conditions have been performed. Even though separation is observed on the lee side of the hill, hill slopes are small and the terrain is relative simple. Since it is difficult to find reliable data for complex terrain, boundary layer flow around a cube has also been selected. This is the topic of chapter 8. The flow around the cube is highly complex and is a good test case to validate the solvers ability to handle separated regions. Flow around a wall mounted cube has been investigated by several authors and good experimental measurements are available. Conclusions are found in chapter 9.

2 Governing Equations

This section introduces the governing flow equations and presents the notation used through the rest of the work. For the ease of reading all equations are stated in orthogonal coordinates even though the flow solver EllipSys3D [37, 38, 56] has been formulated in general curvilinear coordinates. The Navier-Stokes equations are first presented, followed by some assumptions of the flow to be modeled. The section then shows how Reynolds-averaging and spatial filtering of the Navier-Stokes (NS) equations, that is necessary for numerical simulations, lead to the well known closure problem for the turbulent stresses.

2.1 Navier-Stokes equations

Application of Newton's second law to an fluid element of a given mass together with the constitutive relation for stress in a newtonian fluid yield the well-known Navier-Stokes equations. The Navier-Stokes equations (1) and the continuity equation (2) for an incompressible fluid of constant density, ρ, can be stated in Cartesian coordinates as,

$$\frac{\partial u_i}{\partial t} + \frac{\partial (u_i u_j)}{\partial x_j} = -\frac{1}{\rho}\frac{\partial p}{\partial x_i} + \frac{\partial}{\partial x_j}\left[\nu\left(\frac{\partial u_i}{\partial x_j} + \frac{\partial u_j}{\partial x_i}\right)\right] + f_i, \tag{1}$$

$$\frac{\partial u_i}{\partial x_i} = 0, \tag{2}$$

where the Einstein summation notation is used. x_i is the Cartesian coordinate system ($i = 1, 2$ or 3 for x,y or z) with x and y axis in the horizontal and z axis in the vertical direction. u_i denotes the velocity field ($i = 1, 2$ or 3 for u,v or w), p is the pressure and ν is the kinematic molecular viscosity. f_i represents body forces, which act on the mass of the fluid.

Thermal stratification

The atmospheric boundary layer (ABL) considered is assumed to be in hydrostatic equilibrium, i.e. the mean pressure decreases with height following the hydrostatic equation,

$$\frac{\partial p}{\partial z} = -\rho g, \tag{3}$$

where g is the acceleration due to gravity. If an air element of a given mass is lifted upward in the atmosphere its pressure will decrease following (3) and as response its temperature will decrease. If the air element is lifted rapidly enough to avoid heat exchange with the surrounding environment, its temperature, T, will drop following the ***adiabatic lapse rate*** (Γ),

$$\Gamma = -\left(\frac{\partial T}{\partial z}\right)_{ad} = \frac{g}{c_p}, \tag{4}$$

where c_p is the specific heat at constant pressure. Under dry conditions Γ amounts to nearly 10 Kkm^{-1}. When the temperature gradient of the atmosphere differs from Γ, initiated motions tend to be damped or enhanced and the thermal stratification is said to be stable ($\partial T/\partial z < \Gamma$) or unstable ($\partial T/\partial z > \Gamma$). Thermal stratification can greatly affect the flow. In this work, however, only neutral conditions are considered, i.e. the temperature decreases with height following Γ.

During overcast conditions and strong winds the ABL can often be considered neutral [62]. Since only neutral conditions are considered the gravitational force has been omitted from (1). It has been absorbed into the pressure term,

$$\frac{\partial p}{\partial z} = \frac{\partial \hat{p}}{\partial z} + \rho g, \tag{5}$$

and p represents the perturbation around the hydrostatic pressure (3). In section 3, the pressure is further modified by addition of two-thirds times the modeled turbulent kinetic energy. Density variation due to temperature fluctuation around Γ, which may result in gravity waves are not considered, i.e. the density is constant.

Coriolis forcing

The effect of the Earth's rotation is often not observable and can be neglected when considering scales much smaller than the global scales. When simulating the atmospheric boundary layer, however, the effect should be considered. The Coriolis force appears when the equations of motion are considered in a non-inertial coordinate system. Since we consider the equations of motion in a moving frame of reference given by the rotation of the earth the Coriolis force is required. The Coriolis force per unit mass is given by, $-2\varepsilon_{ijk}\Omega_j u_k$, where Ω_j is the angular velocity vector of the earth's rotation and u_i is the velocity in the rotating system. The components of Ω_j are given by $[0, \omega\cos(\phi), \omega\sin(\phi)]$, where ϕ is the latitude and ω is the angular velocity of earth (ω= 2π radians/$24h = 7.27\times10^{-5}s^{-1}$) [62]. By defining the ***Coriolis parameter***, $f_c = 2\omega\sin(\phi)$, the Coriolis acceleration is often rewritten,

$$f_{C,\,i} = f_c\varepsilon_{ij3}u_j, \tag{6}$$

where the Coriolis acceleration in the vertical direction has been omitted. Throughout, the traditional value $f_c = 10^{-4}s^{-1}$ is used corresponding to a latitude of $44°N$ (Paris, France$\sim 48°N$ and Portland, Oregon, U.S.$\sim 45°N$).

2.2 Filtered & Reynolds-averaged NS-equations

The Navier-Stokes equations (1) describe all flow structures at all time and length scales. The largest structures of the turbulent flow scale with the geometry considered e.g. the boundary layer height ($\sim 10^3m$), while the smallest are the size of the dissipative eddies ($\sim 10^{-3}m$)[62]. Even though the NS-equations give a complete flow description, sometimes only the physics of the largest turbulent structures or of the time-averaged flow field is of interest. This is often the case for computational fluid dynamics (CFD). The wide range of scales of a real turbulent flow makes numerical simulations, which resolves all time and length scales impossible. The number of computational cells necessary, combined with the small numerical time step required to capture the fastest turbulent structures, simply makes computational cost too high. Therefore, CFD requires a set of flow equations that can be solved in reduced time.

To make numerical simulation feasible two approaches are used in the present work. The first approach is to apply a spatial filter to the NS-equations (1), resulting in equations that only governs the largest turbulent structures. These equations are solved in Large-Eddy simulation (LES) [28, 35, 46, 54]. The second approach is to apply the Reynolds decomposition technique followed by time-averaging of the NS-equations, thereby getting the Reynolds-averaged Navier-Stokes (RANS) equations, which can be solved in reduced computer time. For both methods a

stress term appears that need to be modeled. This is the well known closure problem, which is the topic of Chapter 3. Here we derive the two sets of equations.

Spatial filtered Navier-Stokes equations

The idea behind LES is to only compute the large energy-carrying turbulent structures exactly, while the effect of the smallest scales are modeled [54]. This limits the computational cost because the numerical mesh can be coarsened. The small unresolved scales are likely to have a homogeneous and universal character and their effect on the large scales is hoped to be modeled simply. To separate the large resolved scales from the small unresolved scales a filtering operation [27] is applied to Navier-Stokes equations (1):

$$\overline{u}(\mathbf{x},t) = \int u(\xi,t)\overline{G}(\mathbf{x}-\xi)d^3\xi \tag{7}$$

An overbar denotes the filtered variable and $\overline{G}$ is a one dimensional filter that is centered about the point $\xi = \mathbf{x}$. The scale separation is determined by the choice of filter. A commonly used filter is the box filter also called the top-hat filter. If we define a cutoff length, Δ, the box filter can be written as:

$$\overline{G}(x-\xi) = \begin{cases} \frac{1}{\Delta} & \text{if } |x-\xi| \leq \frac{\Delta}{2} \\ \\ 0 & \text{otherwise} \end{cases}$$

With the box filter, the filtered variable $\overline{u}(x,t)$ is simply the average value of $u(x,t)$ over the interval $(x-\Delta/2, x+\Delta/2)$ or over a volume in three dimensions. Instead of applying an explicit filter as described, however, we interpret a finite-volume discretisation of the flow equations on a numerical mesh as an implicit filter tied to the numerical resolution (see section 4.2 p. 22 for discussion) and associates the computed velocity field with a filtered velocity. Turbulent scales smaller than the numerical mesh spacing are unresolved, whereas, the larger scales are resolved. This is similar to using a box filter when Δ is equal to the mesh spacing. Since the implicit filter applied scale with the local spacing of the computational mesh, we specify the cutoff length locally as the maximum mesh spacing over the three directions:

$$\Delta = max(\Delta x, \Delta y, \Delta z) \tag{8}$$

Since the spatial filter is fixed to the numerical grid spacing we denote the flow structures, which are unresolved, ***subgrid-scales (SGS)***. Applying the filtering operation to the NS-equations the filtered flow equations appear,

$$\frac{\partial \overline{u}_i}{\partial t} + \frac{\partial(\overline{u}_i\overline{u}_j)}{\partial x_j} = -\frac{1}{\rho}\frac{\partial \overline{p}}{\partial x_i} + \frac{\partial}{\partial x_j}\left[\nu\left(\frac{\partial \overline{u}_i}{\partial x_j} + \frac{\partial \overline{u}_j}{\partial x_i}\right) + \frac{1}{\rho}\tilde{\tau}_{ij}\right] + \overline{f}_i, \tag{9}$$

$$\frac{\partial \overline{u}_i}{\partial x_i} = 0, \tag{10}$$

where tilde is used for unresolved variables. Since $\overline{u_i u_j} \neq \overline{u}_i\overline{u}_j$ the filtering process result in an stress term that needs to be modeled:

$$\tilde{\tau}_{ij} = -\rho\left(\overline{u_i u_j} - \overline{u}_i\overline{u}_j\right) \tag{11}$$

The extra term, which we denote the SGS-stresses, represents the effect from the small unresolved turbulent scales on the large resolved scales. If the variables

are split into resolved and unresolved parts ($u = \overline{u} + \tilde{u}$), the SGS-stress tensor (11) may be decomposed into a sum of various terms (see Leonard [27]), which can be modeled separately. We do not distinguish between these components but model the SGS-stresses as a whole, without splitting it into parts.

Reynolds-averaged Navier-Stokes equations

The second approach adopted to make numerical simulations feasible, is to solve the Reynolds-averaged Navier-Stokes equations (RANS). The RANS-equations are derived from the standard NS-equations (1) by decomposing the variables into time averaged and fluctuating components followed by time-averaging. Even though time-averaging is performed, the transient term of the NS-equations is retained. By doing this it is possible to use the RANS-equations to predict transient behaviors of flows, when instationarities are on a large timescale compared to the averaging time, T. This is sometimes denoted URANS (Unsteady RANS) but is here just denoted RANS. We also use the LES-notation for the RANS variables so that time averaged variables are denoted by an overbar, while unresolved fluctuating components are marked by a tilde. This is also called the Reynolds decomposition technique:

$$u = \overline{u} + \tilde{u} \tag{12}$$

$$\overline{u\left(t\right)} = \frac{1}{2T}\int_{-T}^{T} u\left(t+t'\right)dt' \tag{13}$$

Applying the Reynolds decomposition (12) to the NS-equations and performing the time-averaging (13) one obtains the RANS equations, which are similar to the LES equations (9). The averaging process produces a stress term like the SGS-stresses in LES but in RANS-terminology these stresses are traditionally denoted Reynolds-stresses. Unlike the SGS-stresses, which are functions of the local flow states and vanishes with decreasing filter width (8), the Reynolds-stresses represent large scales properties of the flow. Numerically, however, the spatial filtered equations of LES and the RANS-equations are identical and the only difference occur through the turbulent stress term (11), which is modeled differently in the two approaches.

Mean-field Navier-Stokes equations

Even if the results from RANS and LES are unsteady, one is often interested only in the purely time averaged flow. Therefore a variable, f, can also be represented as ensemble averaged denoted by $\langle f \rangle$. If the variable is statistically stationary in time and ergodic this value is equal to the time averaged value for $T \to \infty$. A resolved component, $\overline{u}$, can therefore be split into an ensemble averaged component and a resolved fluctuation, u', with respect to this average, by:

$$\overline{u} = \langle u \rangle + u' \tag{14}$$

$$\langle u \rangle = \lim_{T\to\infty} \frac{1}{2T}\int_{-T}^{T} \overline{u}\left(t+t'\right)dt' \tag{15}$$

An instantaneous quantity of a statistical steady flow, $u_i(x_i, t)$, can thus be decomposed into an ensemble averaged component, $\langle u_i \rangle$, a resolved component,

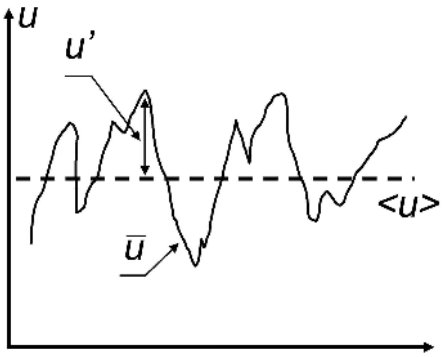

Figure 2. A LES- and RANS-variable can be decomposed into the shown components. The turbulent fluctuation, $\tilde{u}$, that need to be modeled, is not shown.

$\overline{u}_i(x_i,t)$, a resolved fluctuation, $u_i'(x_i,t)$, and an unresolved turbulent fluctuation, $\tilde{u}_i(x_i,t)$ (see figure 2),

$$u = \overline{u} + \tilde{u} = \langle u \rangle + u' + \tilde{u} \tag{16}$$

Applying the decomposition (14) to the filtered/Reynolds-averaged NS-equations (9) and performing the time-averaging (15) we end up with the mean field NS-equations:

$$\frac{\partial \langle u_i \rangle \langle u_j \rangle}{\partial x_j} = -\frac{1}{\rho}\frac{\partial \langle p \rangle}{\partial x_i} + \frac{\partial}{\partial x_j}\left[\nu\left(\frac{\partial \langle u_i \rangle}{\partial x_j} + \frac{\partial \langle u_j \rangle}{\partial x_i}\right) - \langle u_i' u_j' \rangle + \frac{1}{\rho}\langle \tilde{\tau}_{ij} \rangle\right] + \langle f_i \rangle \tag{17}$$

From this equation it is seen that the total turbulent stress,τ, consists of a resolved part, $\overline{\tau}$, and an unresolved part, $\tilde{\tau}$:

$$\overline{\tau}_{ij} = -\rho u_i' u_j', \tag{18}$$

$$\tilde{\tau}_{ij} = -\rho\left(\overline{u_i u_j} - \overline{u}_i \overline{u}_j\right), \tag{19}$$

For RANS simulations most of the turbulent stress is unresolved, whereas LES resolves the most.

2.3 Closure

The governing equations were presented for both time-averaged and spatial filtered flows (the RANS- and LES-equations). Instead of applying an explicit spatial filter to the NS-equations the numerical discretisation onto a computational grid was interpreted as an implicit filter with a characteristic scale, Δ. Because no distinction between filtered and time-averaged quantities was made, it was argued that the two set of equations are identical except for the turbulent stresses. These need to be modeled differently for the two approaches.

3 Turbulence Modeling

The interaction between the resolved turbulent scales and the unresolved scales in LES happens through the turbulent stresses (11), which need to be determined through modeling. For both LES and RANS we denote this turbulence modeling or simply SGS-modeling. SGS-modeling is subject to intense research and new approaches are constantly being developed. The objective here is not to provide a complete overview of ongoing research, but instead to describe how the SGS-modeling has been performed in this work and provide some physical understanding of the methodology.

The wide variety of turbulence models for LES have arisen because solutions are sensitive to the choice of model when unresolved motions are not conspicuously weaker than the resolved motions. This is often the case near walls, where the dominant turbulent structures are small compared to the numerical grid. Away from walls, where the scales of the main energy carrying structures are large compared to the numerical grid and most turbulent kinetic energy is resolved, the LES-solution is relative insensitive to choice of SGS-model. To perform a full LES of wall-bounded flows at high Reynolds numbers, the near-wall grid resolution need to be refined in all directions to resolve the important near-wall flow structures. Because of the high grid requirements, most flows of engineering interest are computationally too costly for a full LES [61]. For RANS computations, however, the mesh requirements are smaller - the mesh only needs to be refined in the wall-normal direction. Generally RANS handles boundary layer flow well, even on relatively coarse computational meshes.

To avoid the high computational costs of a full LES, we adopt an approach where the near-wall region is solved using RANS. This inner RANS-layer acts as wall model for the outer flow away from the wall, handled by LES. Approaches where the inner layer is solved using a different set of equations from the outer layer have been adopted by several authors [4, 15, 61], who often refer to the methods as hybrid two-layer approaches or zonal approaches. Here we show how the standard high Reynolds number $k-\epsilon$ RANS model [26] can be changed to a LES-model simply by changing a turbulent length scale. It is then showed how the RANS formulation can be used as wall model for the outer flow away from the wall handled by the LES. This technique is similar to the well known Detached-eddy simulation (DES) proposed by Spalart et al. [61]. To improve results in the transition region between RANS and LES a backscatter model is also presented.

Energy transfer

Taking a first glance at a turbulent flow, the behavior seems random and chaotic. If one takes a closer look, however, rotational flow structures (turbulent eddies) are observed, with a wide range of length and time scales. The largest eddies are generated and aligned in a preferred direction dictated by the mean flow and are therefore highly anisotropic. They contain the most turbulent kinetic energy. Because of velocity gradients and vortex stretching the large turbulent eddies are distorted and energy is transferred to smaller eddies. This constant transfer of energy to smaller and smaller eddies is termed the ***energy cascade*** [52]. As the eddies decrease in size they tend to loose the directionality of the larger eddies and they become isotropic. When the turbulent eddies become sufficiently small viscous effect become important and the energy is removed by viscous dissipation. Between the large energy carrying scales, which are mostly controlled by inviscid processes, and the smallest scales influenced by viscosity, lies a range only influenced by the cascade process. This range is called the ***inertial subrange***.

The energy cascade described indicates that energy is only transferred from large to small scales, the so-called forward scatter. In reality there is also a transfer of energy from small to large scales denoted backscatter, which can be important. In the following section the modeling of forward and backward energy transfer will be handled separately.

3.1 Eddy-viscosity concept

For a well resolved LES the unresolved scales should be small and only carry little turbulent energy. In a spectral sense the unresolved scales are usually required to be located in the inertial subrange, i.e. the unresolved scales should be dissipative in nature. The main role of a SGS-model is therefore to remove energy from the resolved scales, and to mimic the energy drain associated with the energy cascade.

Many SGS-models follow the Boussinesq concept [7] where the SGS-stresses are assumed to be the product of the fluid strain and an eddy-viscosity, ν_T. Turbulent transport of momentum is thereby regarded in an analogous way to molecular transport, with small scale eddies playing the role of molecules and the correlation length having the role of the mean-free-path. This concept of Boussinesq is adopted,

$$\tilde{\tau}_{ij} = 2\rho\nu_T\overline{S}_{ij} + \frac{\delta_{ij}}{3}\tilde{\tau}_{kk}, \tag{20}$$

$$\overline{S}_{ij} = \frac{1}{2}\left(\frac{\partial\overline{u}_i}{\partial x_j} + \frac{\partial\overline{u}_j}{\partial x_i}\right), \tag{21}$$

where $\overline{S}_{ij}$ is the strain rate tensor. This defines the eddy-viscosity, ν_T, which in contrast to molecular viscosity is a property of the turbulent flow and not the fluid itself. The eddy-viscosity concept is completely dissipative - it does not allow backscatter of energy from the small to the large scales (the eddy-viscosity is always positive in this work). The technique of modeling the energy transfer between subgrid-scales and resolved scales using the concept of Boussinesq is often denoted functional modeling. Another approach is structural modeling, where the SGS-stress tensor (11) is modeled directly without prior knowledge of the interaction between unresolved and resolved scales. Some of the best known structural models are the scale-similarity model (SSM) and the mixed model (MM) of Bardina et al. [5].

When (20) is used the turbulence is assumed isotropic. This assumption is not valid for the large turbulent structures of a flow, which often have a preferred direction dictated by the mean flow. However, as the turbulent scales considered become smaller the anisotropy is eventually lost and the scales can be considered isotropic. To perform a well resolved LES all the large and energy-carrying turbulent structures should be simulated and only the small isotropic scales should be modeled. It is generally accepted that the details of the SGS-model is of minor importance once the grid scale is small compared to the main energy carrying turbulent scales.

Inserting the expression for the eddy viscosity (20) into the filtered or Reynolds-averaged Navier-Stokes equations (9) we end up with the following equation:

$$\frac{\partial\overline{u}_i}{\partial t} + \frac{\partial(\overline{u}_i\overline{u}_j)}{\partial x_j} = -\frac{1}{\rho}\frac{\partial\overline{p}}{\partial x_i} + \frac{\partial}{\partial x_j}\left[(\nu+\nu_T)\left(\frac{\partial\overline{u}_i}{\partial x_j} + \frac{\partial\overline{u}_j}{\partial x_i}\right)\right] + \overline{f}_i, \tag{22}$$

where the term $\delta_{ij}\tilde{\tau}_{kk}/3$ has been absorbed into the pressure term.

By applying the eddy-viscosity concept the equations of motion have been closed and only a model for the eddy-viscosity is needed. The idea of an eddy-viscosity

is the most frequent way of modeling the turbulent stresses for both RANS and for LES-solvers.

3.2 $k-\epsilon$ eddy-viscosity model

RANS

In order to obtain the eddy-viscosity a technique is necessary for both LES and RANS simulations. For RANS simulations we use the classical high Reynolds number $k-\epsilon$ model [26], which is a fine-tuned model that is widely used for atmospheric flow. Here we present this model.

Based on dimensional grounds the eddy-viscosity may be described by the product of a length scale ($\tilde{l}$) and a velocity scale ($\tilde{v}$). Determining the two scales, which must be characteristic for the modeled turbulence is the essence of turbulence modeling. In atmospheric boundary layer simulations the characteristic turbulent velocity scale $\tilde{v}$ is often determined from the turbulent kinetic energy (TKE). This is commonly seen in both LES e.g. the 1.5-order TKE closures [16, 40] and RANS approaches such as the $k-\epsilon$ model. The total turbulent kinetic energy, k, consists of a resolved part, $\overline{k}$, and a subgrid part $\tilde{k}$,

$$\overline{k} = u_i' u_i'/2, \tag{23}$$

$$\tilde{k} = \left(\overline{u_i u_i} - \overline{u}_i \overline{u}_i\right)/2 = -\frac{1}{\rho}\tilde{\tau_{ii}}/2, \tag{24}$$

and the characteristic velocity scale is determined from the unresolved subgrid part (fluctuating part), $\tilde{v} = \tilde{k}^{1/2}$. Thereby the eddy-viscosity is proportional to $\nu_T \propto \tilde{k}^{\frac{1}{2}}\tilde{l}$.

The length scale $\tilde{l}$ should also be characteristic for the turbulence that need to be modeled. In LES only scales smaller than the filter scale applied need modeling, whereas in RANS the turbulence parameterizations encompasses all turbulent length scales - in RANS $\tilde{l}$ represents a macroscale of turbulence. The standard two-equation $k-\epsilon$ model calculates the eddy viscosity by using a length scale constructed by $\tilde{k}$ and $\tilde{\epsilon}$, where $\tilde{\epsilon}$ is the rate of dissipation of the modeled turbulent kinetic energy,

$$l_{RANS} = \frac{\tilde{k}^{3/2}}{\tilde{\epsilon}}, \tag{25}$$

$$\nu_T = C_\mu \frac{\tilde{k}^2}{\tilde{\epsilon}}, \tag{26}$$

where C_μ is a model constant. $\tilde{k}$ and $\tilde{\epsilon}$ are not known but are determined by solving two transport equations. The derivation of these equations is not given here but for non-buoyant flow they have the following form:

$$\frac{\partial \tilde{k}}{\partial t} + \frac{\partial}{\partial x_j}(\overline{u}_j \tilde{k}) - \frac{\partial}{\partial x_j}\left[\left(\nu + \frac{\nu_T}{\sigma_k}\right)\frac{\partial \tilde{k}}{\partial x_j}\right] = \nu_T |\overline{S}|^2 - \tilde{\epsilon} \tag{27}$$

$$\frac{\partial \tilde{\epsilon}}{\partial t} + \frac{\partial}{\partial x_j}(\overline{u}_j \tilde{\epsilon}) - \frac{\partial}{\partial x_j}\left[\left(\nu + \frac{\nu_T}{\sigma_\epsilon}\right)\frac{\partial \tilde{\epsilon}}{\partial x_j}\right] = C_{\epsilon 1}\frac{\tilde{\epsilon}}{\tilde{k}}\nu_T |\overline{S}|^2 - C_{\epsilon 2}\frac{\tilde{\epsilon}^2}{\tilde{k}} \tag{28}$$

σ_k, σ_ϵ, $C_{\epsilon 1}$ and $C_{\epsilon 2}$ are model constants, which need to be determined and $\overline{S}$ is the local strain rate defined by $\overline{S} = (2\overline{S}_{ij}\overline{S}_{ij})^{1/2}$.

LES

To envision a transition from RANS to LES the turbulent length scale need to be modified for the turbulence model to encompass such change. For LES-codes the turbulent length scale is tied to the filter width. In deriving the filtered Navier-Stokes equations (9) the filter width was assumed to scale with the spacing of the computational mesh, Δ (see equation 8). Δ is therefore a characteristic length scale when performing LES. We define the characteristic turbulent length scale for LES as,

$$l_{LES} = C_\Delta \Delta, \tag{29}$$

where C_Δ is a model constant, similar to C_{DES} used in DES [61]. Following the methodology used by Travin *et al.* [69] the LES length scale is incorporated into the turbulence model by modifying the dissipative term of the $\tilde{k}$-equation (27) that now reads:

$$\frac{\partial \tilde{k}}{\partial t} + \frac{\partial}{\partial x_j}(\overline{u}_j \tilde{k}) - \frac{\partial}{\partial x_j}\left[\left(\nu + \frac{\nu_T}{\sigma_k}\right)\frac{\partial \tilde{k}}{\partial x_j}\right] = \nu_T |\overline{S}|^2 - \frac{\tilde{k}^{3/2}}{\tilde{l}}, \tag{30}$$

where $\tilde{l}$ is either l_{RANS} or l_{LES}. By switching between the RANS and LES length scales it is possible to switch between a LES-model and a RANS-model in a very simple manner. The eddy viscosity will still be determined by (26) so it is necessary to solve the $k-\epsilon$-equations for both LES and RANS. When doing LES (i.e. $\tilde{l} = l_{LES}$) the k-ϵ-equations adapt to the length scale so that $\tilde{k}^{3/2}/\tilde{\epsilon} \propto l_{LES}$.

The SGS-model is easily implemented numerically, and we will now show that it reduces to a Smagorinsky-like model at equilibrium. The well known Smagorinsky model [55] is derived from the hypothesis of balance between shear production and dissipation of turbulent kinetic energy and reads,

$$\nu_T = (C_s \Delta)^2 |\overline{S}|, \tag{31}$$

where C_s is a model constant. For this model the characteristic turbulent length and velocity scales can be expressed by $\tilde{l} = C_s\Delta$ and $\tilde{v} = \tilde{l}|\overline{S}|$. If the unresolved scales are located in the inertial subrange it can be shown that $C_s \simeq 0.17$ [30]. A problem with the Smagorinsky model is however that C_s is not a constant but need adjustment for different flows. Many workers prefer $C_s = 0.1$.

Unlike the Smagorinsky model the proposed model explicitly solves the TKE-equation so no equilibrium assumptions between shear production and dissipation is needed. To compare with the Smagorinsky model however, we assume equilibrium, by equating the production and dissipation term of the kinetic energy equation (27):

$$\tilde{\epsilon} = \nu_T |\overline{S}|^2 \tag{32}$$

Using (32) and (26) together with (33) (an approximate expression found from simulations) the Smagorinsky model is recovered:

$$\tilde{\epsilon} \approx \frac{\tilde{k}^{3/2}}{l_{LES}} \frac{C_{\epsilon 1}}{C_{\epsilon 2}} \tag{33}$$

$$\nu_T = (\Delta C_s)^2 |\overline{S}| \approx \left(\Delta C_\Delta C_\mu^{3/4} \frac{C_{\epsilon 2}}{C_{\epsilon 1}}\right)^2 |\overline{S}| \tag{34}$$

The presented LES model has one new model constant C_Δ. The constant need to be determined so that the SGS-model dissipates energy at a proper level. In chapter 5 (p. 32) C_Δ is determined by simulation of decaying homogeneous isotropic turbulence. In chapter 6.3 (p. 45) numerical simulations show that the SGS-model behaves like a Smagorinsky model.

3.3 Wall-layer modeling

For a well resolved LES the modeled SGS-stresses should only contribute a small fraction of the total turbulent stresses (11,18). The grid-resolution requirements for a properly resolved LES has been analyzed by several authors e.g. Chapman [12]. Boundary layer flows can in general be divided into an inner near-wall region, where viscous effects are important, and an outer region away from the wall. The resolution requirements of the outer region is relatively small and is essentially independent of Reynolds number. The inner-layer, however, is much more demanding - resolving all the small inner-layer eddies at high Reynolds number is simply too computationally demanding. Because of the computational cost, modeling of the inner-layer is of great importance for LES of high Reynolds number flows. Furthermore, for atmospheric boundary layer flows the wall is not smooth but consists of roughness elements. A computational mesh, which resolves all individual roughness elements of a rough wall, is impossible. Ultimately, we must choose a technique where the calculation of the near-wall flow is abandoned. Instead it is necessary with an "off the wall" boundary condition, which relates the dynamics of the inner wall-layer to some generalized law-of-the-wall. In RANS these are called "wall functions".

An overview of the different approaches for applying wall-layer models in LES can be found in [44]. In general two methods can be adopted. The first approach is to simply relate the wall stress, τ_0 (35), to the tangential velocity at the first near-wall node through a wall function. The wall stress or the total vertical flux of horizontal momentum is defined by,

$$\tau_0 = [\tau_{13}^2 + \tau_{23}^2]_0^{1/2} \tag{35}$$

$$\tau_{13} = \tilde{\tau}_{13} + \overline{\tau}_{13} \tag{36}$$

$$\tau_{23} = \tilde{\tau}_{23} + \overline{\tau}_{23} \tag{37}$$

where subscript 0 denotes that the values are evaluated at the surface (or the first computational cell from the surface). When wall functions are employed directly to LES, the first computational cell must be large so that the effect of the near-wall eddies can be represented in an averaged sense representative of the wall function. The first grid point is also placed outside the viscous sub-layer. In this layer viscous effects can be ignored and dimensional analysis, where the momentum flux is considered constant with height and variations in the flow direction are negligible, gives the well-known logarithmic velocity profile law for the mean velocity profile over rough surfaces,

$$\frac{u}{u_{*0}} = \frac{1}{\kappa} \ln\left(\frac{z}{z_0}\right), \tag{38}$$

where

$$u_{*0}^2 = \tau_0/\rho, \tag{39}$$

z_0 is the surface roughness height of momentum, κ is the von Karman constant equal to 0.40 and u_{*0} is the characteristic velocity scale of the surface-layer - the so-called friction velocity. Using the wall-law (38), surface stress can be related to the tangential velocity. A problem with the wall-function approach is that the assumption of local stress equilibrium is not valid for flows with separation. Without *a priori* knowledge of the flow, however, wall-functions can not be avoided.

The second approach for wall-layer modeling is to solve the RANS equations or simplified versions of them in the inner layer and use this solution as boundary condition for the outer-flow calculation. The main advantage is that the use of wall-function can be avoided for flow over smooth walls. The idea of modeling the near-wall structures altogether using unsteady RANS and coupling this with LES in an outer region is often denoted hybrid LES-RANS methods or zonal approaches [4, 15, 61].

We adopt a hybrid LES-RANS approach where the $k-\epsilon$ RANS model is solved in the near-wall region. This idea is similar to Nikitin et al. [42]. The RANS-layer acts as wall-model for the outer flow handled by LES. Since we want to be able to simulate flow over rough terrain the $k-\epsilon$ RANS model used employs the log-law (38) as wall-function. The log-law is implemented so that it can be used for flow over rough and smooth walls [56]. The advantages of solving the RANS-equations near the wall instead of directly employing a wall function is that a greater part of the mean velocity profile is resolved. If the near-wall flow was handled by LES an advanced SGS-model capable of representing virtually all of the near-wall turbulent stresses would be needed. Furthermore, LES do not handle near-wall computational cells of very high aspect ratio well - this is not an issue for RANS. By handling the near-wall region with RANS a simple turbulence model can be used and a greater part of the mean near-wall velocity profile can be resolved. Furthermore, the log-law is developed for time-averaged flow, why it seems natural to solve the RANS-equations near the wall.

Since the only difference between the $k-\epsilon$ RANS model and the presented $k-\epsilon$ LES model is the turbulent length scale used in the turbulence model, changing between the two methods is very simple. The switch from RANS to LES is controlled by the turbulent length scales using a universal switch, similar to the one used in DES [69]:

$$\tilde{l} = \min\left(l_{RANS}, l_{LES}\right) = \min\left(\frac{\tilde{k}^{3/2}}{\tilde{\epsilon}}, C_\Delta \Delta\right) \tag{40}$$

The model is solved on a single grid and the turbulent length scale is the only parameter that separates the RANS region from the LES region. The switch from RANS to LES is locally determined with no wall distance criteria. Near the wall l_{RANS} is smaller than l_{LES} and a RANS region is generated. Away from the wall l_{LES} is small and the model switches to LES (see figure 3). In the RANS region the logarithmic law-of-the-wall (38) is used to determine the wall stress based on the instantaneous tangential velocity of the first off the wall grid-point. Since the position of the wall of a rough surface is unknown the logarithmic law is used down to $z/z_0 = 1$ where the tangential velocity is zero.

The model changes from RANS to LES when the two turbulent length scales are equal. In the surface-layer where the mean velocity profile is generally accepted to follow the logarithmic profile (38) the RANS length scale increases linearly with the distance to the wall:

$$l_{RANS} = \frac{\tilde{k}^{3/2}}{\tilde{\epsilon}} \simeq \frac{\kappa z}{C_\mu^{3/4}} \tag{41}$$

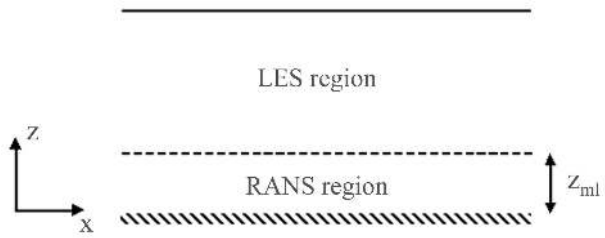

Figure 3. The near-wall RANS region and the outer LES region

For most computational grids equidistant spacing is used in the horizontal direction why Δ is more or less constant. Using (34), l_{LES} can written as,

$$l_{LES} = C_\Delta \Delta \simeq \frac{C_s (C_{\epsilon 1}/C_{\epsilon 2})\Delta}{C_\mu^{3/4}}, \tag{42}$$

and the distance from the wall where the change from RANS to LES happens can be estimated:

$$z_{ml} \simeq \frac{C_s}{\kappa}\frac{C_{\epsilon 1}}{C_{\epsilon 2}}\Delta \tag{43}$$

As seen, z_{ml} is dependent on Δ and is almost independent on C_μ ($C_{\epsilon 1}$ is slightly dependent on C_μ). This is an advantage since the same numerical mesh can be used for different values of C_μ. It is also important to note that there is no jump in eddy-viscosity going from RANS to LES. This is often seen in other hybrid methods.

3.4 Backscatter modeling

The essence of turbulence modeling (as described in section 3.2) is to account for the global net energy flux from resolved scales to subgrid-scales, i.e. the forward energy scatter. It has however been recognized that locally at times there is a backscatter of energy from the subgrid-scales to the resolved scales. This local backscatter of energy cannot be handled by the proposed turbulence model since it always gives positive values of eddy-viscosity. A separate model is necessary. As proposed by Leslie & Quarini [29] we model the backscatter separately from the forward energy scatter. Since backscatter of energy can be recognized as stochastic fluctuations of the SGS-stresses it only seems natural to model the backscatter by introducing random forcing. The proposed model is similar to the stochastic backscatter model by Mason & Thomson [36].

Leslie & Quarini [29] analyzed the rate of backscatter and showed that for the inertial subrange, backscatter rate scales with the local dissipation rate. Based on dimensional reasoning, Mason & Thomson [36] derived an expression for the local mean value of energy backscatter,

$$\langle B_\epsilon \rangle = C_B \left(\frac{\tilde{l}}{l_{LES}} \right)^5 \langle \tilde{\epsilon} \rangle, \tag{44}$$

where C_B is a parameter that depend on spatial filter. For a Top-hat filter the value of C_B was found to be about 0.489 [36]. The fraction $\tilde{l}/l_{LES}$ expresses the "RANS-to-LES-ratio" - it is zero at the wall and grows to one away from the wall

in the LES region. Since the near-wall turbulent structures are small compared to the numerical mesh, SGS-stresses approaches a deterministic value and only need to be handled in an averaged sense in this region (in the RANS-region). The "RANS-to-LES-ratio" ensures that backscatter is neglected in the RANS region.

The backscatter is modeled by adding stochastic forcing (acceleration) to the momentum equations (22) at each time step,

$$B_\epsilon = C_b \left(\frac{\tilde{l}}{l_{LES}} \right)^5 \tilde{\epsilon} = |f_i|^2 T_{SGS}, \tag{45}$$

where T_{SGS} is a timescale characteristic for the sub-grid scales, f_i are the three components of forcing and $\tilde{\epsilon}$ is obtained from equation (28).

The forcing should be correlated and contain length and time scales characteristic for the subgrid-scales. The time scale is applied by adding gaussian noise, w_i, at a prober level to the forcing used at the previous time step,

$$f_i^{n+1} = f_i^n \alpha_B + w_i, \tag{46}$$

where the correlation coefficient $\alpha_B = \exp(-\triangle t/T_{SGS})$ and $\triangle t$ is the numerical time step. Since the length scale characteristic for the subgrid-scale is the filter width, Δ, the timescale is chosen as Δ divided by the local velocity giving,

$$\alpha_B = \exp\left(-\triangle t \frac{\max(\overline{u}_i)}{\Delta} \right) = \exp(-CFL), \tag{47}$$

where CFL is the Courant-Friedrich-Levy-number (51).

The gaussian noise, w_i, is generated at each time step at a level that ensures (44). Mason and Thomson [36] specifies the random forces in terms of the rotation of a random vector potential, thereby ensuring a divergence free field and avoids stochastic contributions to the pressure fluctuation. We make no such corrections for continuity. Instead each component of the gaussian noise is scaled with the local velocity, $w_i \propto |\overline{u}_i| / (\overline{u}_i \overline{u}_i)^{1/2}$. This gives a force distribution similar to the model proposed by Piomelli et al. [45]. The random noise field is added to the forcing used at previous time step using (46) whereafter spatial correlation is added by applying a 1:2:1 smoothing operator in all three directions independent of mesh geometry.

The scaling of the gaussian noise with local velocity do not satisfy the assumption that the small scales are isotropic. The isotropy assumption is, however, only satisfied when grid resolution is fine compared to the large anisotropic turbulent structures generated by the mean shear. Near the wall where the backscatter model is most effective, grid resolution is relative coarse and anisotropy cannot be neglected - why scaling of each force component is important.

The backscatter model proposed is intensionally kept simple to reduce computational effort. The model increases computational cost by less than 5%.

3.5 Model constants

The model constants of the $k-\epsilon$ equations has been determined from experimental data and by considering a wide variety of flows. The originally proposed constants by Launder and Spalding [26] were established for industrial flows, while slightly different values have been found for atmospheric flows [43, 47, 74]. Even though we only use the presented model for atmospheric flows it is capable of dealing with industrial flows as well. Therefore we present the recommenced model constants for both cases.

Close to the surface where the logarithmic law-of-the-wall can be derived C_μ is determined by:

$$C_\mu = \left(\frac{u_{*0}^2}{\tilde{k}}\right)^2 = \left(\frac{\tau_0/\rho}{\tilde{k}}\right)^2 \tag{48}$$

For industrial flow $C_\mu = 0.09$ while a typical value for atmospheric flows is $C_\mu = 0.03$. At times, a different values of C_μ is chosen in order for the modeled turbulent kinetic energy, $\tilde{k}$, to match a specific measurement (se section 6.3). By considering the decay of grid turbulence and taking the turbulent diffusivity of momentum and turbulent kinetic energy equal the following constants has been found,

$$C_{\epsilon 2} \simeq 1.92$$
$$\sigma_\epsilon \simeq 1.30$$
$$\sigma_k \simeq 1.00$$

For industrial flows Launder and Spalding originally proposed $C_{\epsilon 1} = 1.42$ [26], which we will use. For other flows $C_{\epsilon 1}$ will be determined by,

$$C_{\epsilon 1} = C_{\epsilon 2} - \frac{\kappa^2}{C_\mu{}^{\frac{1}{2}}\sigma_\epsilon}, \tag{49}$$

where $\kappa = 0.40$ is the von Karman constant. When performing simulations with different values of C_μ, C_Δ needs to be changed accordingly. The LES-region should independently of C_μ dissipate energy at the correct level. To determine C_Δ equation (34) is used:

$$C_\Delta = C_s C_\mu^{-3/4} \frac{C_{\epsilon 1}}{C_{\epsilon 2}} \tag{50}$$

The value of $C_\Delta = 0.65$ was determined by simulating decaying isotropic turbulence with $C_\mu = 0.09$, $C_{\epsilon 1} = 1.42$ and $C_{\epsilon 2} = 1.92$ (see chapter 5 p. 32). This leads to $C_s = 0.144$. Furthermore, simulation show that $C_B = 0.70$ gives reasonable results. The standard model constants for industrial and atmospheric flows are listed in table 1 and are used for both RANS and LES.

Table 1. $k-\epsilon$ model constants for standard industrial flows ($C_\mu = 0.09$) and for standard atmospheric boundary layer flows ($C_\mu = 0.03$). For RANS $C_B = 0$

Flow	C_μ	κ	σ_k	σ_ϵ	$C_{\epsilon 1}$	$C_{\epsilon 2}$	C_Δ	C_B
Industrial	0.09	0.40	1.00	1.30	1.42	1.92	0.65	0.70
Atmospheric	0.03	0.40	1.00	1.30	1.21	1.92	1.26	0.70

3.6 Closure

This section presented the eddy-viscosity concept, where the unresolved turbulent stresses of both LES and RANS-simulations are represented by the product of fluid strain and the eddy-viscosity. The classical $k-\epsilon$ RANS-model was presented and by simple adjustment of the turbulent length scale the model was changed to a LES-model. The eddy-viscosity model can be chosen to run in pure "RANS-mode" or as a LES-model, where the near-wall flow is handled by RANS. It is a single turbulence model, which can be used for steady and transient RANS calculation as well as LES simulation over both smooth and rough walls.

The eddy-viscosity concept is used to model the main forward energy scatter - from large to small turbulent scales. To model the energy backscatter a simple stochastic backscatter model was presented. Furthermore, two sets of model constants were derived, one set for industrial flows and one set for atmospheric boundary layer flows.

4 Numerical Approach

Various errors exist in LES results. These come from both numerical errors as well as modeling errors in the SGS-model. Much research in LES is focused on improved SGS-models, without reference to the often more significant errors present. In this section different numerical approaches are addressed with the overall aim that numerical and modeling errors do not dominate results.

The section starts by giving a short introduction to how wind simulations are performed, after which the flow solver is presented. Here aspects, like choosing the right differencing schemes for the convective terms in the momentum equations and requirements for the time step, are discussed. The section then describes how to determine the forcing used to drive the simulations. Finally, the computational domain and grid generation is discussed where aspects like boundary conditions and domain sizes are addressed together with an estimation of the computational costs for wind simulations.

4.1 Wind simulation methodology

For traditional RANS simulations of the wind over terrain the approaching flow can be prescribed at the inlet of the computational domain. Since the inlet flow is constant in time a steady velocity profile, which may follow the logarithmic profile (38), can be specified at the inlet. Likewise is it possible to specify the turbulent kinetic energy and dissipation of turbulent kinetic energy at the inlet according to equilibrium relationships. To allow numerical simulations by LES, however, a different approach is necessary. For LES simulations it is necessary to prescribe a time-dependent inflow that accurately represents the turbulent structures of a wind environment. The technique adopted is to split the actual terrain simulation into two: an ABL simulation, that generates the time dependent wind data, this simulation is also called the ***precursor*** simulation and a second simulation, the ***successor*** simulation or the actual terrain simulation, which adopts the inflow generated by the precursor (see fig. 4).

Several inexpensive methods of generating synthetic turbulent inflow exists that can reproduce spectra and correlations of a targeted wind environment. These methods, however, does not reproduce the coherent structures observed in at-

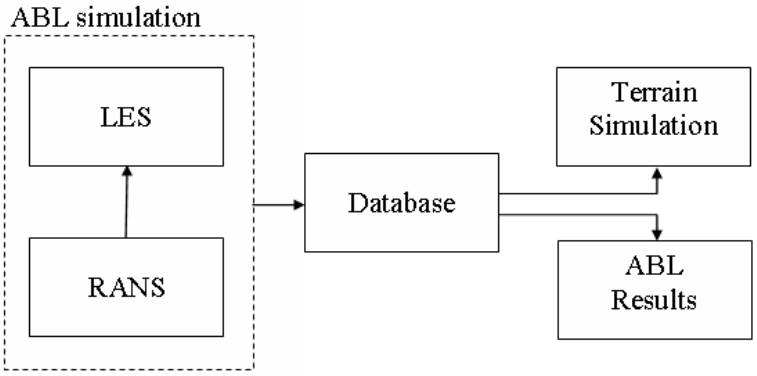

Figure 4. The ABL simulation (precursor) consist of a RANS simulation and a LES simulation, where the RANS simulations provides initial conditions for the LES simulation. The precursor generates winddata, which is stored in a database and can be used as inflow data for a terrain simulation (successor).

mospheric turbulence. The main advantages of using a precursor simulation is that the generated turbulence is made directly by the Navier-Stokes solver, which is also used for the successor simulation. The generated inflow data is therefore adapted to the solver and is a solution to the descretized Navier-Stokes equations, why it is likely to contain the physical coherent structures of turbulence. The purpose of the precursor simulation is however twofold. Besides generating inflow data for a successor simulation, the precursor provides valuable information of the wind environment over flat but rough terrain, why it is also called an ABL simulation.

The precursor is run in a computational domain with a bottom surface of constant roughness. The horizontal distance required to generate fully developed turbulent structures is large and would require a very long computational domain. Instead a smaller domain is used with the horizontal boundaries specified as cyclic, and simulation is run until a fully developed velocity profile is established consistent with the rough surface. The generated wind field is thus spatially homogeneous in horizontal directions. To save computational effort, the actual precursor simulation is first run as pure RANS simulation and the LES computation is then started from this solution. More than simply saving computational time the RANS solution is valuable to compare with the LES results. A detailed description and the results of the ABL simulations can be found in chapter 6 (p. 41).

Since most of the computational effort of a terrain simulation is spend on the precursor simulation the generated ABL wind field is stored and can subsequently be used many times as input to different terrain simulations (successor). The time dependent wind data $(\overline{u}, \overline{v}, \overline{w}, \tilde{k}, \tilde{\epsilon})$ from the precursor simulation is taken from a cross-sectional plane of the computational domain at each time step and is stored in a wind database. The cross-sectional plane from the precursor exactly corresponds to the inflow grid of the successor and the successor is run with the same time step, thereby avoiding both space and time interpolation. Contrary to the precursor that has a horizontally homogeneous wind field, the successor simulation is allowed spatial development. The successor simulation gets the wind data from the precursor at the inlet, but downstream of this location a new boundary layer will develop adapted to local terrain and roughness changes.

4.2 Flow solver

The CFD code EllipSys3D developed by Michelsen [37][38] and Sørensen [56] has been used in all calculations. It is a multiblock finite-volume discretisation of the incompressible Navier-Stokes equations (22). The multi-block facilities allow for geometrical flexibility and for large, parallel computations, which is necessary for the computational expensive simulations performed in this work. The exchange of information between processors is handled using Message Passage Interface, MPI.

The code is formulated in general curvilinear coordinates and uses structured unstaggered grids i.e. cell variables are stored in the cell centers. In all simulations the PISO algorithm [21] has been used to solve the equation system and pressure/velocity decoupling is avoided by applying the Rhie/Chow interpolation technique [48]. The TDMA solver (Tri-Diagonal Matrix Algorithm) is used in altering directions to solve the transport equations and pressure solution is accelerated using a multigrid method. The solution in time is advanced in time using a second order iterative time-stepping method. For RANS simulations solution time is minimized by using a three-level grid sequence. More than accelerating solution time, the grid sequence provides solutions on coarser mesh levels, which are important when insuring grid independent results.

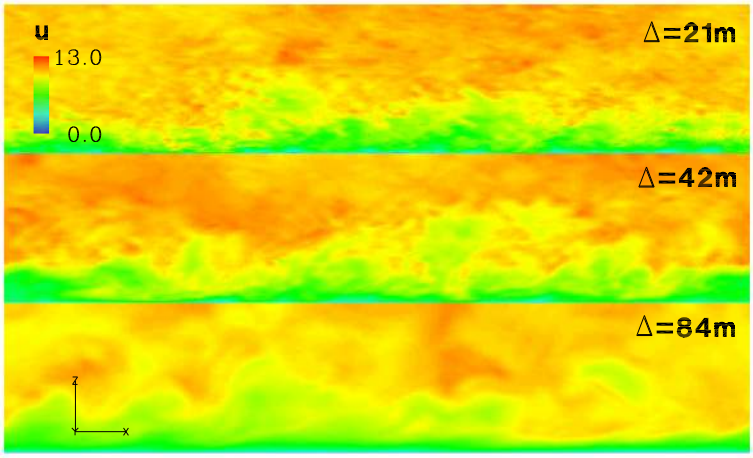

Figure 5. Contour plot of streamwise velocity for varying cutoff lengths. For the top plot a cutoff length equal the mesh spacing has been used (8). When the cutoff length is increased the simulation will eventually evolve from LES towards RANS. Simulations are run as precursors using mesh C (table 5), see chapter 6 (p. 41) for details.

Differencing schemes

As already shown, spatial filtering or Reynolds-averaging applied to the NS-equations produces a SGS-stress term that needed modeling (11). The full unlinear convective term of the NS-equations, $\overline{\partial u_i u_j}/\partial x_j$, has been split into two parts, a resolved convective term, $\partial \overline{u}_i \overline{u}_j/\partial x_j$, and the unresolved SGS-stress term, $\partial \tilde{\tau}_{ij}/\partial x_j$. When performing LES, these terms result in both numerical discretisation errors and SGS-modeling errors, both of which should be minimized. An analysis of the numerical errors can be found in [18] [25].

The importance of the SGS-model generally depends on the resolution of the numerical mesh (assuming that the SGS-model explicitly has the local mesh spacing as parameter). As the mesh is refined, less turbulent energy is placed in the subgrid scales and the importance of accurate turbulence modeling decreases. Discretisation errors cannot be removed by mesh refinement but can be reduced by using higher order numerical schemes. Even high order finite-difference schemes, however, have truncation errors at high wave-numbers i.e. at the smallest resolved scales [25]. To reduce this error explicit filters with larger filter widths can be applied to the non-linear term in order to reduce the small scale motions affected by the error. It has been noticed by several authors that explicit filtering reduces numerical errors (it completely removes aliasing errors) but it also increases the effect of the SGS-model thereby increasing the importance of advanced SGS-modeling. Furthermore, if an explicit filter of just twice the grid spacing is applied, the computational cost increases by a factor of 16 for the same nominal resolution [18], since mesh resolution should be doubled in all directions and time step halved.

Similar to applying explicit filters in order to damp small-scale motions prone to numerical errors, the turbulent length scale, l_{LES} (29), can be increased. This increases the eddy-viscosity and damps the resolved small-scale motions (see figure 5). For the LES simulations shown in this work, however, grid resolution is relatively coarse but cannot be increased much because of numerical cost. Since the nominal resolution in reality becomes lower for simulations with explicit filtering we do not use this technique. The downside of using the computational mesh

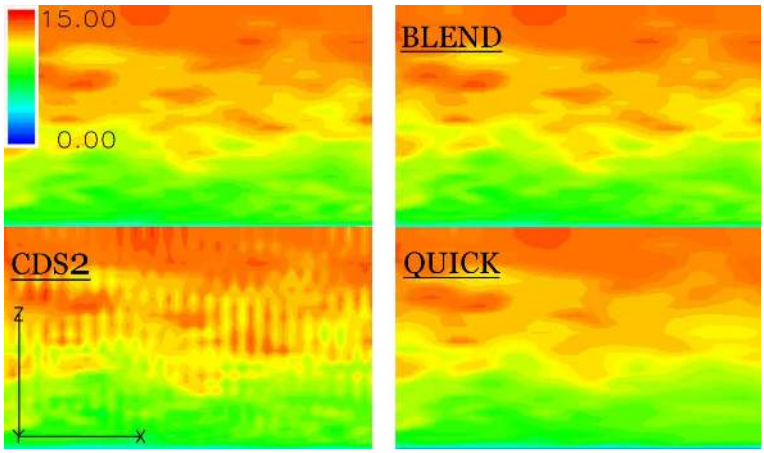

Figure 6. Contour plot of stream-wise velocity, $\overline{u}$. Left column: Top, cyclic horizontal boundary conditions (precursor), convective term are solved using CDS2. Bottom, Inflow and outflow condition in the horizontal (successor), convective terms are solved using CDS2. Right column (successor): Bottom, convective terms are solved using upwind scheme (QUICK). Top, a blend of QUICK (7%) and CDS2 (93%) is used.

as filter is that the magnitude of numerical errors may be comparable to that of the SGS stresses. As discussed by Lund [31], however, improved results may be obtained simply by mesh refinement without explicit filtering, due to the fact that numerical errors are moved out to higher wavenumbers.

Discretisation of the convective nonlinear terms in the NS-equations should in general be done with schemes with no or low numerical dissipation. For simulations performed in this work the smallest resolvable scales are too large for molecular viscosity to be of importance, energy dissipation therefore come from the SGS-model and from numerical dissipation. Since the SGS-model is dissipative in nature some researchers abandon the SGS-model all together and rely purely on numerical dissipation to work as turbulence model. Since numerical dissipation changes with different flows and different computational meshes, relying purely on numerical dissipation is not recommendable. Several discretisation schemes are available in EllipSys3D. In chapter 5 (p. 32) the SGS-model is calibrated by simulation of decaying homogeneous isotropic turbulence, and it is shown that the numerical dissipation from upwind schemes is too large. To reduce numerical dissipation the convective terms for all precursor simulations are solved using second-order (CDS2) or fourth-order (CDS4) central differencing schemes, based on deferred correction [24].

Generally, only central differencing schemes should be used when doing LES. When running successor simulations using the transient inflow from the precursor, however, unphysical fluctuations are observed. This is illustrated in the left column on figure 6, which shows contour plots of streamwise velocity for a precursor (top) and a successor (bottom) both performed using CDS2. The fluctuations are due to the unboundedness of the central differencing scheme, and are not observed for cyclic conditions. When an upwind scheme (QUICK) is used (bottom, right on figure 6) the fluctuations disappear. Comparing the contours for the precursor with the contours of the successor using QUICK it is, however, seen that details of the turbulent structures are lost using the upwind scheme. In order to remove the unphysical fluctuations but still limit the amount of numerical dissipation, we combine the upwind and the central scheme. As a result the fluctuations disappear and the detailed turbulent structures are preserved. When running terrain

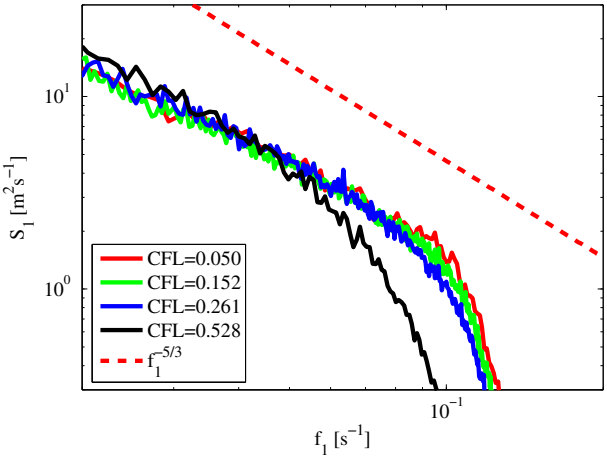

Figure 7. One-dimensional spectra corresponding to different time steps. The CDS4-scheme was used. In order to resolve all possible scales the maximum CFL-number should be 0.25.

simulations (successor) the convective scheme used will be a combination of 93% CDS2 (or CDS4) and 7% QUICK. For the precursor, purely central schemes are used.

Time step

Simulations are performed with a second order accurate iterative time stepping algorithm. We use an implicit time integration technique, which is stable for any size of time step. For explicit schemes, a general stability criterion demands that the Courant-Friedrich-Levy-number (CFL-number) is lower than one, meaning that the flow properties cannot advance more than one grid spacing during one time step,

$$CFL = \Delta t max\left(\frac{|\overline{u}|}{\Delta_x}, \frac{|\overline{v}|}{\Delta_y}, \frac{|\overline{w}|}{\Delta_z}\right) \leq 1 \tag{51}$$

For accuracy reasons, however, the time step must be smaller for both implicit and explicit time integration techniques.

To determine the required time step, channel flow simulations were performed with varying time steps. On figure 7 one-dimensional spectra of the u-velocity for different CFL-numbers are shown. The spectra are from different simulations but are taken at the same height (z=100m). All simulations are performed with the same simulation parameters only the time step was changed. On the figure it is seen that in order to resolve all possible scales the CFL-number must be $CFL = 0.25$ or smaller. For larger time steps numerical dissipation increases and energy is lost at high frequencies. Subsequently for all simulations the global time step is chosen to give a maximum CFL-number of less than 0.25

The precursor simulations are run until the boundary layer is fully developed and turbulence statistics has reached a steady state. This state is usually reached after about thirty non-dimensional time periods, $30Hu_{*0}^{-1}\Delta t^{-1}$, where H is the height of the computational domain. The successor simulation, which receives inflow turbulence from the precursor, should be run for at least one but preferable two flow-through times before results are sampled. A flow-trough time is defined by, L/u_0, where L is the length of the computational domain and u_0 is the mean inlet velocity.

4.3 Driving the ABL simulation

For the ABL simulations (precursors) a force is required to drive the flow. We generally consider two cases, a channel flow where the influence of Coriolis forces has been neglected and a second case that involves the Coriolis term. To drive the flow we impose a constant pressure gradient, which need to be determined.

Channel flow

With a channel flow, we consider a boundary layer flow that is driven by a constant pressure gradient in the flow direction. If the flow is considered stationary and horizontally homogeneous and Coriolis forces are neglected, the mean field NS-equation (17) in the x-direction becomes:

$$\frac{1}{\rho}\frac{\partial\langle p\rangle}{\partial x} = \frac{\partial}{\partial z}\left(\frac{1}{\rho}\langle\tilde{\tau}_{13}\rangle - \langle u^{'}w^{'}\rangle\right) = \frac{1}{\rho}\frac{\partial\langle\tau\rangle}{\partial z} \tag{52}$$

When simulating the ABL it is usually assumed that the top of the boundary layer (top of computational domain) has an inversion region where the stress can be set to zero i.e. the vertical component of turbulence is zero. Using $\tau = 0$ at the top of the boundary layer ($z = H$) it is found that the shear stress decreases linearly with height.

$$\langle\tau\rangle = H\frac{\partial\langle p\rangle}{\partial x}\left(\frac{z}{H} - 1\right) \tag{53}$$

Only near the wall, the assumption of a constant shear stress region equal to the wall stress holds, $\tau \simeq \tau_0$. This was one of the assumptions behind the logarithmic velocity profile (38). If we take $z = 0$ the pressure gradient required to drive the flow is found:

$$\tau_0 = -H\frac{\partial\langle p\rangle}{\partial x} = \rho u_{*0}^2 \tag{54}$$

$$\frac{\partial\langle p\rangle}{\partial x} = -\rho\frac{u_{*0}^2}{H} \tag{55}$$

For a given friction velocity, u_{*0}, is it possible to determine the required pressure gradient using (55).

Coriolis forcing

In the atmosphere Coriolis forces (6) cannot be neglected. If again molecular viscosity is neglected then for a horizontally homogeneous stationary flow the two horizontal NS-equations for the mean field become:

$$0 = \quad f_c\langle v\rangle - \frac{1}{\rho}\frac{\partial\langle p\rangle}{\partial x} + \frac{1}{\rho}\frac{\partial\langle\tau_{13}\rangle}{\partial z} \tag{56}$$

$$0 = -f_c\langle u\rangle - \frac{1}{\rho}\frac{\partial\langle p\rangle}{\partial y} + \frac{1}{\rho}\frac{\partial\langle\tau_{23}\rangle}{\partial z} \tag{57}$$

These two equations describe the so-called Ekman spiral wind profile. In the ABL the wind is seen to be a balance between the pressure, the Coriolis and the frictional forces. Because the relative strength of the frictional force and the Coriolis force changes throughout the boundary layer, the wind direction near the ground is different from the one at top of the boundary layer. If the vertical

turbulence fluctuations are assumed to disappear at the top of the atmospheric boundary layer, the geostrophic winds can be defined:

$$u_g \equiv -\frac{1}{\rho f_c}\frac{\partial \langle p \rangle}{\partial y} \tag{58}$$

$$v_g \equiv \quad \frac{1}{\rho f_c}\frac{\partial \langle p \rangle}{\partial x} \tag{59}$$

To drive an ABL flow with a geostrophic wind in the x-direction the following pressure gradient is required in the y-direction:

$$\langle \frac{\partial p}{\partial y} \rangle = -u_g \rho f_c \tag{60}$$

When doing an ABL simulation with Coriolis forcing, equation (60) is used to determine the required pressure gradient - which we take to be constant with height.

4.4 Computational domain

The computational domain should have a size so that the main scales of the atmospheric boundary layer (ABL) that are involved in the turbulence energy generation can be resolved, and at the same time the grid must be fine enough to allow adequate resolution of the smaller eddies. The aim is to generate grid independent results. Traditionally this is achieved by performing grid-dependency tests where the same simulation is repeated on meshes with increasing resolution. For LES of the ABL this technique is seldom adapted because the cost of even a coarsely resolved simulation is high and because non-linear interaction between numerical errors makes results difficult to interpret. A finer resolved simulation may not give the same solution since more physics is simulated.

This section describes how the computational grids for simulations of the ABL over flat terrain are generated. First the boundary conditions are described together with the outer dimension of the computational domain. Finally the actually meshing is explained.

Lateral boundary conditions

For ABL (precursor) studies, the flow is assumed to be statistically homogeneous in horizontal planes. Therefore, all lateral or horizontal boundaries are specified as being periodic (cyclic boundary condition) and simulations are run until the boundary layers are fully developed. If instead an inlet and outlet condition had been used the overall length for a thick boundary layer to develop would require a very large computational domain.

The generated turbulent wind from the ABL simulation is stored in a wind database and can subsequently be used as input for terrain simulations (successor). The time dependent wind data is taken from a cross-sectional plane that exactly corresponds to the inflow grid of the successor simulation. For the successor simulations, the traditional Neumann boundary condition (zero normal gradient) is used at the outlet. This boundary condition, however, generates spurious unphysical features in the solution near the outlet. This is seen on figure 8 where three different outlet conditions are compared to a precursor. To avoid the unphysical behavior, it is possible to use an convective outlet instead. This boundary condition has been implemented in EllipSys3D and greatly improves results. The approach we have adopted in this work, however, is simply to increase the length of the

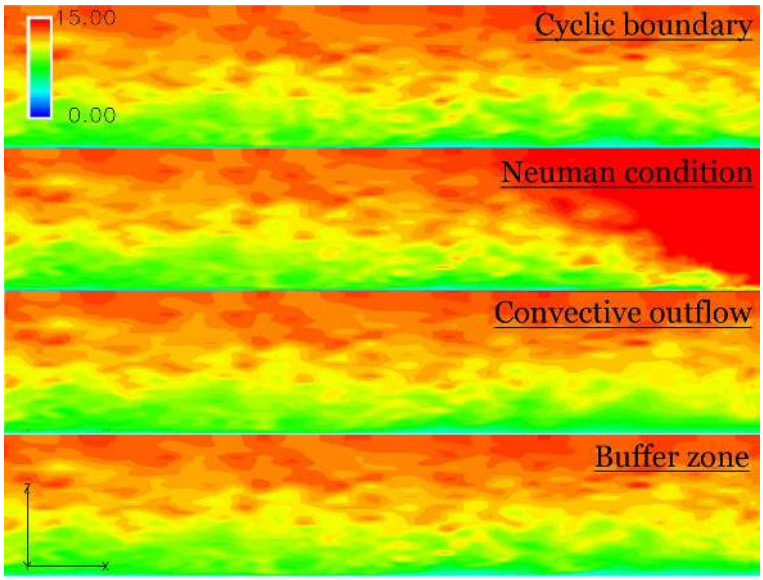

Figure 8. Contour plots of streamwise velocity. Three successor simulations with different outlet conditions are compared to a precursor simulation which uses cyclic boundary conditions. Turbulence from precursor is used as input to successors, and contour plots are compared at the same time-instance. The whole domain is not shown for the successor using bufferzone.

computational domain, so that a buffer zone exists between the region of interest and the outlet. Thereby the outlet is still treated with the Neumann condition. The two remaining lateral boundaries for the successor are specified as periodic.

Top boundary condition

At the top boundary a symmetry boundary condition (friction free wall) is used ($\partial u/\partial z = \partial v/\partial z = 0, w = 0$) to model an inversion layer (a layer where temperature increase with height at top of the ABL). Since the boundary do not allow fluxes to cross; pressure waves generated by topography will be reflected. This effect is assumed negligible however when the top boundary is placed far away from the surface. With domain heights of more than ten times the level difference at the surface we assume that the wave reflection is negligible. The symmetry condition inhibit the turbulent normal motions while tangential motions are enhanced.

Bottom boundary condition

As described in 3.3 (p. 14) the no-slip boundary condition cannot be applied to the bottom boundary because the surface is rough. A wall model must be used to represent the drag generated by the roughness of the surface. The method applied is similar to DES [61], but contrary to DES (used over smooth walls), we apply a wall model in the near surface RANS region, which secures a logarithmic profile. Furthermore, contrary to DES that treats most of the boundary layer with RANS, the proposed method only handles a very small portion of the boundary layer with RANS ($z < z_{ml}$). In the RANS region all is "modeled" in the sense that time dependency is week. The resolved frequencies in the RANS region are small, and do not supply any significant shear stress. The RANS region close to the wall ($z < z_{ml}$) (43) can be interpreted as a kind of boundary condition for the flow above.

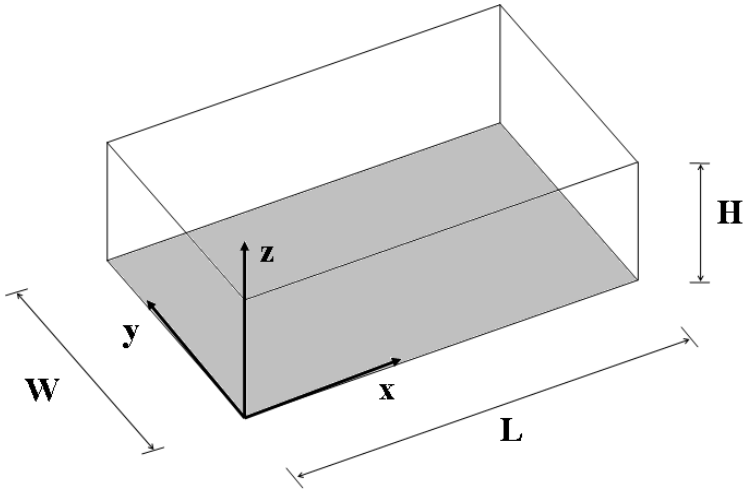

Figure 9. The main dimensions of the computational domain. L, W and H is the length, width and height of the domain. For ABL simulations the mean geostrophic wind is in the x-direction.

Domain dimensions

The computational domain's outer dimensions should be on a scale comparable to the largest turbulent scales. In the part of the ABL where the logarithmic velocity profile exists, shear flow instabilities dominate the flow. The scales of such instabilities increase with height so it is logical to assume that the largest turbulent structures scale with the boundary layer height, h. The equations of motion are solved in a three-dimensional domain, where L, W and H are the length, width and height of the domain (se fig. 9). These outer dimensions must be selected to best represent the ABL without constraining important turbulent structures, and to allow the successor terrain to be simulated.

The height (or depth) of the neutral boundary layer and consequently the height of the computational domain are followed by some uncertainty. For the neutral boundary layer the height is often taken to be proportional to the scale, u_{*0}/f_c, by some constant of proportionality. The choice of constant varies and of course influences results when fitting different data sets. A factor of 0.3 is often chosen. Domain height is thereby found by,

$$H = h = 0.3\frac{u_{*0}}{f_c} \tag{61}$$

Most ABL simulations performed in this work are performed on computational domains with H=1200m, which means that simulations should be performed with friction velocities of about $u_{*0} = 0.4ms^{-1}$. All ABL simulations are run until all statistics are fully converged i.e. the boundary layer is allowed to develop to the whole domain height, $H = h$.

The width of the domain must be chosen so that the largest scales of motion are unrestricted. Figure 10 shows how the domain width influences the mean velocity profile for an ABL simulation (driven as a channel flow). For the results shown the domain height is $H = 1200m$ and domain width is expanded by increasing the number of computational cells. Thereby the influence of the domain width is investigated without changing other simulation parameters. As seen, the domain width should be about four times the height to give domain independent results (W=4H). The velocity profiles on figure 10 are similar until a height were the domain width limits further growth of turbulent scales.

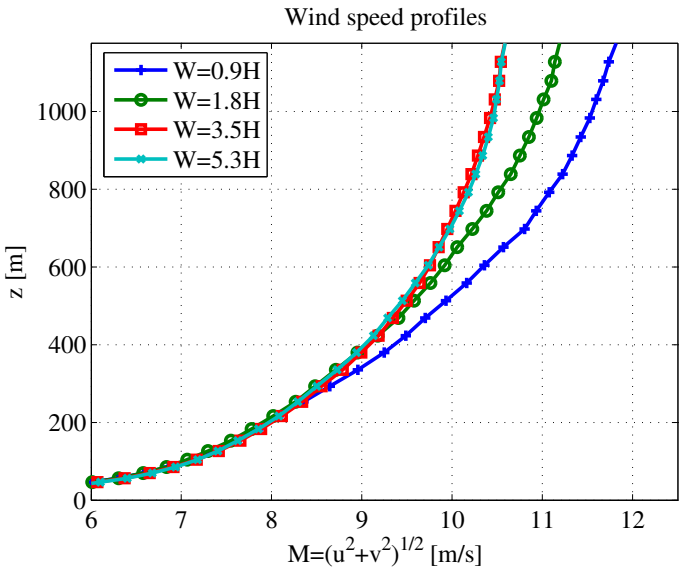

Figure 10. Velocity profiles for channel flow simulations performed with varying domain widths. For the two narrow domains (W=0.9H, W=1.8H) the large scale turbulence is restricted by domain boundaries resulting in speedup. Independent results are observed when $W \geq 3.5H$

When cyclic boundary conditions are used cyclic variations in time series will be observed and velocity spectra will contain marked peaks at frequencies corresponding to multiples of the domain length if the domain length is to short. The best way to determine the required domain length is by examining the streamwise two-point correlations to confirm that the flow variables become completely uncorrelated. Domains lengths of about six time the height is found to be adequate and is used throughout, giving domain sizes of approximately 6H×4H×1H.

Mesh generation

The filter used to separate resolved scales from subgrid-scales is not given explicitly, but is known to scale with Δ (8). The maximum grid spacing is thus the principal measure of the spatial resolution and should be kept as small as possible. The least expensive way to obtain a small filter-scale is to have cubic computational cells, as Δ is given by $\Delta = max(\Delta x, \Delta y, \Delta z)$. Ideally the LES region away from the wall should contain no stretching, but have a target grid spacing that prevails over this region.

To be able to capture near-wall gradients the grid must be refined in the wall-normal direction near the wall. For the log-layer to be accurate the stretching ratio ($S = \Delta z_{j+1}/\Delta z_j$) should be around 1.25 or less [60]. Refinements can be done but usually more is gained by refining the LES region, a maximum stretching of S = 1.20 is chosen. For the precursor mesh, grid cells are stretched from the wall to a specific height from were constant meshing is applied using a hyperbolic tangent transformation that insures a maximum stretch of S = 1.20 [57]. In the direction parallel to the wall equidistant spacing is used so that cubic cells are obtained in a region away from the wall. The lowest center point of a computational cell should be placed close to the surface so the no-slip boundary condition can be imposed by application of the law-of-the-wall. On the other hand, the lower bound for the logarithmic region and therefore the lower limit for the first computational cell is

about,

$$z^+_{log} \geq 70 = \frac{z u_{*0}}{\nu} \tag{62}$$

As a rule of thumb, a height of the first cell equal to the roughness height, z_0, is normally found adequate.

4.5 Computational costs

The precursor simulation is by far the most time consuming part of a terrain simulation, often using several weeks of computing time on fairly large computer clusters. A precise estimate of the computational time needed for an ABL simulation is therefore often valuable. Here we try to estimate the computational cost of the precursor at different grid resolutions given the power of the individual processors. We assume that the grid resolution for the outer LES flow is independent on Reynolds numbers

When the computational mesh of the precursor is generated, the grid spacing in the two horizontal directions is equidistant, whereas stretching is required in the vertical direction as described above. With a domain size of (6H, 4H, 1H) the required number of computational cells is,

$$N = N_x N_y N_z = \left(6\frac{H}{\Delta}\right)\left(4\frac{H}{\Delta}\right)\left(\frac{H}{\Delta} + \frac{\ln\frac{\Delta}{z_0}}{\ln S} - \frac{z_0}{\Delta}\frac{S^{\ln\frac{\Delta}{z_0}}}{S-1}\right), \tag{63}$$

where it has been assumed that the height of the first computational cell is equal to z_0 and that a constant stretching is used until a height from where constant mesh spacing is applied. By simplifying the expression and using (61) together with the recommended stretching ratio of S=1.2, we end up with the following expression for the required number of computational cells:

$$N \simeq 65 \cdot 10^{10}\left(\frac{u_{*0}}{\Delta}\right)^3\left(1 + 15\cdot 10^{-4}\frac{\Delta}{u_{*0}}\ln\frac{\Delta}{z_0}\right) \tag{64}$$

In order for the turbulence to fully develop the simulation should be run for about thirty non-dimensional time periods ($30 H u_{*0}^{-1}\Delta t^{-1}$). Using this together with $CFL = 0.25$ the number of required time steps, N_T, can be determined,

$$\Delta t = \frac{CFL\cdot\Delta}{u} \simeq 0.25\Delta\left(\frac{u_{*0}}{\kappa}\ln\frac{H}{z_0}\right)^{-1} \qquad Time = 30\frac{H}{u_{*0}} = \frac{9}{f_c} \tag{65}$$

$$N_T = 300\frac{H}{\Delta}\ln\frac{H}{z_0} = 90\cdot 10^4\frac{u_{*0}}{\Delta}\ln\frac{0.3u_{*0}}{f_c z_0} \tag{66}$$

A sample simulation run on 20 processors on a computational mesh of 80 blocks of 48^3 grid cells, showed that the total CPU time per time step per grid point was approximately $5\cdot 10^{-5}s$. Thereby the CPU time can be estimated by

$$CPUtime = 5\cdot 10^{-5} N_T N \tag{67}$$

On figure 11 the computational cost is shown for an ABL simulation with $u_{*0} = 0.4ms^{-1}$ and $z_0 = 0.1m$. It is seen that a simulation with $\Delta = 20m$ requires 8 million grid points and a CPU time of 600 days using 1 CPU (=1 month using 20 processors).

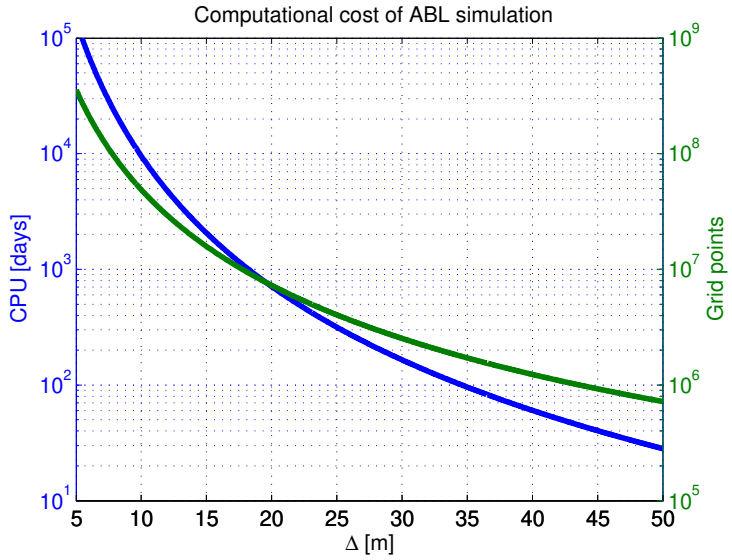

Figure 11. Estimated CPU time (using 1 CPU) and computational grid points for an ABL simulation with $u_{*0} = 0.4ms^{-1}$ *and* $z_0 = 0.1m$

4.6 Closure

This section presented a number of numerical techniques necessary in order to get numerical results not dominated by errors. First the whole windsimulation methodology was described. Here it was explained that a precursor simulation is needed, to generate the inflow turbulence necessary for the terrain simulation (the successor).

The finite-volume solver EllipSys3D was then presented. Since no explicit filtering of the flow equations is done, a high order difference scheme is needed in order to reduce discretisation errors. Furthermore, central differencing schemes must be used to reduce numerical dissipation and the numerical time step should be small enough to ensure $CFL \leq 0.25$.

Two methods was presented for driving the flow. A channel flow is driven by a constant pressure gradient in the streamwise direction, while an ABL flow, where Coriolis forces are important, is driven by a constant transverse pressure gradient. The geostrophic wind was found as a balance between pressure and Coriolis forces.

Finally the methodology behind generating the computational domain was explained. In order to capture the largest turbulent structures, the outer dimension should be 6H×4H×1H, where H is the domain height. The computational cost of the precursor was also estimated based on the spacing of the computational mesh, Δ.

5 Simulating Decaying Turbulence

Decaying isotropic turbulence is often used as benchmark test case to validate models and computer simulations. Isotropic turbulence is used because of its simplicity and because of the numerous experimental and numerical data available. A grid in uniform flow traditionally generates the isotropic turbulence in wind tunnel experiments. Downstream of the grid the fluctuating motion decays because no turbulent energy is created to balance the viscous dissipation (the shear away from the walls is zero). Finally, when all the turbulent energy has dissipated the flow tends to become laminar again. For LES the energy of the decaying turbulence is also directed towards smaller and smaller scales. Instead of dissipating because of molecular viscosity the dissipation happens at somewhat larger scale controlled by the SGS-model. Simulating decaying isotropic turbulence is therefore a possible way of validating the SGS-models ability to model the forward energy scatter.

The success of various computer simulations is normally measured by the model's ability to correctly capture the energy decay but also by how different various higher order statistics are reproduced. Comte-Bellot and Corrsin [14] provide some of the best-known experimental data of decaying isotropic turbulence. Their wind tunnel grid experiment provides data of turbulent kinetic energy and power spectra at different downstream locations. These spectra will be used to generate initial conditions for numerical simulations and they will be compared with the temporal evolution of the simulated velocity field. The evolution of the energy spectrum will be examined at different times in the simulation and compared to measurements.

When simulating the decay of isotropic turbulence only the LES-part of the SGS-model will be used i.e. the turbulent length scale (40) will be locked to the LES length scale ($\tilde{l} = l_{LES}$). The simulations are performed in a numerical domain with cyclic boundaries so there is no boundary layer that need to be treated by RANS. By simulating isotropic turbulence only the LES part of the SGS-model is calibrated, but many other numerical aspects are highlighted such as the importance of choosing prober differencing schemes.

5.1 Problem description

The forward scatter of turbulent energy from large to small turbulent scales controlled by the turbulence model need to be calibrated. For most flows the production and dissipation of turbulent kinetic energy is of a similar order of magnitude. When simulating decaying turbulence, however, no energy is produced since no wall shear exists, and the turbulence model's ability to dissipate energy can therefore be controlled.

For the ABL simulations performed in this work, molecular viscosity can generally be neglected why the eddy-viscosity is responsible for the main energy drain. As shown in (34) the eddy-viscosity can be estimated as $\nu_T = (\Delta C_s)^2 |\overline{S}|$ where C_s is given by:

$$C_s = C_\Delta C_\mu^{3/4} \frac{C_{\epsilon 2}}{C_{\epsilon 1}}. \tag{68}$$

The purpose of simulating decaying isotropic turbulence is therefore to determine C_s so that the model gives the correct level of energy dissipation. Different CFD codes are, however, implemented with different numerical schemes, which are more or less prone to numerical dissipation. Because of this, it is important to determine C_s together with the specific CFD-code and differencing schemes. The simulations shown are all performed using the model constants for standard

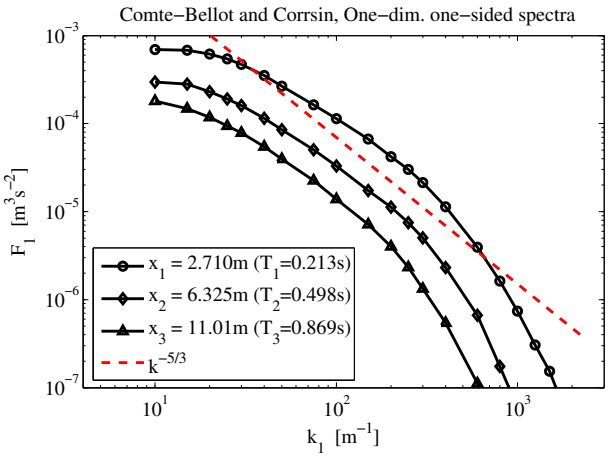

Figure 12. The experimental one-dimensional spectra is used for validations of numerical results. The ideal slope of $-5/3$ of the inertial range is shown

industrial flows ($C_\mu = 0.09$, $C_{\epsilon 1} = 1.42$ and $C_{\epsilon 2} = 1.92$) and varying values of C_Δ. C_s is subsequent determined using (68).

5.2 Experimental data

No experiment exits that simulate the temporally decay of isotropic turbulence. To provide such information the turbulent flow downstream of a grid in uniform flow is traditionally used. The comparison between the experiment and the time evolution of the spatially homogeneous turbulence is made by interpreting streamwise distances divided by the mean speed, $\langle u \rangle$ in the experiment as a time interval for the temporal decaying turbulence. This is the simple isotropic hypothesis of Taylor [64].

Comte-Bellot and Corrsin [14] have in their wind tunnel experiments measured velocity signals at different positions downstream of the grid. These experiments provide one-dimensional energy spectra that can be interpreted as the time evolution of the decaying isotropic turbulence and will be used for comparison with numerical results. Comte-Bellot and Corrsin provide spectra, which correspond to three instances in time $u_0 t/M_g$ = 42, 98 and 171, where u_0 is the inlet velocity ($u_0 = 10ms^{-1}$) and M_g is grid spacing in the experiment (M_g=0.0508m). The first spectrum will be used as initial conditions (T=0ms) for the numerical simulation while the last two (T=283ms and T=654ms) are used for validating the numerical model. The experiment was carried out with a Reynolds number based on the grid spacing ($Re = u_0 M/\nu$) of 34000. Because of this relative moderate Reynolds number, the experiment does not show an extended inertial range (see figure 12).

For a truly isotropic velocity field the turbulent kinetic energy and the r.m.s. velocity (σ_{u_i}) of the three velocity components (u,v,w) are equal.

$$\sigma_u^2 = \sigma_v^2 = \sigma_w^2 = \langle u^2 \rangle = \langle v^2 \rangle = \langle w^2 \rangle \tag{69}$$

The r.m.s. velocities given in the Comte-Bellot and Corrsin experiment are, however, not entirely equal and the velocity field is therefore not completely isotropic. To be able to compare the isotropic simulations with the experiment, the total level of turbulent kinetic energy at the three time instances is determined by integrating the one-dimensional spectrum, provided from the Comte-Bellot and

Corrsin experiment, over the whole wave number range:

$$\langle k \rangle = \frac{3}{2}\sigma_u^2 = \frac{3}{2}\int_0^\infty F_1(k_1)\, dk_1 \tag{70}$$

where k_1 is the spatial wave number. In table 2 the used values for total turbulent kinetic energy and the r.m.s. velocities are shown.

Table 2. The total turbulent kinetic energy, $\langle k \rangle$, and longitudinal integral scale, L_f, from the Comte-Bellot and Corrsin experiment. The values are shown for three different times instances corresponding to three locations in the wind tunnel. (exp.) is the values from the original paper

$u_0 t/M_g$	[-]	42	98	171
T	$[ms]$	0	283	654
L_f	$[m]$	0.0240	0.0345	0.0490
σ_u (exp.)	$[ms^{-1}]$	0.222	0.128	0.0895
σ_u (used)	$[ms^{-1}]$	0.214	0.118	0.0806
$\langle k \rangle$ (used)	$[m^2s^{-2}]$	0.0687	0.0209	0.0097

5.3 Computational mesh

To make computations as simple as possible a cubic computational mesh is used with cyclic (periodic) boundary conditions on all sides (see figure 13). The cyclic boundary conditions exclude walls, which could corrupt the decaying turbulence and the domain can be kept as small as possible. Since there is no mean velocity the domain size should be equivalent to the largest turbulent eddies that should be resolved. The smallest wave number represented is $k_{min} = 2\pi/L$, where L is the size of the computational box. The grid spacing must also be fine enough for eddies in the inertial range to be simulated. For a particular spatial resolution the highest theoretical resolved wave number is $k_c = \pi/\Delta$. This corresponds to the maximum resolvable wave number following the Nyquist theorem. We assume that wave numbers up to k_c are resolved, this corresponds to a sharp cutoff filter in Fourier space. On Figure 12 the one-dimensional spectra of Comte-Bellot and Corrsin experiment are shown. The largest measured eddies have a wave number of about $k_1 = 10m^{-1}$, which correspond to a length scale of 0.63 m. By choosing a domain size of L=1m the grid spacing on a 64^3 mesh is $\Delta = 0.016m$. Due to the Nyquist theorem the largest resolvable wave number becomes $k_c = 201m^{-1}$, which is seen to be in the inertial range (the range where the slope of energy spectra is -5/3). Simulations are also performed on a 128^3 mesh, which also have the cutoff wave number in the inertial range ($k_c = 402m^{-1}$). As described earlier the inertial range of the experiment is not too clear due the relative low Reynolds number, so it is difficult to specify a grid spacing that completely insures a cutoff wave number in this range. Table 3 shows the ideal resolved turbulent kinetic energy for the two mesh resolutions. These have been determined by integration of the one-dimensional spectra provided by the Comte-Bellot experiment over the wave number range $(0 - k_c)$.

All simulations are performed with a time-step of $\Delta t = 1 \cdot 10^{-3}s$ (for both $N = 64^3$ and $N = 128^3$), which insures a CFL number smaller than 0.1 and viscosity $\nu = 1.49 \cdot 10^{-5}m^2s^{-1}$ and air density $\rho = 1.225kgm^{-3}$. Computations are performed with four different schemes, central difference schemes of second- (CDS2) and fourth order (CDS4) accuracy and upwind schemes of first- (UDS)

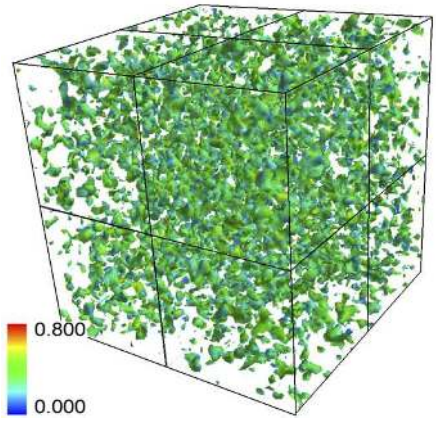

Figure 13. Isotropic, homogeneous turbulence in computational domain. Contours of iso-vorticity with colors corresponding to the total velocity during the early stages of a simulation

and third order (QUICK) accuracy. For post processing all statistics at a particular time is computed from the cell center variables and averaged over the entire domain.

Table 3. Resolved turbulent kinetic energy, $\langle\overline{k}\rangle$, for different mesh resolutions. The values of $\langle\overline{k}\rangle$ are determined from the Comte-Bellot and Corrsin one-dimensional spectra assuming a sharp cutoff filter when separating the subgrid scales from the resolved scales. The resolved contribution $\langle\overline{k}\rangle$ of the total, $\langle k\rangle$, is shown in parentheses.

T	$[ms]$	0	283	654
$\langle\overline{k}\rangle$ (64^3)	$[m^2s^{-2}]$	0.0579 (84%)	0.0187 (89%)	0.0091 (94%)
$\langle\overline{k}\rangle$ (128^3)	$[m^2s^{-2}]$	0.0654 (95%)	0.0205 (98%)	0.0096 (99%)

5.4 Initial conditions

The most crucial part of simulating decaying homogeneous isotropic turbulence is to generate a proper initial velocity field. Since no experimental data of a complete velocity field is available the turbulence has to be generated artificially from statistics. The turbulence field need to be generated so it corresponds to the first measured spectrum of the Comte-Bellot and Corrsin experiment.

As a first approach the initial isotropic turbulence field is generated by the algorithm described by Mann [32]. The generated turbulence field fits the von Karman spectrum, has equal variances $\sigma_u^2 = \sigma_v^2 = \sigma_w^2$ but the derivative skewness equals zero and the velocity field lacks the two-point correlations present in "real" turbulence. For isotropic turbulence the three-dimensional spectrum (the spectral tensor) is by Mann [32] described by the parameters α, ϵ and L_t (L_t is a length scale and α is the Kolmogorov constant). Using these scales the one-sided one-point u-spectrum suggested by Von Karman has the following form,

$$F_1(k_1) = \frac{18}{55}\alpha\epsilon^{2/3}L_t^{5/3}\frac{1}{(1+L_t^2k_1^2)^{5/6}} \qquad \sigma_u^2 = \int_0^\infty F_1(k_1)dk_1, \tag{71}$$

which is fitted to the measured spectrum using the values seen in table 4. When

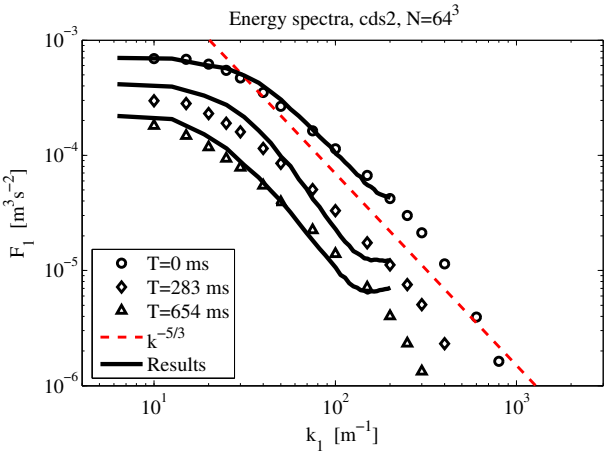

Figure 14. Turbulent spectra from simulation of decaying turbulence are compared to measurements. The initial velocity field is generated by a turbulence generator, that do not reproduces all of the statistics of real turbulence. The simulation is run on a $N = 64^3$ mesh with $C_\Delta = 0.65$

using the generated velocity field in a numerical simulation the turbulence need time to adapt to the numerical solver. This is seen on figure 14, where the decay of the generated turbulence is compared to the Comte-Bellot and Corrsin experiment. The initial spectrum (T=0) fits the experiment fairly well. Running the simulation, however, it is clearly seen that the spectrum experiences an unphysical transient behavior. First the slope of the inertial range steepens and energy starts accumulating at small scales, and then the slope returns to the theoretical value of -5/3. To avoid this transient behavior the initial turbulence field should be adopted to the Navier-Stokes solver before comparisons with the experiment are done.

Table 4. The parameters used when fitting the Von Karman spectrum to the experimental spectrum

α	=	1.7		, three-dimensional Kolmogorov constant
ϵ	=	0.3	m^2s^{-3}	, dissipation of turbulent kinetic energy
L_t	=	0.03	m	, a length scale of the spectral velocity tensor

To generate a velocity field that fits the experiment and is adopted to the Navier-Stokes solver, an initial turbulence field is generated with more energy than the experiment. Simulation is then run, but the results are first monitored when the energy level has decayed to fit the experiment. In this way it is possible to generate a field where the one-dimensional spectrum fit the experimental data. This method has been done for both the $N = 64^3$ and the $N = 128^3$ meshes using the CDS2-scheme and $C_\Delta = 0.65$, and their spectra are seen on figure 15. As seen the spectra do not match the experiment completely. This owes to the fact that the experimental spectra do not have an extended inertial range. It should be noted that exact fit of the spectra are of minor importance when calibrating the turbulence model. The calibration is primarily based on determining the value of C_Δ that gives the correct slope of the inertial range. This can actually be done without an experimental spectrum. The experimental spectrum is however important when validating that the numerical model simulates the decay of energy correctly.

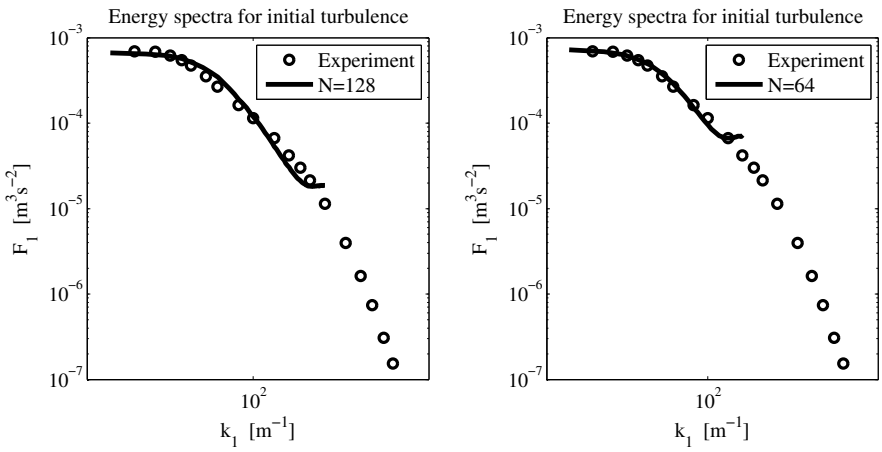

Figure 15. The one-dimensional spectra of the initial velocity fields for the $N = 128^3$ mesh (Left), and the 64^3 mesh (Right). Both fields are generated using the CDS2-scheme

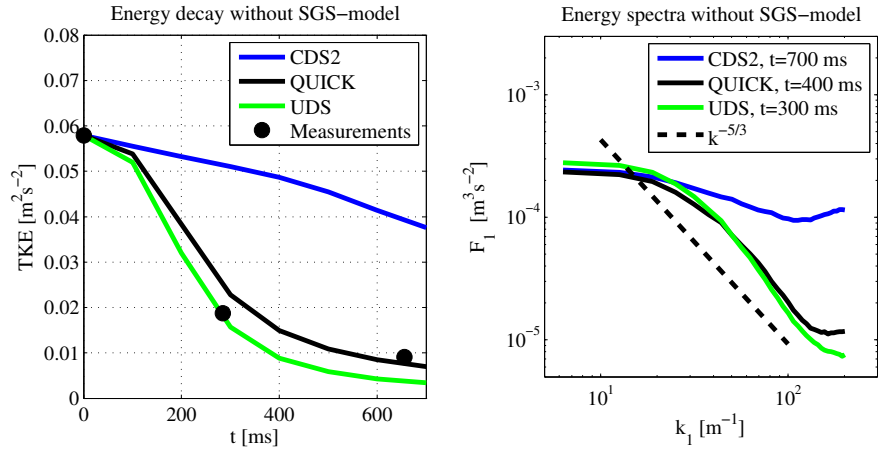

Figure 16. Simulation of decaying turbulence for different numerical schemes performed without SGS-model. Left, the time evolution of $\langle \overline{k} \rangle$. Measurements are only shown so that magnitudes can be compared. The two upwind-schemes are numerically too dissipative. Right, one-dimensional velocity spectra taken at different simulation times. The central scheme show little numerical dissipation (a positive quality), resulting in energy build up at small scales.

5.5 Results

Numerical dissipation

To get an impression of the level of numerical dissipation, simulations are first run without SGS-model (i.e. $\nu_T = 0$). Since the smallest turbulent scales simulated are too large for molecular viscosity to be of importance, energy dissipation is almost purely caused by numerical errors. For an ideal numerical scheme no dissipation would be observed. Simulations are run with both a central difference scheme (CDS2) and upwind schemes (UDS, QUICK) on the $N = 64^3$ mesh, and the same input conditions are used. On figure 16 (left) the decay of turbulent kinetic energy is shown. Here it is seen the numerical dissipation of the two upwind schemes is very large compared to the central scheme. The numerical dissipation

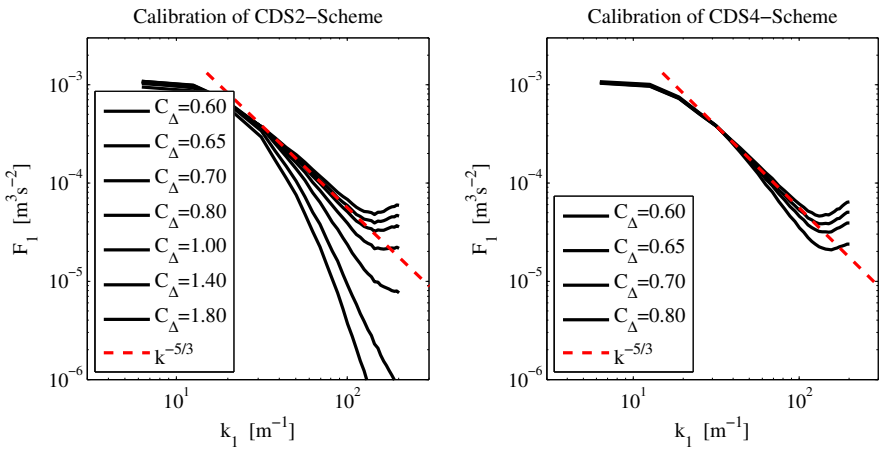

Figure 17. Turbulent one-point spectra for simulations performed on the $N = 64^3$ mesh with varying values of C_Δ. For both the CDS2-scheme (left) and the CDS4-scheme (right) a value of $C_\Delta = 0.65$ gives the ideal slope of -5/3 in most of the inertial range

for the upwind schemes alone, compares to that of the experimental data. This is an unwanted effect, since the dissipation will be too large when simulating with the turbulence model. Figure 16 (right) shows the spectra for the three numerical schemes after different simulation times. For the central scheme an energy accumulation is observed at small scales. The numerical dissipation is insufficient to balance the energy flux from the cascade (the energy transfer from larger to smaller scales), thus the small scales accumulate energy. For the upwind schemes the numerical dissipation is large so no energy accumulation is seen. Since the energy dissipation increases when adding the SGS-model, it is not possible to achieve the slope of -5/3 when using upwind schemes. This means that although upwind schemes are favorable in the fact that they are numerical stable, centered schemes are preferred for LES.

Calibrating the turbulence model

The turbulence model is calibrated so that the spectral slope fits the ideal slope of -5/3 in most of the inertial range. Thereby most information of the small eddies are kept. The model could have been calibrated with focus on the actual energy decay, but since the energy decay is dependent on the initial turbulence field it does not seem usable as calibration parameter. The calibration simulations are run with the two central schemes for varying values of C_Δ. There is a slight energy build-up at the highest wave-numbers. It is possible to choose a higher value of C_Δ thereby increasing the energy dissipation and removing this energy build-up. This does, however, make the slope of the spectra very steep and valuable information of resolvable eddies are lost.

On figure 17 the one-dimensional spectra for different values of C_Δ at a specific time are seen for the CDS2-scheme (left) and the CDS4-scheme (right). As expected the slope of the inertial range steepens as C_Δ increases. It is found that using $C_\Delta = 0.65$ insures that the spectral slopes in the inertial range are approximately -5/3 for both schemes. C_Δ is equivalent to C_{DES} used in the DES-model by Travin et al. [69]. They found $C_{DES} = 0.61$, which is comparable to $C_\Delta = 0.65$, but it shows that the correct value of C_Δ can vary with the numerical approach. Using (68) it is found that $C_s = 0.144$.

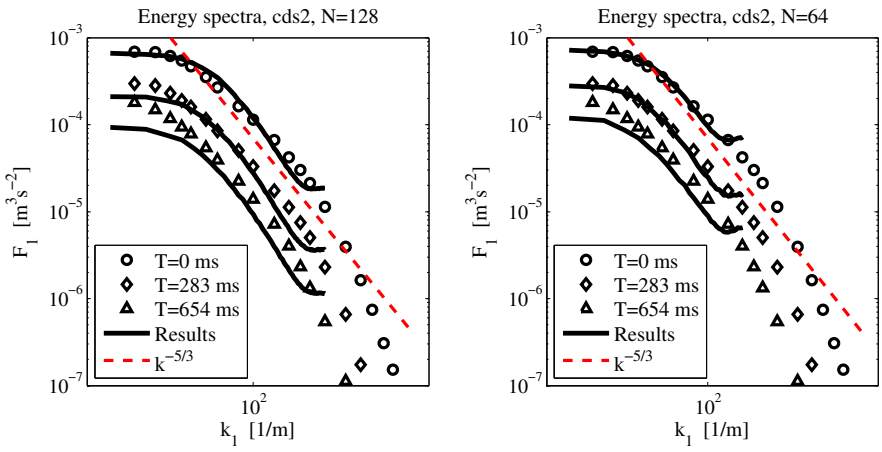

Figure 18. Temporal development of the one-dimensional spectra compared to the experiment. Left, $N = 128^3$. Right, $N = 64^3$.

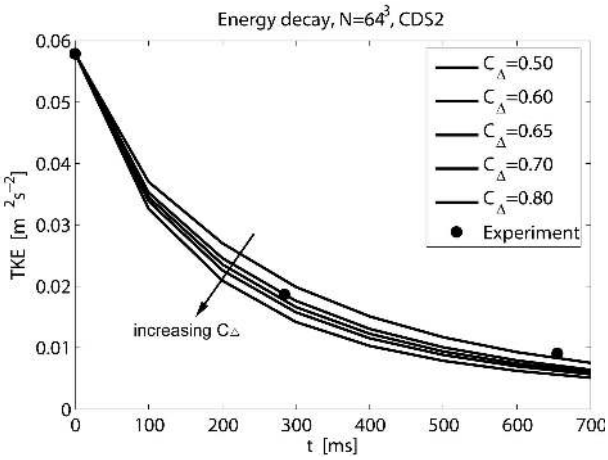

Figure 19. Time evolution of $\langle \overline{k} \rangle$ compared to measurements for varying values of C_Δ. Dissipation increases for increasing values of C_Δ.

On figure 18 the temporal development of the one-dimensional spectra is compared to the experiment. Calculation is here done with the CDS2-scheme for $N = 64^3$ and $N = 128^3$ grids. It is seen that the value of C_Δ gives the same slope of the inertial range and the same decay rates on both grids. The energy decay is too fast compared with the experiment; which might be connected to the energy build-up seen at high wave numbers. The fast energy decay is however not seen as conclusive. Performing the simulation with an initial velocity field generated as described by Mann [32] (see figure 14) gives a decay rate that is too small. The initial velocity field is therefore very decisive when simulating decaying turbulence. The slope of the inertial range and the energy decay is however shown to be independent of mesh resolution. On figure 19 the turbulent kinetic energy is plotted as function of time for different values of C_Δ for the CDS2-scheme. It is seen that the energy decay increases with increasing value of C_Δ. For $C_\Delta = 0.65$ the energy level fits well in the beginning of the simulation, but is a little to small at the end. Overall good agreement is found.

5.6 Closure

Decaying homogeneous isotropic turbulence was simulated in order to calibrate and validate the SGS-model. The energy decay was found to be very sensitive to the initial turbulence field. Velocity fields were, however, successfully generated for $N = 64^3$ and $N = 128^3$ grids.

Calibration showed, that for the two central schemes (CDS2 and CDS4), $C_\Delta = 0.65$ ($C_s = 0.144$), gave a proper slope of most of the inertial range. Some energy accumulation was, however, found at the highest wave numbers. The two central schemes gave similar results. The upwind schemes showed bad ability to resolve the high wave numbers, and did not show an extended inertial range. In general, upwind formulated schemes should not be used for LES. Simulation showed that although the LES-formulation is relative simple, reasonably good results can be achieved when simulating decaying turbulence.

6 Simulation of the Neutral ABL

The purpose of this chapter is to describe how simulation of the atmospheric boundary layer (ABL) are performed and present the simulation results for the proposed turbulence model. The section starts out by shortly discussing the problems of simulating the ABL, whereafter important relations and properties of both the boundary-layer and surface-layer are described. Different numerical aspects are then discussed such as the effect of changing the model constant C_μ and the effect of the backscatter model. Finally, the ABL relations and properties described will be used to validate results of both RANS and LES-simulations.

6.1 Problem description

The traditional problem in Large-eddy simulation of the ABL is that the mean velocity profile differs from similarity theory in the surface-layer. The problem occurs near the rough surface, where the contribution from the SGS model dominates that of the resolved terms. Because of high Reynolds numbers, it is computational too costly to resolve all the near-wall turbulent structures. In addition, the rough surface of the ABL introduces approximations by the need of a wall-layer model. As a consequence, many Large-eddy simulations of high Reynolds number boundary layer flows, show excessive gradients of the mean velocity near the wall.

Mason and Thomson [36] demonstrated that the Smagorinsky model coupled with a wall-model is unable to capture the logarithmic velocity profile. Excessive levels of shear were also found by Andren et al. [1] for SGS-models that solve the turbulent kinetic energy equation when calculating the eddy-viscosity (e.g. Moeng [40], Nieuwstadt and Brost [41] and Mason [34]). Mason and Thomson [36] explain the problem by the model's failure to represent the stochastic variations of the subgrid stresses. Introducing a backscatter model improved results [36]. Sullivan et al. [63] also achieved improved velocity profiles with a two-part eddy-viscosity model where the eddy viscosity was separated into a mean-field part and a fluctuating part.

Instead of applying some generalized law-of-the-wall at a distance from the wall, hybrid methods has been tried for high Reynolds number flows over smooth walls. Hybrid RANS/LES methods solve the unsteady RANS equations in the near-wall region and couples this to a LES model away from the wall. This approach was adopted by Nikitin et al. [42] who used DES [61] as wall-layer model in a series of channel flows. Nikitin et al. [42] found that even though a logarithmic velocity profile with a correct slope was formed in both RANS and LES region, the transition region between the two showed too high velocity gradients. This velocity shift is due to the change in eddy-viscosity. Between the RANS region with high levels of eddy-viscosity and the low level LES region, a region exists where resolved turbulent structures have not yet been formed. To balance the lack of Reynolds-stress carrying structures the velocity gradient increases [45].

As described above roughly two types of wall-models exist when performing LES. Either equilibrium laws applied directly to the first near-wall grid cell are used or hybrid RANS/LES methods are used. In both cases a velocity shift is traditionally observed. Using the first approach high velocity gradients are observed at the first near-wall grid cells, whereas for hybrid methods the velocity shift is found in a region between RANS and LES. We apply a hybrid method and introduce a stochastic backscatter model similar to Mason and Thomson [36] in order to minimize the velocity mismatch. The backscatter distorts and breaks up the unphysical turbulent structures from the RANS region and increases the rate of which Reynolds-stress carrying eddies are formed.

In this chapter the presented model's ability to capture both mean velocity profiles but also higher order statistics will be analyzed. Particular attention is made on insuring a smooth match between the near-wall RANS layer and the outer LES-layer. Achieving this is one of the main issues for hybrid RANS/LES methods. For the ease of reading and because the near-wall RANS region is relative thin the proposed model will simply be denoted as a LES-model.

6.2 Properties of the atmospheric boundary layer

In order to validate results, an overview of the most important scaling parameters and dimensionless relations commonly used for the neutral atmospheric boundary layer are given. These relations are mainly determined from dimensional analysis. The section is divided into to parts. First, important relations for the surface-layer are presented, whereafter relations valid for the rest of the boundary layer are given. The surface-layer is defined as the lowest 10% of the whole boundary layer height, or about 100m for the simulations presented here.

Important surface-layer relations

Near the ground, for the neutrally stratified ABL, turbulence is mechanically generated by the wind shear. It is therefore logical to assume that the surface stress, τ_0, is an important scaling parameter for the surface-layer. On the basis of the surface stresses (35) the characteristic velocity scale, the ***friction velocity***, u_{*0}, is defined. The total stress, τ, can be split into a resolved part, $\overline{\tau}$, and a modeled part, $\tilde{\tau}$. Since the near surface stresses for simulations are all modeled, only the modeled part of the stresses (35) need to be used when determining the surface stress,

$$\tau_0 = [\tau_{13}^2 + \tau_{23}^2]_0^{1/2} \approx [\tilde{\tau}_{13}^2 + \tilde{\tau}_{23}^2]_0^{1/2}, \tag{72}$$

and the friction velocity is defined from the surface stress by,

$$\tau_0/\rho \equiv u_{*0}^2 = C_D M^2 \tag{73}$$

C_D is a dimensionless drag coefficient that only depends on the roughness height, z_0, and M, which is a reference velocity determined at a specific height. Subscript 0 is used to denote that the surface stress and friction velocity are evaluated at the surface. When experimental measurements of u_{*0} are performed the measurements are for practical reasons performed at some height above ground. Even though u_{*0} decreases with height it is nearly constant in the surface-layer - this justifies the approximation. u_{*0} was considered constant in deriving the logarithmic law (38). The logarithmic law can therefore only be considered valid in the surface-layer. If the stresses used to determine the friction velocity are evaluated at greater heights, i.e. outside the surface-layer, subscript 0 is omitted and u_* is then a local characteristic velocity scale.

When results from simulations of the ABL are presented, the two horizontal components of velocity are arranged with the u-component directed in the local mean wind direction and the v-component transverse. To avoid confusion, however, we define the wind speed by,

$$M = \left(\overline{u}^2 + \overline{v}^2\right)^{1/2} \tag{74}$$

Assuming that the mean wind shear, $\partial\langle M\rangle/\partial z$, is dependent only on the friction

velocity and the height above the surface, z, dimensional analysis yields,

$$\Phi_m = \frac{\kappa z}{u_{*0}} \langle \frac{\partial M}{\partial z} \rangle, \tag{75}$$

Φ_m is the ***dimensionless wind shear*** (the Monin-Obukhov stability function for momentum) that for the neutral boundary layer $\Phi_m = 1$ in the surface-layer. The roughness length, z_0, has been neglected in Φ_m. Integration of (75) with respect to z gives the logarithmic velocity profile, (38), which we repeat for convenience,

$$\frac{\langle M \rangle}{u_{*0}} = \frac{1}{\kappa} \ln \left(\frac{z}{z_0} \right) = C_D^{-1/2} \tag{76}$$

For LES simulations, Φ_m, is an often used measure of the computational solvers ability to capture mean velocity profiles, and it is calculated from the horizontal- and time-averaged profile of wind speed. Similar to Φ_m, relations are usually made for the turbulent kinetic energy, Φ_k, and for the dissipation of turbulent kinetic energy, Φ_ϵ, these read,

$$\Phi_k = \frac{1}{u_{*0}^2} \langle k \rangle = C_\mu^{-1/2}, \tag{77}$$

$$\Phi_\epsilon = \frac{\kappa z}{u_{*0}^3} \langle \epsilon \rangle, \tag{78}$$

A number of different values for the three components of turbulence (the variances) in the surface-layer have been proposed by various authors. For the neutral ABL we use the recommendations by Gryning et al. [19] (for w' and v') and Stull [62] (for u'):

$$\frac{\langle w' \rangle^2}{u_{*0}^2} = 1.7 \tag{79}$$

$$\frac{\langle v' \rangle^2}{u_{*0}^2} = 2.0 \tag{80}$$

$$\frac{\langle u' \rangle^2}{u_{*0}^2} = 6.0 \tag{81}$$

Important boundary-layer relations

At times when the near surface-winds are unknown the surface stress may instead be expressed through the geostrophic winds (58,59),

$$\tau_0/\rho \equiv u_{*0}^2 = C_D G^2, \tag{82}$$

where the geostrophic wind speed, G, is determined by the two geostrophic wind components:

$$G = \sqrt{u_g^2 + v_g^2} \tag{83}$$

The geostrophic wind-components are defined using the horizontal pressure gradients (58,59), but at times the wind can be considered geostrophic at the top of

the boundary layer. The geostrophic drag coefficient, $u_{*0}/G = C_D^{1/2}$, is often expressed by the geostrophic resistance laws,

$$\frac{G}{u_{*0}} \cos\theta = \frac{1}{\kappa} \left[\ln\left(\frac{u_{*0}}{|f_c| z_0} \right) - A \right], \tag{84}$$

$$\frac{G}{u_{*0}} \sin\theta = \frac{B}{\kappa}, \tag{85}$$

where θ is the cross-isobaric angle (the angle between the surface stress and the geostrophic wind) and A and B are similarity constants. The measured values of A and B generally show some scatter, since they are depended on both stability and on the value of hf_c/u_{*0} [75]. It should be noted that for the ABL simulations presented $hf_c/u_{*0} \approx 0.3$. Traditionally, values of about A=1.5 and B=4 are used for the neutral ABL.

To describe the three components of turbulence throughout the neutral ABL we use the recommendations by Gryning et al. [19] (for w' and v') and Stull [62] (for u'),

$$\frac{\langle w' \rangle^2}{u_{*0}^2} = 1.7 - \frac{h}{z} \tag{86}$$

$$\frac{\langle v' \rangle^2}{u_{*0}^2} = 2.0 - \frac{h}{z} \tag{87}$$

$$\frac{\langle u' \rangle^2}{u_{*0}^2} = 6.0 \left(1 - \frac{z}{h}\right)^2 + \frac{z}{h} \frac{\langle u' \rangle_h^2}{u_{*0}^2} \tag{88}$$

where (86) and (87) are based on an empirical model by Brost et al. [8]. Since the boundary condition used for simulations ensures $\langle w' \rangle = 0$ at the top of the ABL, (86) is not valid throughout the whole boundary layer.

6.3 Numerical aspects

Flow setup

Simulations of the neutral atmospheric boundary layer are performed with both the classical high Reynolds number $k - \epsilon$ RANS model [26] and the proposed $k - \epsilon$ LES model. To drive the ABL flow a constant pressure gradient is used corresponding to a geostrophic wind of $(u_g, v_g) = (10, 0) ms^{-1}$ (58). Simulations are performed with the horizontal components of the Coriolis force, using a Coriolis parameter (6) of $f_c = 10^{-4} s^{-1}$.

Cyclic or periodic boundaries conditions are used in both horizontal directions, while a symmetry condition or stress free condition is used at the top boundary as described in sec. 4.4 (p. 26). The symmetry condition ensures that no mass is transferred across the top boundary. As described in sec. 3.3, the logarithmic wall-law, (38), must be used to represent the drag generated by the roughness of the surface. Both RANS and LES simulations are run with four roughness lengths $z_0 = 0.001m$, $0.03m$, $0.1m$ and $1m$ representative of different surface types ranging from open sea to forests [62].

Simulations have been performed on four different computational meshes (A,B,C,D). However, only results from mesh A and C, are presented (see table 5). Mesh A and C both have domain heights of 1200m and have similar outer dimensions. Mesh A is relatively coarse with horizontal grid spacings of $\Delta = 44m$ while mesh C is

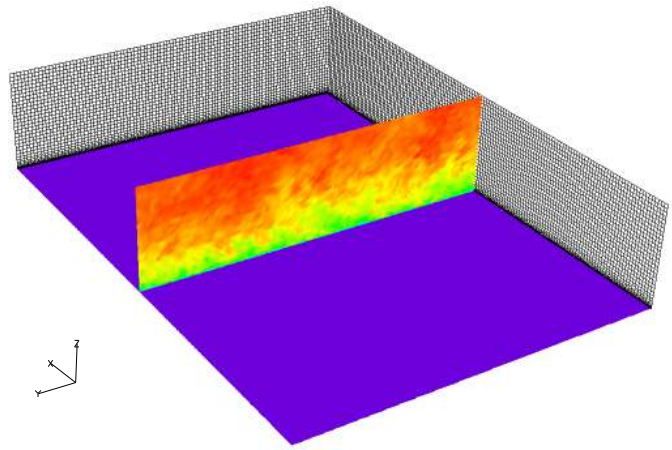

Figure 20. Mesh A. The figure gives an impression of the domain dimensions. The z-axis is in vertical while x and y-axis are in the horizontal. A cross sectional plane shows the instantaneous contours of wind speed.

finer with $\Delta = 21m$. Mesh A is shown on figure 20. A more detailed description of how computational meshes are generated is found in sec. 4.4.

Before the actual results are presented, the effect of changing the value of C_μ is described. Furthermore, the influence of using the backscatter model is also presented. All the results presented are calculated from time-series, and results denoted by $\langle\rangle$ are both time-averaged and averaged over horizontal directions.

Table 5. Domain sizes and mesh details. The domains of sizes (L,W,H) are partitioned into (N_x,N_y,N_z) grid cells. z_1 is the height of the first near-wall grid cell, and S is the maximum stretching ratio applied to the mesh near the wall.

Mesh	L [km]	W [km]	H [km]	N_x [-]	N_y [-]	N_z [-]	$\triangle$ [m]	S [-]	z_1 [m]
A	6.4	4.2	1.2	144	96	48	44.2	1.25	0.17
C	6.0	4.3	1.2	280	200	80	21.4	1.20	0.11

Value of C_μ

The total level of turbulent kinetic energy, $\langle k\rangle$, is traditionally assumed constant with height in the surface-layer (77). The specific value of $\langle k\rangle$ for an atmospheric flow does, however, depend on many factors such as stratification, surface roughness and topography. For RANS simulations turbulent kinetic energy (TKE) is all modeled, and the level of TKE in the surface-layer can be adjusted by changing the model constant C_μ,

$$\langle k\rangle = \frac{u_{*0}^2}{C_\mu^{1/2}}, \tag{89}$$

where $C_\mu = 0.03$ is the standard value for RANS simulations of atmospheric flows (see table 1). When on-site measurements are available, the value of C_μ is normally changed so that the level of turbulent kinetic energy matches that of the specific measurement. Here we want to investigate how to chose C_μ for LES. In order to investigate the effect of changing C_μ, a set of RANS and LES simulations are performed - table 6 shows the simulations parameters.

Table 6. Top table: Parameters for RANS simulations performed with varying values of C_μ. For $C_\mu = 0.27$ eq. (49) is used to determine $C_{\epsilon 1} = 1.68$. Otherwise, standard model constants are used (see table 1). Bottom table: Parameters for LES

Mesh	*Scheme*	C_μ	C_b	z_0	$\triangle$t	u_g	v_g
A	CDS2	0.27	0.00	0.100m	1.00s	$10ms^{-1}$	$0ms^{-1}$
A	CDS2	0.09	0.00	0.100m	1.00s	$10ms^{-1}$	$0ms^{-1}$
A	CDS2	0.03	0.00	0.100m	1.00s	$10ms^{-1}$	$0ms^{-1}$

Mesh	*Scheme*	C_μ	C_b	z_0	$\triangle$t	u_g	v_g
A	CDS4	0.09	0.70	0.100m	1.00s	$10ms^{-1}$	$0ms^{-1}$
A	CDS4	0.03	0.70	0.100m	1.00s	$10ms^{-1}$	$0ms^{-1}$
C	CDS4	0.09	0.70	0.100m	0.50s	$10ms^{-1}$	$0ms^{-1}$
C	CDS4	0.03	0.70	0.100m	0.50s	$10ms^{-1}$	$0ms^{-1}$

On figure 21, profiles of TKE and dissipation of TKE, are shown for the RANS simulations throughout the ABL. When C_μ is changed the level of TKE in the surface-layer ($z \leq 100m$), is adjusted following (89), while the profile of surface-layer dissipation remains unaffected - expected according to (78),

$$\langle \epsilon \rangle = \frac{u_{*0}^3}{\kappa z} \tag{90}$$

Outside the surface-layer both TKE and dissipation drop. If the expression for the eddy-viscosity, (26), is used with (89) and (90)it is found that the surface-layer eddy-viscosity can be determined by,

$$\langle \nu_T \rangle = u_{*0} \kappa z \tag{91}$$

On figure 22 the RANS profiles of eddy-viscosity and velocity profiles for varying values of C_μ are shown. As expected the profiles are similar in the surface-layer, but start to deviate in the outer layer.

The ability to change the level of turbulent kinetic energy for RANS simulations is convenient when fitting simulation results to experimental measurements. One would, however, expect that for a truly neutral, fully developed boundary layer of constant surface roughness a unique solution would exist. When different levels of TKE can be found for ABL measurements, it is a consequence of a range of processes. Stratification may not be truly neutral or upstream topographic features may have an effect on the local wind. Instead of modeling these complicated processes for RANS, it is often more convenient to compensate by changing C_μ so that the level of TKE matches the given experiment. Since the level of near-wall turbulence is important, e.g. to capture the correct separation point in complex terrain, a proper value of C_μ is needed.

For LES of the neutral ABL, the results are to a large degree independent of C_μ. Figure 23 shows the profiles of TKE (top), dissipation (middle) and velocity (bottom) for LES performed on mesh A and mesh C. Near the surface, in the RANS-layer, most TKE is modeled ($k \approx \tilde{k}$), and above this height TKE is mostly resolved ($k \approx \overline{k}$). The first thing to note is that the resolved part of the turbulent kinetic energy is independent on C_μ. Differences are observed but are mostly due to difficulties in achieving fully converged results for LES. The amount of resolved turbulence in LES is generated mechanically by the wind shear, and because the surface-layer velocity is unaffected by C_μ so is the resolved TKE.

The modeled contribution of TKE in the near-wall RANS region, found by (30), can still be determined by (89) but the level drops rapidly in the LES-region where

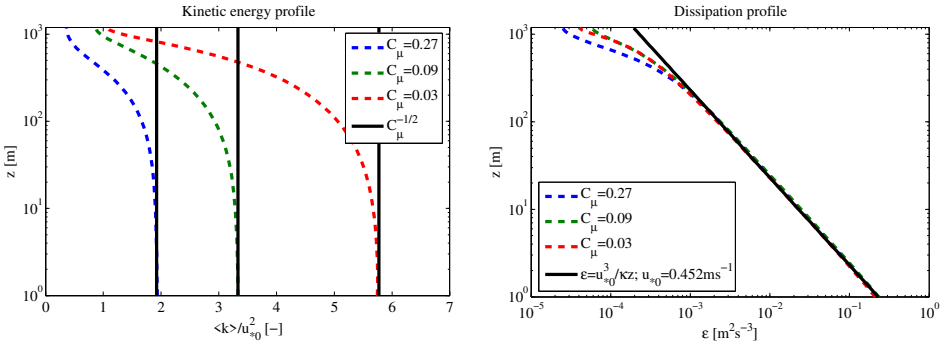

Figure 21. Left: Logarithmic plot of profiles of turbulent kinetic energy (TKE). For RANS, TKE is all modeled and the near-wall level can be determined by $\langle\tilde{k}\rangle/u_{*0}^2 = C_\mu^{-0.5}$. *Right: Modeled part of TKE dissipation found with eq. (28).*

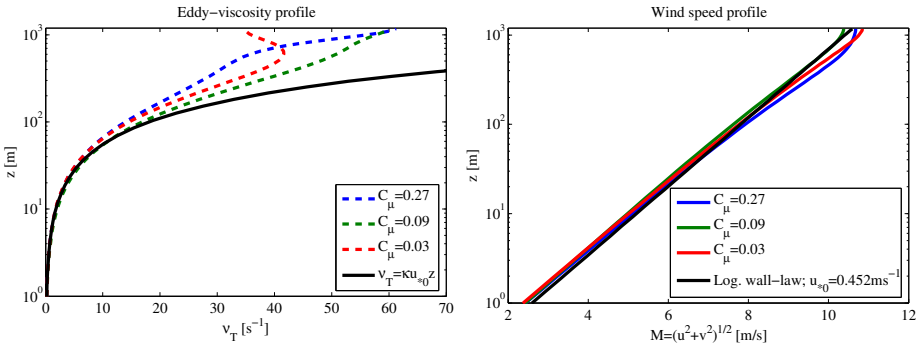

Figure 22. Left: Logarithmic plot of eddy-viscosity profiles. Right: RANS velocity profiles for varying values of C_μ *compared to the logarithmic profile.*

most turbulence is resolved. As seen, the modeled TKE in both LES- and RANS-region still varies with C_μ when performing LES. The relation between $\tilde{k}$ and $\tilde{\epsilon}$, (26), adjusts to give a prober value of eddy-viscosity, but the actual level of $\tilde{k}$ is more or less arbitrary. If the modeled and resolved TKE are added, for varying values of C_μ, then the total TKE is either unrealistically high in the LES region or unrealistically low in the RANS region. Therefore, $\tilde{k}$ found by (30) is inadequate for determining the subgrid-scale TKE in the LES region.

In the middle of figure 23 the level of modeled dissipation in the near-wall region for LES is seen to be unaffected by C_μ. Near the surface the modeled dissipation still follows (90), but drops in the LES region, where a greater part is resolved. Since the backscatter model, described in sec. 3.4, scatters energy at a level corresponding to the modeled dissipation, and because it is mostly effective close to the RANS-region, the backscatter model is assumed independent of C_μ. On the bottom of figure 23 the LES velocity profiles from mesh A and C are shown. It is seen that the velocity profiles indeed seem independent of C_μ when simulating the ABL. However, in order to show that the LES model is independent on C_μ and that it works as a Smagorinsky model, the Smagorinsky constant has been calculated using (34),

$$C_s = \left(\frac{\nu_T}{|\overline{S}|}\right)^{0.5} \Delta^{-1} \tag{92}$$

The proposed turbulence model was calibrated simulating decaying turbulence using $C_\mu = 0.09$ and for this C_μ it was found that $C_s = 0.144$. Running the ABL

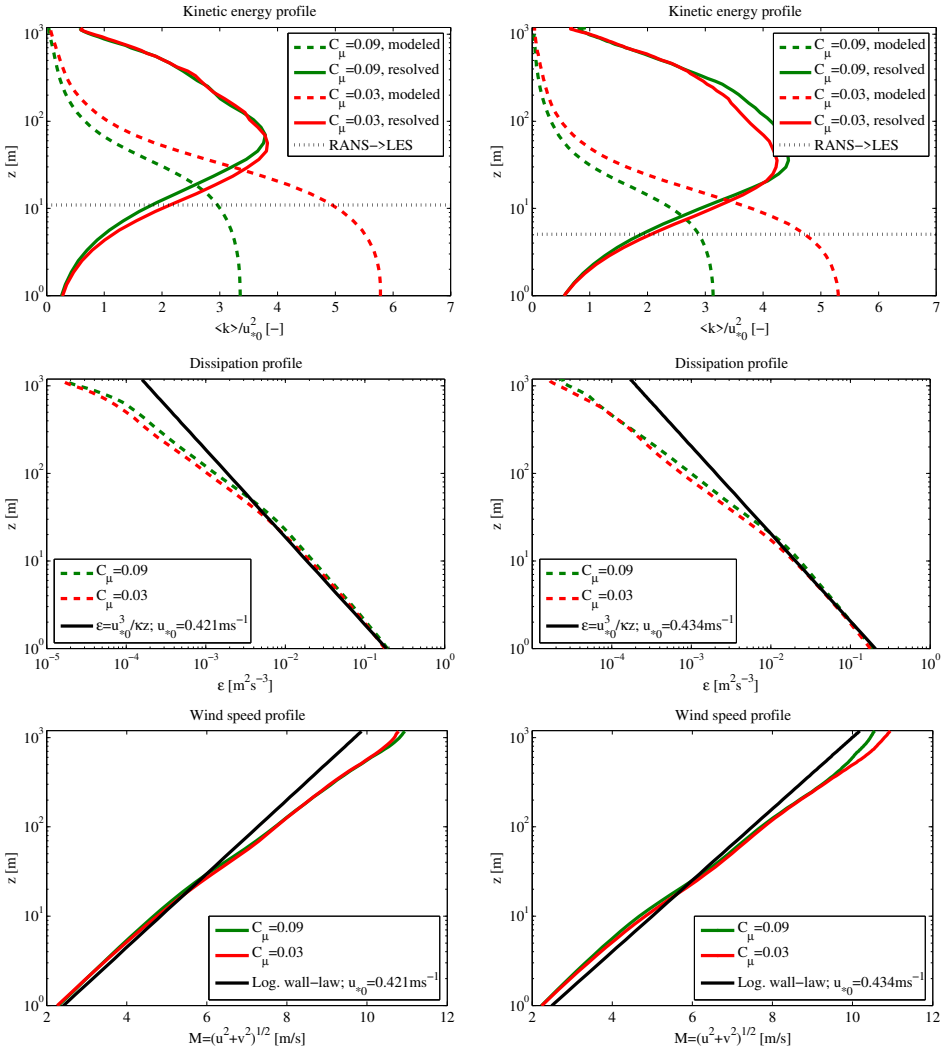

Figure 23. Left and right column are LES results for mesh A and mesh C respectively. Top: profiles of turbulent kinetic energy, where dashed lines are the modeled contributions and solid lines are the resolved contributions. The theoretical height, where the change from RANS to LES happens (43) is also shown. Close to the wall the TKE is all modeled and the level can be determined by $\langle\tilde{k}\rangle/u_{*0}^2 = C_\mu^{-0.5}$. *Middle: modeled part of the dissipation of turbulent kinetic energy, found with eq. (28). Bottom: Velocity profiles for varying values of* C_μ

simulations with different values of C_μ we want to ensure that this is still equivalent to $C_s = 0.144$. Figure 24 shows the calculated profiles of the Smagorinsky constant using mesh A and C for $C_\mu = 0.03$. As seen, C_s is still close to the calibrated value. This means that when C_Δ is determined using (50) the LES region works as a Smagorinsky model that is independent on C_μ.

Since prober modeling of the near-wall RANS region is important in complex terrain and because the resolved TKE is unaffected by C_μ, C_μ should be chosen following traditional RANS practise, so that the modeled turbulent kinetic energy matches field observations. This will ensure that the RANS region behaves correctly. If no field observation exists C_μ=0.03. The LES region is unaffected by C_μ an dissipates energy correctly as long as C_Δ is determined using (50). In the LES region the modeled TKE found by (30) is incorrect and should not be used as measure for the subgrid-scale turbulent kinetic energy. Calculation of the normal stresses, i.e the SGS TKE, is often difficult for SGS models. Therefore, when

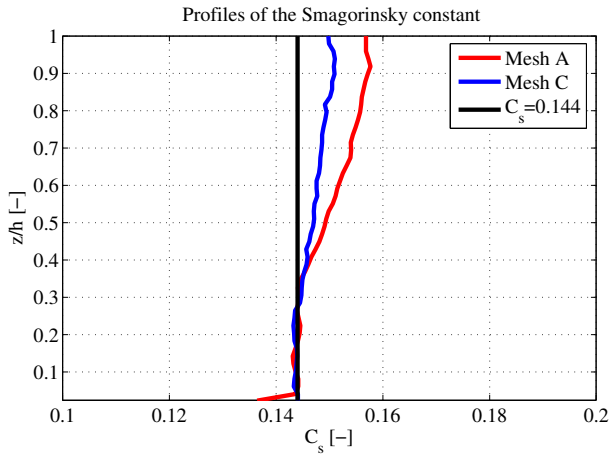

Figure 24. Profiles of the Smagorinsky constant calculated using 92. The turbulence model was calibrated to give $C_s = 0.144$.

presenting results only the resolved normal stresses will be shown. However, both resolved and modeled shear stresses are presented, since these are both correct.

Since LES-results of ABL simulations are independent on the value of C_μ, we will only use the classical value $C_\mu = 0.03$ in the rest of this chapter.

Backscatter model

In order to determine the effect of the backscatter model when LES is performed, a series of simulations with and without backscatter has been run. A wide range of simulations have been made in order to determine the appropriate level of backscatter, here we only present results from the simulations shown in table 7.

Table 7. Simulation parameters for investigating the effect of using the backscatter model for LES. Simulations are performed on mesh A and C with and without the backscatter model. Standard model constants are used (see table 1).

Mesh	*Scheme*	C_μ	C_b	z_0	$\triangle$t	u_g	v_g
C	CDS2	0.03	0.00	0.100m	0.50s	$10ms^{-1}$	$0ms^{-1}$
C	CDS2	0.03	0.70	0.100m	0.50s	$10ms^{-1}$	$0ms^{-1}$
A	CDS2	0.03	0.00	0.100m	1.00s	$10ms^{-1}$	$0ms^{-1}$
A	CDS2	0.03	0.70	0.100m	1.00s	$10ms^{-1}$	$0ms^{-1}$

The level of backscatter applied is shown on figure 25. Here it is seen that the backscatter goes to zero in the near-wall RANS region and again in the outer region, where the level of modeled dissipation is small. As designed, the backscatter is large in the "buffer region" between the RANS and LES region. Since the change from RANS to LES happens closer to the surface for the fine mesh (mesh C), higher levels of backscatter are observed for this mesh (due to high dissipation near the surface). The scaling of the backscatter forcing with the local velocity components, dampens the vertical and transverse force components and enhances the streamwise, giving a backscatter distribution similar to Piomelli et al. [45].

Figure 26 shows the dimensionless wind shear and wind profiles for simulations with and without backscatter. Concentrating on the results from simulations without backscatter (dashed lines) excessive wind gradients are clearly observed in the transition region between RANS and LES. The highest wind gradients are found

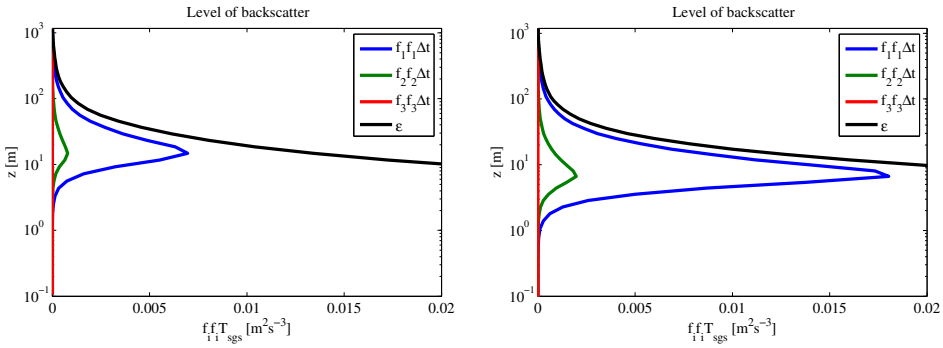

Figure 25. The three components of backscatter forcing compared to the modeled energy dissipation. Left: coarse mesh (mesh A). Right: mesh C.

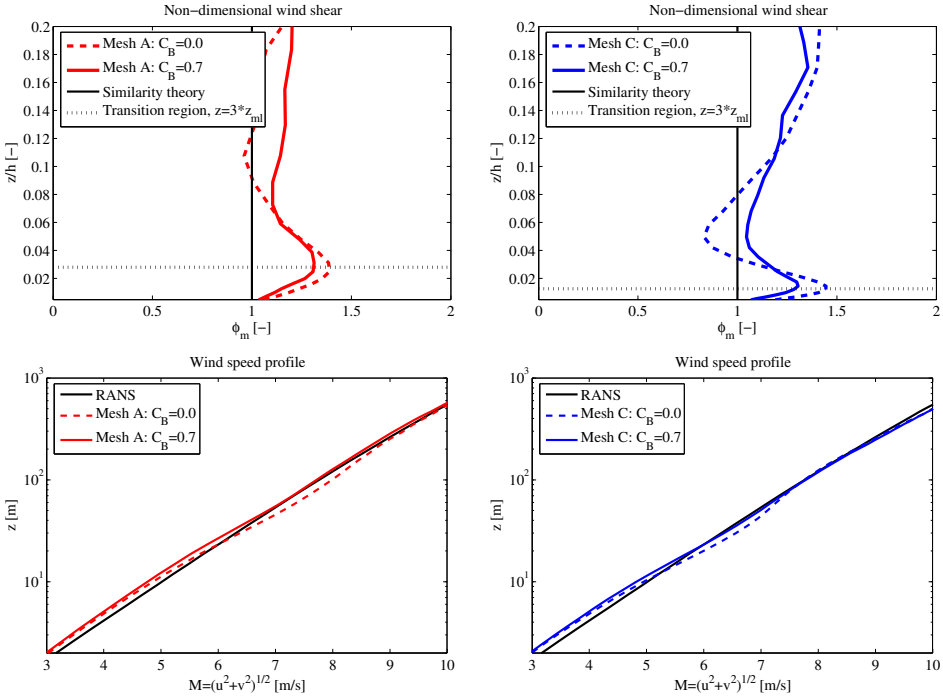

Figure 26. Mean velocity profiles, with (solid lines) and without backscatter (dashed lines). Top row: Dimensionless wind shear (75) in the surface-layer. Bottom row: velocity profiles on logarithmic scale. Left column, mesh A. Right column, mesh C.

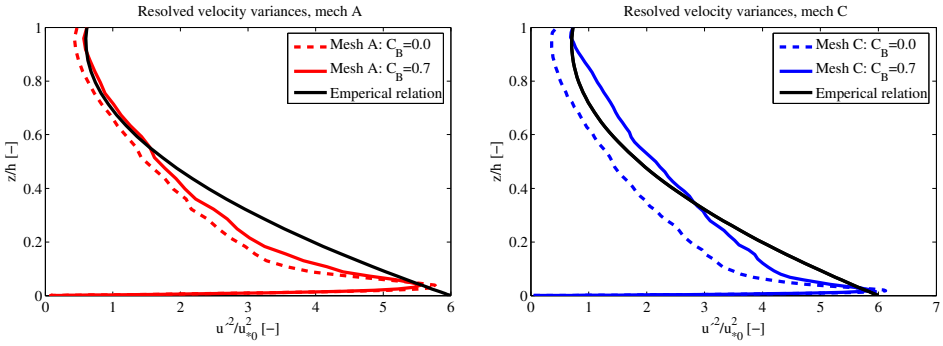

Figure 27. The streamwise component of the resolved velocity variance for simulations with and without backscatter model. The predicted curve, using equation (88), is also shown. Left: simulations on mesh A. Right: simulations on mesh C.

at about $z = 3z_{ml}$, where z_{ml} is the theoretical hight of the change between RANS and LES (43). Near the surface, in the RANS region, the velocity profiles are logarithmic with a given slope. At some height the profiles clearly start to deviate from the logarithmic profile, with too high velocity gradients, above which the velocity profile again returns to the slope of the near-wall RANS region. It is seen that the velocity shift is nearer the ground for mesh C than for mesh A. The unphysical shift happens at the height where the shear stress switches from being mainly modeled to being resolved. This demonstrates the traditional deficiency in ABL LES. Nikitin et al. [42] also observe this discrepancy from similarity forms using a similar model. The problem with excessive wind gradients, however, is not only observed in hybrid methods but is a general problem for LES of boundary layer flows, where wall functions are needed [36, 63].

When the simulation is run with backscatter model (solid lines) the velocity mismatch is reduced. The dimensionless wind-shear (seen on top of figure 26) still have an unphysical kink in the transition region, but the value has dropped noticeable from about 1.5 to 1.3 for mesh C. The velocity profiles from backscatter runs follow RANS simulations, run with the same model constants, reasonable well and are close to logarithmic.

On figure 27 profiles of the streamwise velocity variance are shown. Here it is seen that the maximum value of $\langle u'^2 \rangle / u_{*0}^2$, which is about 6, decreases slightly when the backscatter model is applied. Furthermore, the non-backscatter simulations show a very sharp peak in $\langle u'^2 \rangle / u_{*0}^2$ - this is reduced when backscatter is applied. This is similar to Mason and Thomson [36] who also found an unrealistic near-surface peak in the velocity variance. Mason and Thomson [36] explained that the near-surface peak was due to the excessive shear in the near-wall region and also found that it was removed with the addition of a backscatter model.

As shown, the addition of a backscatter model improves both the mean velocity profile and the turbulent variances. Without backscatter, an unphysical region is observed between the RANS region where all turbulent stresses are modeled and the LES region where most turbulent stress is resolved. When backscatter is included, turbulent structures are generated, which can carry turbulent stress - this reduces the unphysical transition region. The backscatter model is clearly capable of diminishing some of the LES discrepancies from the similarity forms and in the rest of this work, all LES simulations are run with backscatter model.

6.4 Results

All LES simulations of the ABL are started from RANS solutions computed with the same simulation parameters and boundary conditions. Since many authors are familiar with the $k - \epsilon$ RANS model, it only seems natural to compare the RANS and LES solutions. In this section, we first present the RANS results, and comparisons with LES are conducted afterwards.

RANS

The RANS results presented are performed with the parameters shown in table 8. Simulations are performed on mesh A, for varying values of roughness, z_0. In order to demonstrate that the RANS solutions are grid-independent, RANS simulations have been performed on successively refined grids. Using the EllipSys3D solver simulations can be performed on different grid levels, where grid level 1 is the most refined. By moving to grid level 2 the resolution is coarsened by removing every second cell in all directions. For higher grid levels the grids are coarsened accordingly. Figure 28 is an example of velocity profiles achieved for different grid levels, calculated on mesh A with $z_0 = 0.1m$. Grid level 3 is the coarsest resolution,

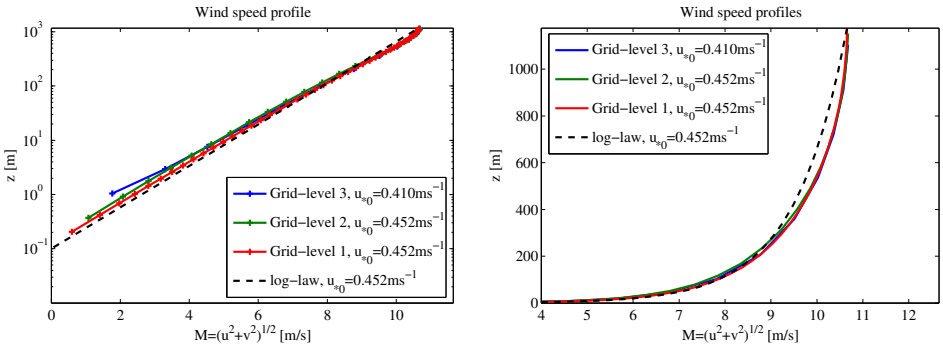

Figure 28. RANS velocity profiles for varying grid levels performed on mesh A. Grid-level 1,2 and 3 refers to $\Delta = 44.2m$, $\Delta = 88.4m$ *and* $\Delta = 176.8m$ *respectively. The predicted friction velocities,* u_{*0}, *are shown in the legend.*

while grid level 1 is the most refined. It is seen on the figure that even on grid level 3, the near-wall velocity profile is reasonable predicted. For grid level 1 and 2 the predicted friction velocity, u_{*0}, is the same ($u_{*0} = 0.452ms^{-1}$), why we conclude that solutions are grid-independent. From here on, all results presented are calculated on grid level 1.

Table 8. RANS parameters. Standard model constants are used (see table 1).

Mesh	*Scheme*	C_μ	C_b	z_0	$\triangle$t	u_g	v_g
A	CDS2	0.03	0.00	0.001m	1.00s	$10ms^{-1}$	$0ms^{-1}$
A	CDS2	0.03	0.00	0.030m	1.00s	$10ms^{-1}$	$0ms^{-1}$
A	CDS2	0.03	0.00	0.100m	1.00s	$10ms^{-1}$	$0ms^{-1}$
A	CDS2	0.03	0.00	1.000m	1.00s	$10ms^{-1}$	$0ms^{-1}$

As described in section 6.3, the level of turbulent kinetic energy for RANS simulations is determined by the value of C_μ, and is not affected by change in roughness. Because of this, only the mean velocity is presented. On figure 29, 30 and 31 the mean wind is shown in different ways. Figure 29 shows the dimensionless wind shear, Φ_m, in the lower part of the boundary layer ($z/h \leq 0.4$) for varying values of roughness. It is seen that Φ_m follow similarity theory ($\Phi_m = 1$) quit closely, with a maximum wind shear of $\Phi_m = 1.2$. To the left on figure 30 the Ekman spiral is shown. Here it is observed how the cross-isobaric angle, θ, increases with roughness. To the right of figure 30 the velocity profiles together with the determined friction velocities are shown. On figure 31 it is seen that the velocity profiles are indeed logarithmic in the surface layer. Above this height a slight speed-up is observed. A summary of the RANS results is shown in table 9.

Table 9. Predicted RANS values of cross-isobaric angle, θ, *friction velocity,* u_{*0}, *and similarity constants A and B from the geostrophic resistance laws.*

z_0	u_g	v_g	θ	u_{*0}	A	B
0.001m	$10.0ms^{-1}$	$0.0ms^{-1}$	9.1^o	$0.31ms^{-1}$	2.1	2.0
0.030m	$10.0ms^{-1}$	$0.0ms^{-1}$	12.9^o	$0.41ms^{-1}$	2.2	2.1
0.100m	$10.0ms^{-1}$	$0.0ms^{-1}$	18.2^o	$0.45ms^{-1}$	2.3	2.8
1.000m	$10.0ms^{-1}$	$0.0ms^{-1}$	21.8^o	$0.58ms^{-1}$	2.3	2.6

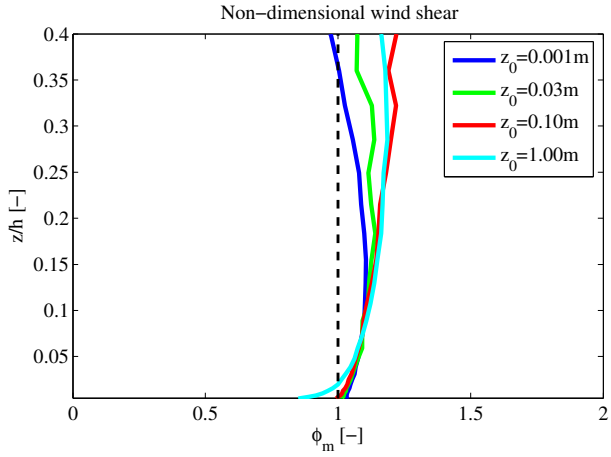

Figure 29. Dimensionless wind shear. RANS simulations are performed on mesh A with different values of z_0

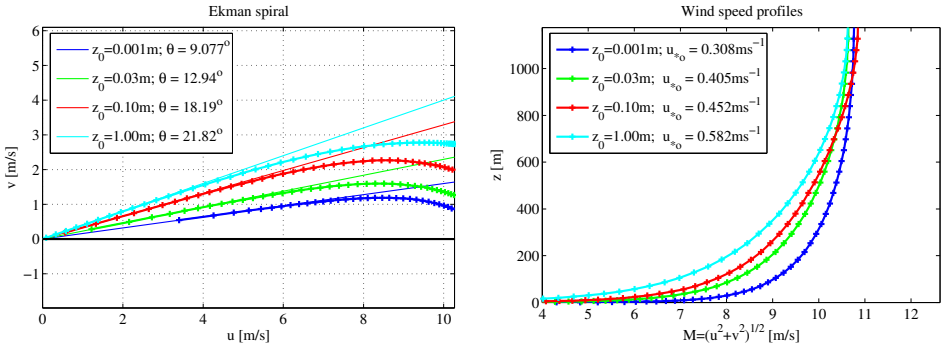

Figure 30. RANS. The Ekman spiral and velocity profiles for different values of z_0 but for the same geostrophic wind.

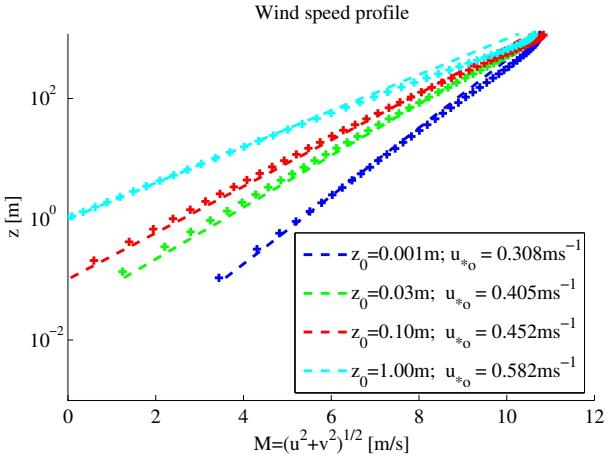

Figure 31. Logarithmic plot of velocity profiles for RANS simulation using different values of z_0 compared to the logarithmic law-of-the-wall (38).

LES

As described earlier, grid-dependency tests are seldom performed for LES. Because of non-linear interactions between numerical errors, a finer resolved simulation may not give the same solution for LES. Furthermore, even a relative coarsely resolved LES of the ABL is computational expensive. To investigate the effect of changing grid resolution, however, simulations have been performed on two computational grids - mesh A and mesh C. Table 10 shows the input parameters used for this test. LES simulations have also been performed with different values of roughness length, z_0, on mesh A (see bottom of table 10). These simulations will be compared with the RANS simulations.

Table 10. Top table: Input parameters for LES simulations performed on two meshes. Bottom: Parameters used for LES simulations with varying roughness. If parameters are not shown, then standard model constants are used (see table 1).

Mesh	*Scheme*	C_μ	C_b	z_0	$\triangle$t	u_g	v_g
A	CDS4	0.03	0.70	0.100m	1.00s	$10ms^{-1}$	$0ms^{-1}$
C	CDS4	0.03	0.70	0.100m	0.50s	$10ms^{-1}$	$0ms^{-1}$

Mesh	*Scheme*	C_μ	C_b	z_0	$\triangle$t	u_g	v_g
A	CDS4	0.03	0.70	0.001m	1.00s	$10ms^{-1}$	$0ms^{-1}$
A	CDS4	0.03	0.70	0.030m	1.00s	$10ms^{-1}$	$0ms^{-1}$
A	CDS4	0.03	0.70	0.100m	1.00s	$10ms^{-1}$	$0ms^{-1}$
A	CDS4	0.03	0.70	1.000m	1.00s	$10ms^{-1}$	$0ms^{-1}$

To investigate the effect of grid resolution for LES, we start by examining the turbulence models ability to capture the mean wind. Figure 32 shows the dimensionless wind shear for mesh A and C in the surface-layer. A characteristic kink is observed for the LES simulations between the region where the turbulent stresses are all modeled and the highly resolved region ($z/h \leq 0.03$). Since this transition region is governed by the mesh resolution, it is nearer the ground for mesh C than mesh A. Achieving a dimensionless wind shear near 1 is often the benchmark test case for LES simulations of the ABL. With a maximum dimensionless shear of 1.3 in the surface-layer the proposed model give acceptable results. Both mesh A and mesh C results are close to the results from RANS simulations.

The Ekman spiral and the velocity profiles shown on figure 33 are also in close agreement with the RANS simulations for both mesh resolutions. The LES simulations predict a slightly lower friction velocity compared to RANS. Figure 34 shows the velocity profiles on logarithmic scale. Again it is seen that the solutions on the two meshes and the RANS solution are in close agreement. In the surface-layer the velocity profile is logarithmic, and above this layer a speed-up is observed.

Figure 35 shows profiles of the three components of resolved velocity fluctuations (the variances) and the total resolved turbulent kinetic energy for the LES simulations. The streamwise component of turbulence compares well with the predicted values. It is seen that the maximum value of $\langle u' \rangle / u_{*0}^2$ is slightly larger for mesh C (=5.9) than for mesh A (=5.6), but overall good agreement is found. The vertical component of turbulence is seen to be slightly underpredicted. Slightly better results are obtained on the fine mesh C than the coarser mesh A. The maximum value of $\langle w' \rangle / u_{*0}^2$ for mesh C is 1.2 and 1.0 for mesh A. The transverse component fits prediction fairly well but is slightly overpredicted on mesh C. The maximum values of $\langle v' \rangle / u_{*0}^2$ for mesh C and A are 2.2 and 1.8, respectively. Because the vertical and streamwise components are slightly underpredicted, the

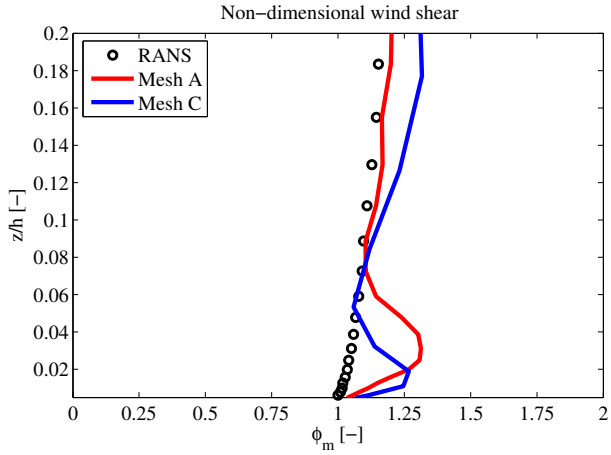

Figure 32. Dimensionless wind shear in the surface-layer for LES on mesh A and C compared with RANS simulation. $z_0 = 0.1m$

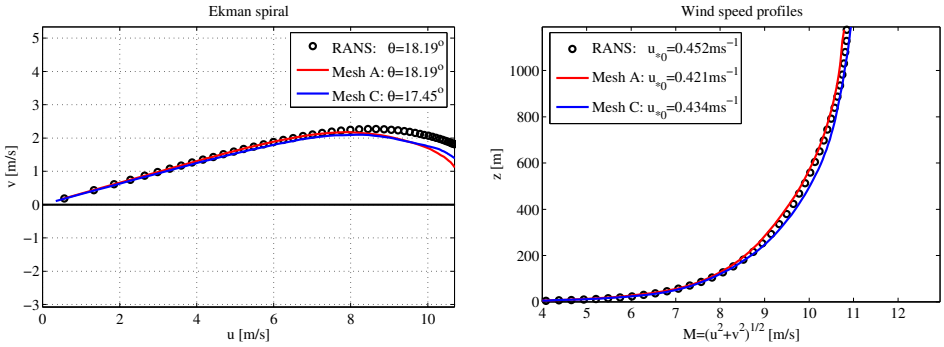

Figure 33. Ekman spiral and velocity profiles for LES performed on mesh A and mesh C. Results are compared with RANS simulations. $z_0 = 0.1m$

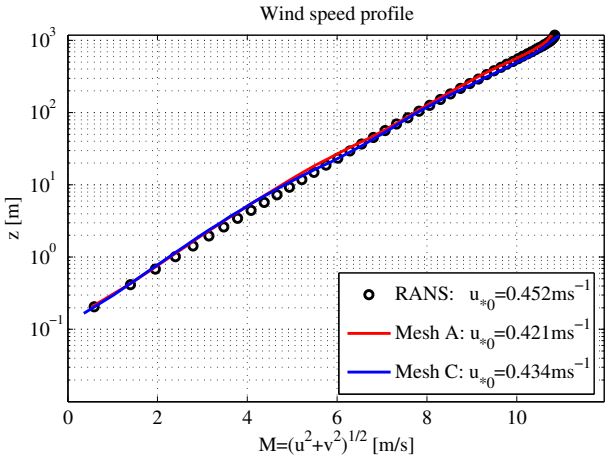

Figure 34. Velocity profile on logarithmic scale for LES compared with RANS simulation. $z_0 = 0.1m$

total turbulent kinetic energy is also slightly underpredicted. An exact comparison with atmospheric measurements is, however, difficult because these generally tend to show some scatter. Therefore, comparisons are often made with other LES simulations. Andren et al. [1] compared four different LES codes and found that the different SGS models resulted in values of $\langle u' \rangle / u_{*0}^2$ spreading from 5.6 to 7.1 (values are extracted from figure in [1]).

Figure 36 shows profiles of the shear stress, which is seen to decrease linearly with height. In the bottom of figure 36 the contribution of the resolved stress to the total is shown on a log plot. The height where half the shear stress is resolved for mesh A and C is $z = 29m$ and $z = 14m$ respectively. This gives an impression of the resolution needed, if flow around structures of engineering interest are to be simulated.

Figure 37 shows the normalized one-dimensional spectra of the streamwise velocity at different heights. The spectra are calculated by Fourier transformations of time series, which are averaged in the horizontal direction and are normalized with the local value of u_*. The straight lines show the theoretical slope of a Kolmogorov inertial range, $(f) \cdot f^{-5/3}$, and the slope of the energy production range, $(f) \cdot f^{-1}$. At the smallest scales a steep fall-off is observed. This spectral drop happens at frequencies considerable smaller than the Nyquist frequency. The highest resolved frequency is about $u/5\Delta$, which means that 5 computational cells are required to resolve a turbulent eddy. This spectral fall-off can only be explained by the implicit filtering of the numerical scheme that damps the smallest scales [25]. This damping is observed in other finite-volume LES results. Due to the limited grid resolution, the turbulent spectra from LES do not show the extended inertial range found in atmospheric measurements but we do observe a region with a slope of k^{-1}. In order to resolve the inertial range better a smaller computational domain with higher resolution could have been chosen. This would however mean the energy production scales would be less resolved.

LES simulations are also performed with varying values of surface roughness (see table 10). Because of computational cost these simulation are only performed on the coarse mesh A. Since simulation parameters are identical to the RANS results presented, it is interesting to compare the two. This is done on figure 38,39 and 40 where RANS results are denoted by circles and LES results by solid lines. In addition, the LES results are summarized in table 11.

Table 11. Predicted values of the cross-isobaric angle, θ, friction velocity, u_{*0}, and similarity constants A and B from the geostrophic resistance laws. Top table: LES results for simulations on mesh A and C with $z_0 = 0.1m$. Bottom table: LES results, for simulation with different values of z_0 performed on mesh A.

$Mesh$	z_0	u_g	v_g	θ	u_{*0}	A	B
C	0.100m	$10.0ms^{-1}$	$0.0ms^{-1}$	17.5^o	$0.43ms^{-1}$	1.9	2.8
A	0.100m	$10.0ms^{-1}$	$0.0ms^{-1}$	18.2^o	$0.42ms^{-1}$	1.6	3.0

$Mesh$	z_0	u_g	v_g	θ	u_{*0}	A	B
A	0.001m	$10.0ms^{-1}$	$0.0ms^{-1}$	11.1^o	$0.29ms^{-1}$	1.5	2.6
A	0.030m	$10.0ms^{-1}$	$0.0ms^{-1}$	14.9^o	$0.39ms^{-1}$	1.9	2.6
A	0.100m	$10.0ms^{-1}$	$0.0ms^{-1}$	17.8^o	$0.43ms^{-1}$	1.7	2.9
A	1.000m	$10.0ms^{-1}$	$0.0ms^{-1}$	25.5^o	$0.57ms^{-1}$	2.4	3.0

On figure 38 the velocity profiles and Ekman spirals for LES and RANS are shown. Here it is seen that LES predicts slightly larger values of the cross-isobaric angle, θ, than RANS. The non-dimensional shear for RANS and LES shown on fig-

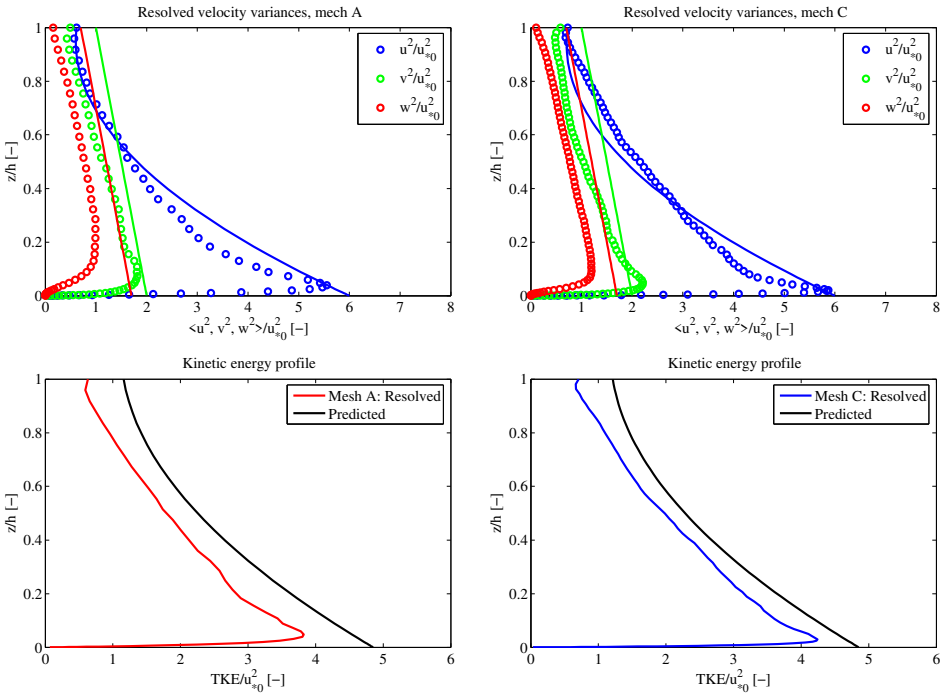

Figure 35. Top row: components of the resolved velocity variances from LES simulations (denoted by circles), compared with estimates (86),(87),(88), (denoted by solid lines). Bottom row: The total resolved turbulent kinetic energy. Left column are results on mesh A, right are from mesh C.

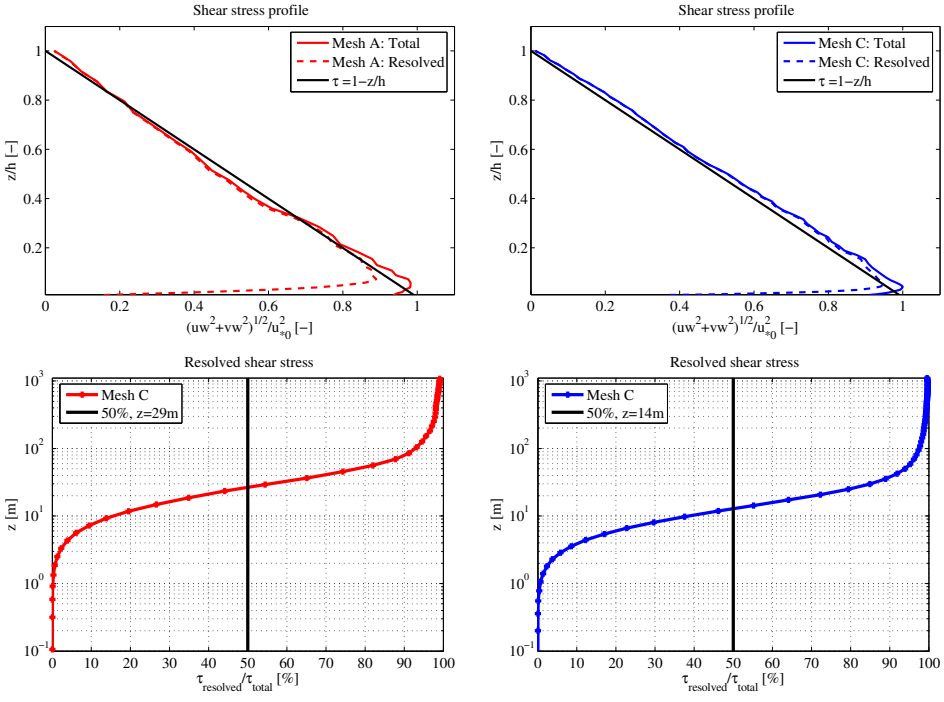

Figure 36. Top row: resolved and total profiles of Reynolds shear stress (horizontal momentum flux, (18)) for mesh A and C. Bottom row: contribution of the resolved stress compared to the total.

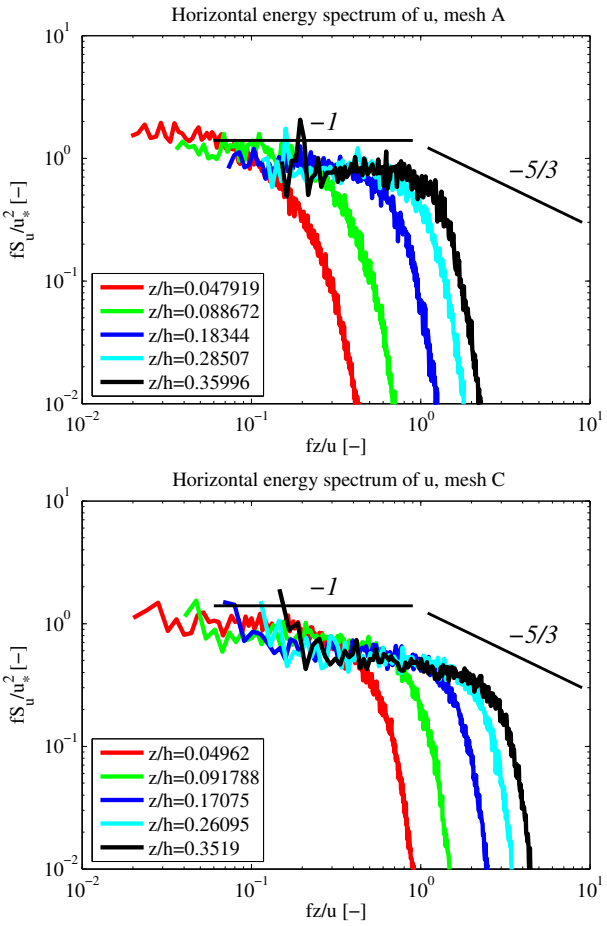

Figure 37. Streamwise normalized one-dimensional spectra of the streamwise velocity component. The spectra have been normalized with the local friction velocity and is plotted for different heights.

ure 39 are fairly similar, when the near-wall kink in the LES results is disregarded. If one compares the velocity profiles on the logarithmic plot (figure 40) RANS and LES is seen to agree closely. The predicted similarity constants A and B from the geostrophic resistance laws are shown in table 11. Except for the simulation done with $z_0 = 1m$ they are in reasonable close agreement giving an averaged value of A=1.7 and B=2.8. The difference for $z_0 = 1m$ might be related to the logarithmic law (38), which is not valid for large values of roughness.

6.5 Closure

In this chapter, the proposed turbulence model was validated by simulation of the neutrally stratified atmospheric boundary layer over a rough surface. The traditional problem of simulating high Reynolds number flows over rough surfaces was first described. Because wall-models are necessary, LES-simulations tend to behave unphysical near the wall. The proposed turbulence model run without the backscatter model, produce too high near-wall velocity gradients - a general trend found among many LES models. By applying the backscatter model the velocity gradients is reduced resulting in velocity profiles with a clear logarithmic region.

The importance of the model parameter C_μ was also discussed. C_μ should be chosen to ensure a correct level of modeled turbulent kinetic energy (TKE) in the near-wall RANS region. When C_Δ is chosen using (50), the LES turbulence model

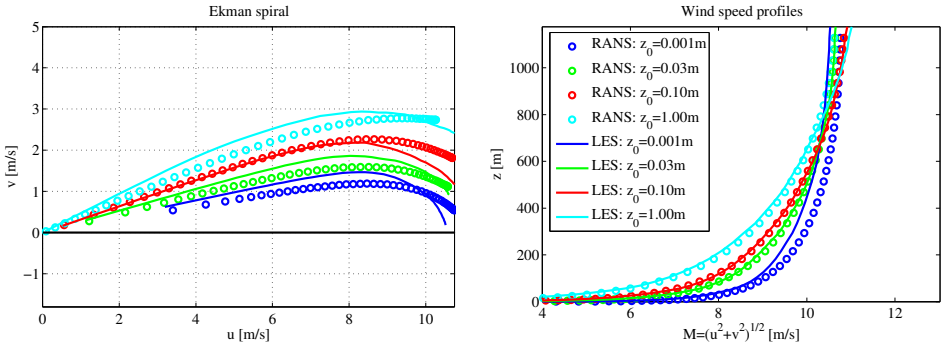

Figure 38. Left: Ekman spiral compared for RANS and LES. Right: Velocity profiles for RANS and LES

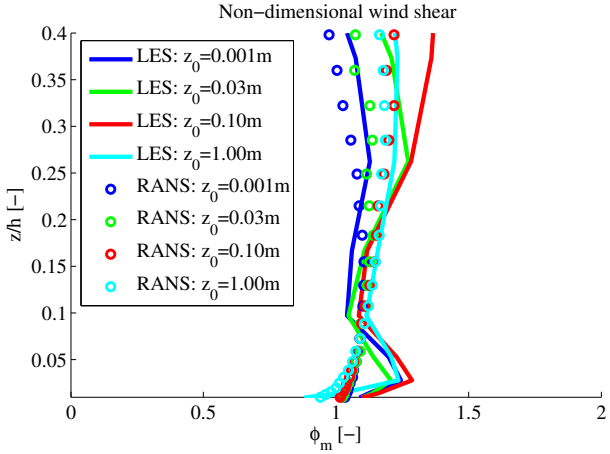

Figure 39. Non-dimensional wind shear for LES and RANS simulations performed with different roughness lengths. The LES results have been smoothed by using linear interpolation of neighboring points.

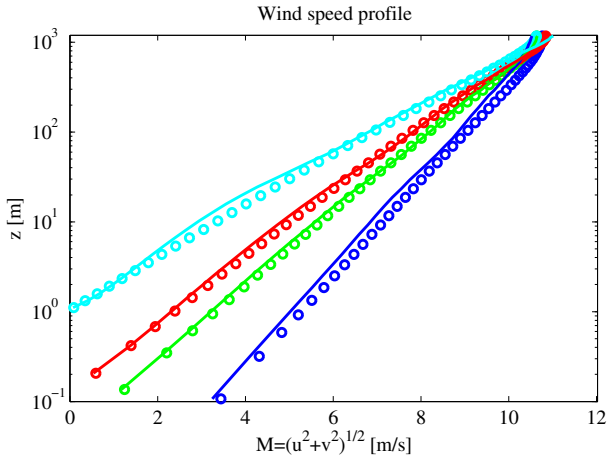

Figure 40. Logarithmic plot of the RANS and LES velocity profiles.

is independent of C_μ and works like Smagorinsky model. The modeled TKE is only accurate in the RANS region and is not representative for the SGS TKE in the LES region. Therefore, only the resolved TKE is presented for LES simulations.

A big advantage with the proposed turbulence model is that it can be run in both RANS- and LES-mode. Only one new simulation parameter, C_Δ, is necessary, otherwise the standard $k-\epsilon$ parameters can be used. Because of the simplicity in changing between the two methods both RANS and LES simulations can be performed and results compared. In general, RANS and LES mean velocity profiles showed good agreement and were relative independent on mesh resolution. More importantly, the LES results showed clear logarithmic velocity profiles in the surface-layer. Furthermore, the velocity variances also compared well with empirical relations throughout the ABL.

7 Simulation of the Askervein Hill

A difficulty when validating a turbulence model designed for atmospheric boundary layer flows, is the general lack of prober experimental measurements of flow over natural terrain. In order for an experiment to be applicable as validation case, thorough measurements are needed both at the location of interest and at upstream locations. Measurements should contain information on both mean wind and turbulence especially when validating a LES model. Furthermore, the conditions at which the wind measurements are taken, such as effects of thermal stratification and orthography, must be thoroughly documented.

Probable the best known and best documented field campaign is that performed in 1982 and 1983 over the Askervein hill located at the Hebrides in Scotland [66, 67]. The Askervein hill's highest point is 116m above the surroundings and its planform is almost elliptic with major axis of about 1km and 2km. Even though the hill hardly can be termed as complex, complex phenomena, such as recirculation zones in the lee-side of the hill, have been observed. Furthermore, nearby downstream hills may influence the wind around the Askervein hill. Contrary to many measurements of atmospheric flow over hills the Askervein hill project provide valuable turbulence measurements, which can be used for comparison with simulations. These kinds of measurements are normally restricted to laboratory scales - not atmospheric scales. Therefore, despite the relative simple geometric appearance of the Askervein hill, earlier wind simulations [10, 13, 56, 70] have proved it to be a challenging test case, and it is valuable for validating the proposed turbulence model.

In the previous chapter we demonstrated the proposed LES model's ability to simulate the flat and neutrally stratified ABL. Now we turn to flow over hills. This chapter describes how the wind simulation over the Askervein hill is performed and both LES and RANS results are discussed and compared with measurements. For an overview of "The Askervein Hill Project" see Taylor and Teunissen [65].

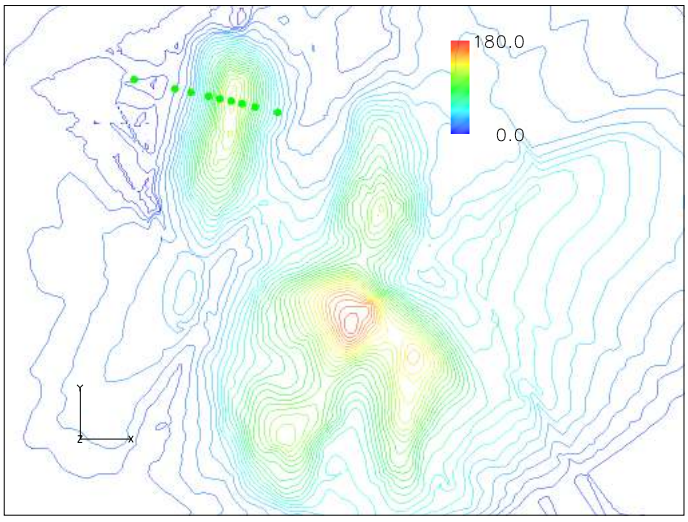

Figure 41. Elevation contour (m) plot of the Askervein hill and the surrounding terrain used in simulations. The measurements used were taken along line A (denoted by green dots).

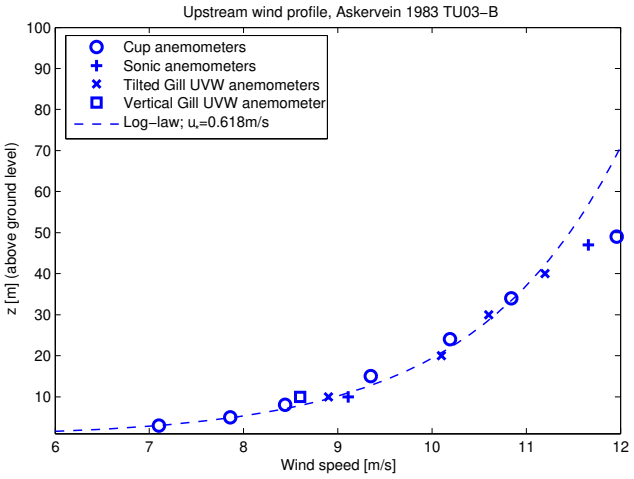

Figure 42. Mean velocities measured at RS for the TU-03B run. A logarithmic velocity profile has been fitted, $u_{*0} = 0.618ms^{-1}$, $z_0 = 0.03m$.

7.1 Problem description

Figure 41 shows the digitized contour lines of the Askervein hill and the surrounding terrain. The map has been oriented so that the x-axis is aligned with the mean flow direction at the time of measurements (210^oN). Nine dots are shown on the figure. They are located along a line (line A) going from southwest to northeast and represent the location of measuring instruments. At these locations measurements of turbulence, mean wind speed and direction were made in a height of 10m - these measurements will be used for validating the LES solver. Line A intersects with the Askervein hill's highest point (HT) 126m above the sealevel (116m above surroundings). The Askervein hill is relatively isolated apart from the hills observed downstream. Upstream there is a uniform and flat fetch of about 4km to the coastline. 3km upstream, a reference site (RS) is located where measurements of the "undisturbed" flow has been taken. During the measuring campaign [66, 67], 50m towers was placed at HT and RS in order to measure vertical wind profiles.

To perform LES of the Askervein hill a wind field that matches the one measured at RS will be generated by running a precursor simulation as described in the previous chapter. This windfield is then used as inflow for the actual Askervein simulation (the successor), where the inflow boundary is located at RS. We follow [10, 13, 56, 70] and compare results to field measurement TU-03B of Taylor and Teunissen [67] taken on October 3, 1983, where the atmosphere was nearly neutrally stratified. This is the most commonly used dataset. In order to evaluate LES results a reference RANS simulation is also performed. This RANS simulation is run on the same mesh as the LES simulation, but will not use a precursor to generate inflow. Instead, a velocity profile is specified at the inlet.

In order to compare the mean wind from measurements and simulations we define the speed-up, ΔS, as the difference between the local wind speed and the undisturbed reference wind speed normalized with the reference wind speed,

$$\Delta S = \frac{M(z') - M_{ref}(z')}{M_{ref}(z')}. \tag{93}$$

here z' is the local height over terrain and M is the velocity in horizontal direction. The reference velocity $M_{ref}(z')$ is taken at RS for the measurements and at the computational inlet for simulations. Turbulence variances are normalized with the same reference wind speed squared.

7.2 Experimental data

The measurements used to validate results, were averaged over a three hour period on October 3, 1983. The specific run number for the measurements is designated TU-03B [67], and was taken under strong winds. During the three hour period, mean wind at RS was $8.9ms^{-1}$ at 10m above ground level and friction velocity was about $u_{*0} = 0.57ms^{-1}$ (both measured with tilted Gill UVW anemometer). The undisturbed windprofile measured at RS is shown on figure 42 with the used instrumentation.

Using a surface roughness value of $z_0 = 0.03m$ (the suggested value by Taylor and Teunissen [65]) a logarithmic profile has been fitted to the measurements using $u_{*0} = 0.618ms^{-1}$. As seen there is some scatter around the logarithmic profile. At heights above 40m the measured windprofile shows a change in slope compared to the logarithmic profile, this might be related to the upstream costal boundary layer [39]. The vertical anemometer placed at RS at $z = 10m$ measures a mean velocity of $M = 8.6ms^{-1}$. This is the instrument used along line A and $M = 8.6ms^{-1}$ is therefore used as reference velocity when normalizing measurements along line A. The cup anemometers on figure 42 were placed on a 50m high tower. A similar tower was set up at HT. When investigating the speed-up at HT the measurements will be normalized with the cup anemometer measurements from RS. The measurements used for validation are shown in Table 12 and 13, where wind direction and the three components of turbulence are also shown.

Table 12. Measurements taken along line A at 10m above ground level. Run no: TU03-B [67], AES vertical Gill uvw anemometer.

dist. HT $[m]$	Direction $[^o]$	Upwash $[^o]$	Speed $[ms^{-1}]$	$\langle u' \rangle$ $[ms^{-1}]$	$\langle v' \rangle$ $[ms^{-1}]$	$\langle w' \rangle$ $[ms^{-1}]$
RS	207.3	2.5	8.6	1.223	0.704	0.413
-850	201.6	3.9	7.8	1.200	0.762	0.463
-500	192.9	2.8	6.7	1.350	0.683	0.475
-350	196.0	11.5	7.2	1.243	1.038	0.580
-200	200.6	16.0	10.5	1.115	1.126	0.565
-100	207.9	14.5	13.2	1.059	1.232	0.577
HT	203.4	2.7	16.2	1.100	1.034	0.577
100	206.5	−11.1	12.0	1.758	1.012	0.531
200	195.9	−13.0	5.6	2.560	1.502	0.881
400	188.1	−5.7	3.0	1.983	1.798	1.192

Table 13. Measurements from RS and HT. Run no: TU03-B [67], AES cup anemometers.

Height $[m]$	Speed (RS) $[ms^{-1}]$	$\langle u' \rangle$ (RS) $[ms^{-1}]$	Speed (HT) $[ms^{-1}]$	$\langle u' \rangle$ (HT) $[ms^{-1}]$
3	7.10	1.42	15.71	1.45
5	7.86	1.37	16.38	1.38
8	8.44	1.42	16.30	1.17
15	9.35	1.27	16.63	1.04
24	10.19	1.23	16.15	1.19
34	10.84	1.16	15.77	1.17

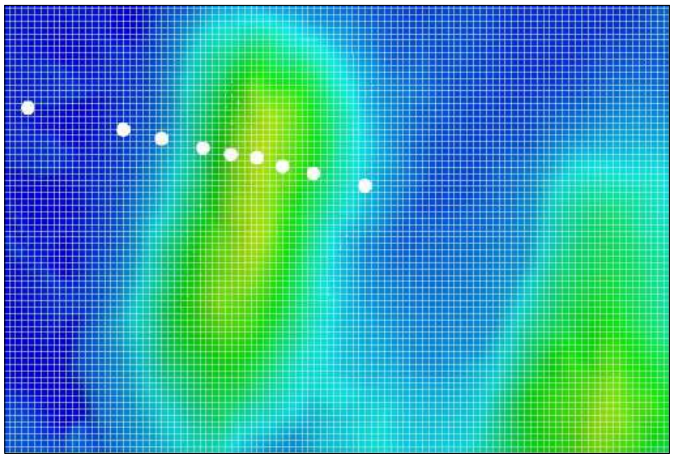

Figure 43. Horizontal meshing applied. Close-up of the Askervein hill

7.3 Numerical aspects

Computational mesh

Two computational meshes are necessary - one for the precursor and one successor. The purpose of precursor simulation is to generate an inflow windfield similar to the one measured. To avoid spatial interpolation we generate the precursor mesh so that it exactly matches the inflow boundary of the successor.

Following (61), the domain height for $u_{*0} = 0.618ms^{-1}$ should be about H=1850m. In order to achieve higher mesh resolution, however, a slightly smaller domain height has been chosen, H=1500m. We consider this slightly lower domain height sufficient to avoid affects from the upper boundary on the hill flow [56]. The length of the precursor mesh is 8.9km and the width 5.6km, thereby roughly achieving our recommended domain dimensions (6H×4H×1H). The EllipSys3D code uses terrain-following coordinates, which makes it possible for the computational boundary of the successor to follow the topography. To generate the successor mesh, contour lines of the Askervein hill and the surrounding area has been digitized. Two contour maps have been used - a high resolution map of the Askervein hill only, and a coarser map that also includes the neighboring hills on the leeside of Askervein. The elevations of these maps were interpolated to a horizontal resolution of 23.3m using 240×240 grid points that covers a square area of $5.6 \times 5.6km$. Downstream of this area the domain length is increased by additional 48 grid points that are stretched so that the total length of the successor domain is 8.8km. This extra length provides a buffer zone between the Askervein hill and the outlet. A closeup of the grid points are shown on figure 43.

For both precursor and successor we use a constant roughness length of $z_0 = 0.03m$ and the height of the first near-wall computational cell is put equal to z_0. The mesh is stretched upward using 96 grid points by the method described in section 4.4, using a hyperbolic mesh generator [57]. The vertical mesh spacing over the Askervein hill is shown on figure 44.

Because of the finite resolution of the computational mesh the height of the digitized Askervein hill has reduced from 126m to 124m. The height above sealevel at the inlet, corresponding to the reference site, is about 5m. For both precursor and successor a symmetry boundary condition is used at the top of the domain. Cyclic conditions are used on all four horizontal planes except for the successor mesh, where inflow and outflow conditions are used in the flow direction. The successor mesh is shown on figure 45 and mesh details are given in table 14.

Figure 44. Left: The vertical meshing applied over the Askervein hill. The foreground has been taken from a photograph. Right: Photograph taken from an upstream location of the Askervein hill.

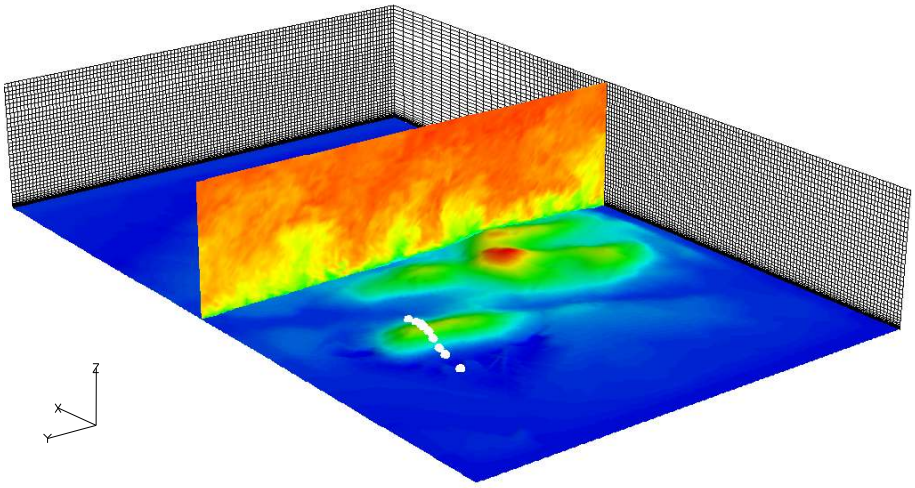

Figure 45. The Askervein mesh. The figure gives an impression of the domain dimensions. The Askervein hill is placed slightly to the left in order to make room for the downstream hills. A cross sectional plane shows the instantaneous contours of wind speed. Only every second grid point is shown

Table 14. Domain sizes and mesh details. The domains of sizes (L,W,H) are partitioned into (N_x,N_y,N_z) grid cells. z_1 is the average height of the first near-wall grid cell, and S is the maximum stretching ratio applied to the mesh near the wall. In the horizontal direction the Askervein successor mesh uses equidistant mesh spacings for the first 5.6km (240 cells) whereafter the cells are coarsened towards the outlet.

Mesh	L [km]	W [km]	H [km]	N_x [-]	N_y [-]	N_z [-]	$\triangle$ [m]	S [-]	z_1 [m]
Askervein successor	8.8	5.6	1.5	288	240	96	23.3	1.20	0.03
Askervein precursor	8.9	5.6	1.5	384	240	96	23.3	1.20	0.03

Simulation parameters

In order to have a reference simulation, both RANS and LES simulations are run, using the same model constants. The turbulence intensity ($\langle k \rangle^{0.5}/M_{10m}$) at RS was measured to 0.12 (see table 12). Using the logarithmic profile (38) with $u_{*0} = 0.618ms^{-1}$ ($M_{10m} = 9.0ms^{-1}$) the constant C_μ can be determined using (48) and $C_{\epsilon 1}$ and C_Δ is determined by (49) and (50),

$$C_\mu = \left(\frac{u_{*0}^2}{\langle k \rangle}\right)^2 = \left(\frac{0.618^2}{1.16}\right)^2 = 0.11 \tag{94}$$

$$C_{\epsilon 1} = C_{\epsilon 2} - \frac{\kappa^2}{C_\mu{}^{\frac{1}{2}}\sigma_\epsilon} = 1.55 \tag{95}$$

$$C_\Delta = C_s C_\mu^{-3/4}\frac{C_{\epsilon 1}}{C_{\epsilon 2}} = 0.61 \tag{96}$$

Table 15 gives an overview of the used model constants.

Table 15. Model constants for simulations of the Askervein hill. For RANS $C_b = 0$.

C_μ	$C_{\epsilon 1}$	$C_{\epsilon 2}$	σ_k	σ_ϵ	C_b	C_Δ
0.11	1.55	1.92	1.00	1.30	0.70	0.61

No precursor is run for the RANS simulation. Instead we follow Sørensen [56] and specify the inlet velocity as logarithmic with a roughness length equal 0.03m and $u_{*0} = 0.618ms^{-1}$. Furthermore, the turbulent kinetic energy and dissipation of turbulent kinetic energy are specified by relation (77) and (78):

$$\langle k \rangle = \frac{u_{*0}^2}{C_\mu^{1/2}} \tag{97}$$

$$\langle \epsilon \rangle = \frac{u_{*0}^3}{\kappa z} \tag{98}$$

7.4 Results

Inflow turbulence - precursor

In order to generate inflow for the LES successor simulation a precursor simulation is run. The precursor is run using a constant pressure gradient corresponding to a geostrophic wind of $(u_g, v_g) = (16.8, -3.9ms^{-1})$, using the horizontal components of the Coriolis forcing. The simulation methodology is the same as described in chapter 6. The parameters used are shown in table 16.

Table 16. Input parameters for the precursor

Mesh	*Scheme*	C_μ	C_b	z_0	$\triangle$t	u_g	v_g
Precursor	CDS4	0.11	0.70	0.03m	0.30s	$16.8ms^{-1}$	$-3.9ms^{-1}$

The precursor results are shown on figure 46. It is seen that the mean velocity profile is nearly logarithmic with $u_{*0} = 0.602ms^{-1}$ - this is close to the targeted velocity profile of $u_{*0} = 0.618ms^{-1}$. The turbulence intensity at 10m is about

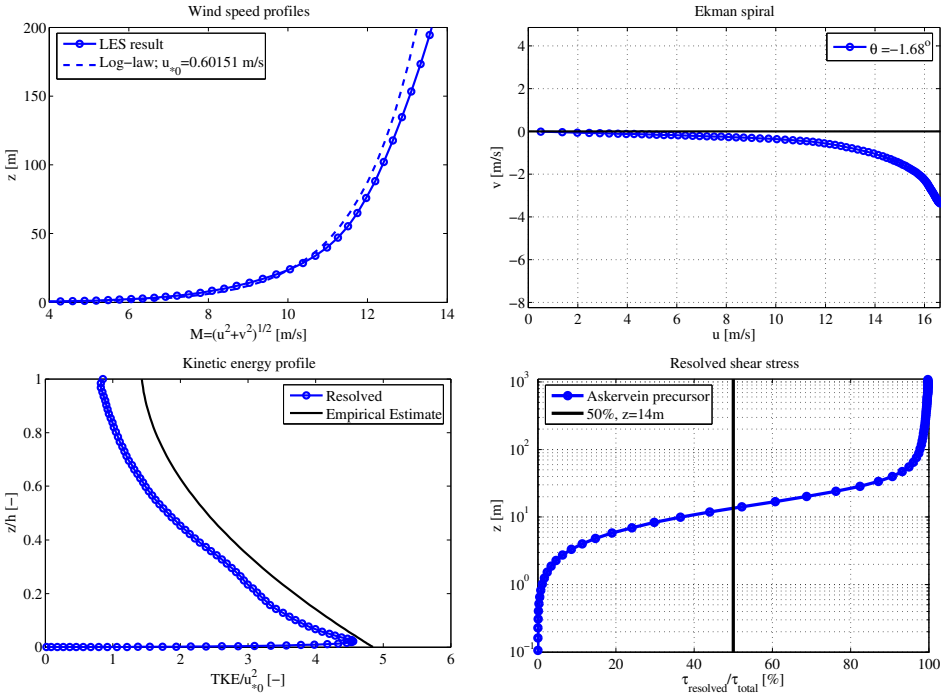

Figure 46. Precursor results for the Askervein hill. Top-left: Surface-layer velocity profile compared to a logarithmic profile, $u_{*0} = 0.602ms^{-1}$. Top-right: Ekman spiral. Surface-layer velocity is nearly along x-axis. Bottom-left: Profile of resolved turbulent kinetic energy. Bottom-right: Amount of resolved shear stress compared to the total.

0.16, which is a bit higher than the experiment. According to Taylor and Teunissen [67], however, the turbulence measurements taken by Gill anemometers are likely to be underestimated by up to 20%. Near the surface, the mean velocity is directed along the x-axis and the wind field can therefore be used directly for the successor simulation. Only about 50% of the shear stress is resolved in 10m heights, where most measurements are taken. It would have been favorable with a mesh of higher resolution in order to achieve a higher part of resolved shear stress. Due to computational costs, however, higher resolution cannot be achieved without decreasing the domain size and thereby limit the size of the largest turbulent structures.

In order to attain a fully developed turbulent boundary layer, the precursor was run for about 250,000 iterations before the wind field for the successor could be sampled. Using 40 processors the CPU time for the precursor was about 1 month.

Wind over the Askervein hill - successor

The input parameters for the successor are identical to the ones used for the precursor (see table 16). 80 minutes of turbulence from the precursor is saved and used as inflow for the LES successor simulation. The successor is allowed 40 minutes of spin-up time before results are sampled. The presented results are averaged over the final 40 minutes of time series taken at discrete locations corresponding to the measurements. 40 minutes of sampling time was found to be the minimum, in order to achieve prober mean values of velocity and turbulence. The wind profile at RS averaged over the 40 minutes is shown on figure 47. As seen, the mean wind for the LES simulation is reasonably close to the measured. At 10m height the mean wind is $8.4ms^{-1}$ - this is used as reference velocity when normalizing LES

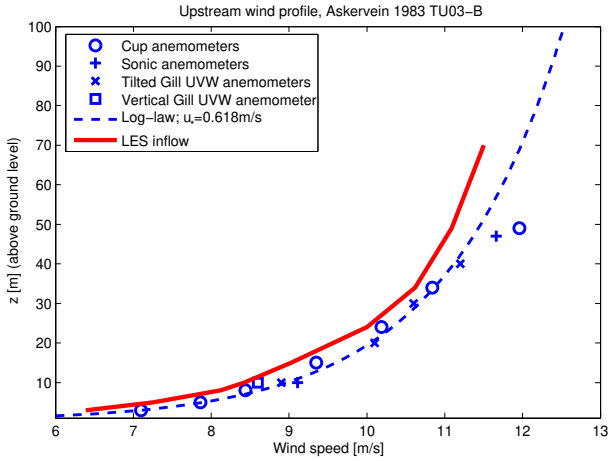

Figure 47. The inflow wind profile for the successor simulation (LES) compared to measurements. The profile is taken at RS in the simulation. For the RANS simulation the logarithmic profile shown was used at the inlet.

results along line A.

The comparison of measured and simulated speed-up along line A and at the hill top is shown on figure 48. Overall the RANS simulation is seen to predict the speed-up along line A reasonably well and is in close agreement to Sørensen [56] that uses the same CFD-solver. Upstream of the hill top the measured speed-up is captured and in the lee-side of the hill RANS reproduces the flow deceleration. RANS does, however, underpredict the speed-up at the hill top, $\Delta S = 0.77$, compared to the measured value of 0.88. This result was also found by Sørensen [56]. For the LES simulation, the hill top speed-up is captured reasonable accurately (S=0.92). As seen in the bottom of figure 48 the calculated speed-up is close to the measured for all heights at HT. Upstream of the hill the LES simulation, slightly overpredicts the speed-up and 400m downstream the model clearly underestimates speed-up. 400m after the hill top the LES simulation predicts a recirculation zone and a too low value of the speed-up. One reason for this underprediction may be related to the questionable validity of using a logarithmic wall-law in a separated flow region. However, Castro et al. [10] describe the Askervein flow as being on the verge of forming a recirculation zone. They find that the forming of a recirculation zone is very dependent on numerical parameters, and also find too low values of speed-up for their high resolution meshes. Castro et al. [10] describes that the deviations from measurements may be related to lower values of roughness found at the hill top during measurements, and do indeed get improved results for simulations with lower values of z_0.

Unfortunately, simulations with varying roughness' have not been performed and we are unaware if this would indeed improve the lee-side prediction. If, however, the measuring point after 400m is discounted the general agreement is good.

The mean wind direction and upwash is shown on figure 49. 400m after the hill top the mean wind speed for the LES simulation is close to zero and wind direction is therefore difficult to determine. Except for this point the RANS and LES simulations are in close agreement. It should be noted, that the LES results are only sampled at the discrete locations corresponding to the measurements (table 12). The LES sampling is therefore much coarser than for RANS. Even though the overall trend is indeed captured, the models do not completely agree with the observed wind.

Figure 50 (top) compares the computed TKE with the measured. For LES only

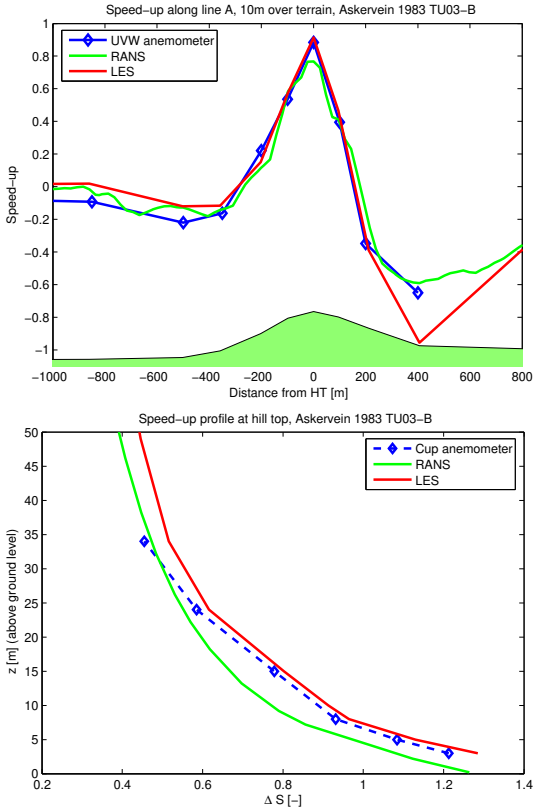

Figure 48. Comparison of measured velocity speed-up to simulated values along line A (top) and at hill top (bottom).

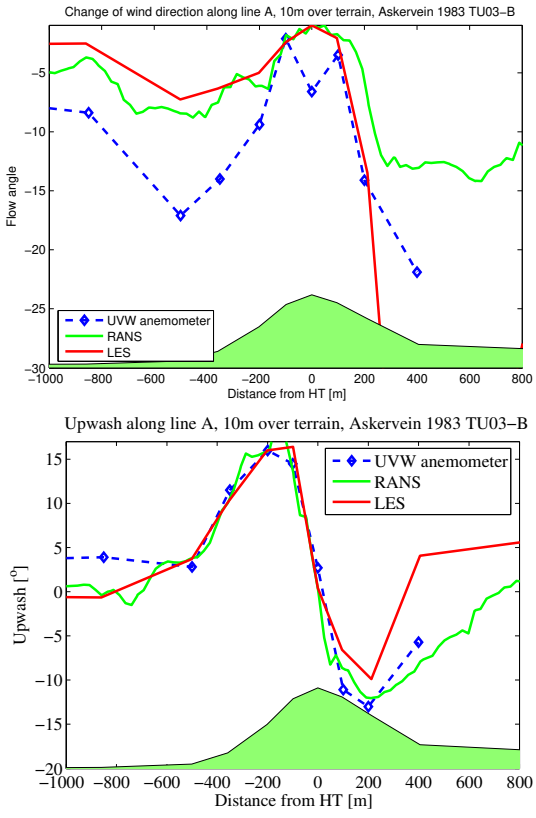

Figure 49. Top: Comparison of measured and simulated wind direction deviation from 210°. Positive in counter-clockwise direction. Bottom: Upwash along line A.

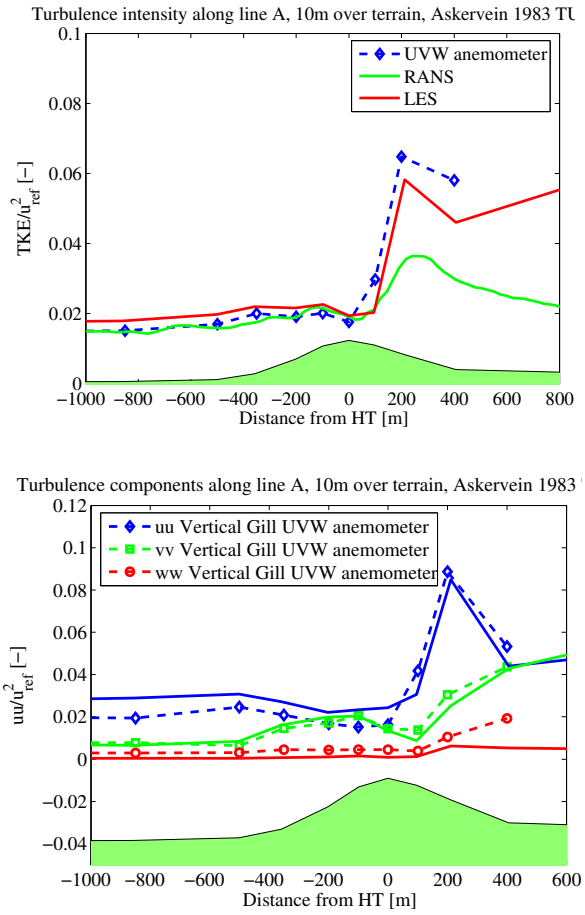

Figure 50. Top: comparison of TKE along line A with experiment. For LES only the resolved part is shown. Bottom: The turbulent velocity variances for LES simulation.

the resolved contribution is shown. Upstream of the hill the RANS model captures the TKE well but underpredicts after the hill top. For the LES simulation the level of TKE for the inflow turbulence was higher than for the measurements, therefore the overall level of TKE along line A is also slightly too high. It is, however, seen that the LES model predicts the turbulence increase after the hill top well. Figure 50 (bottom) shows the three components of turbulence (the three velocity variances) for the LES simulation. These are also seen to follow experiments very well. This information cannot be extracted from the RANS simulation. The LES results along line A is summarized in table 17.

7.5 Closure

Having tested the presented turbulence model over flat terrain in the previous chapter, this chapter deals with the wind over the Askervein hill. The topography of the Askervein hill is not complex but is chosen because of the well documented measuring campaign performed in 1982 and 1983. These measurements provide valuable information needed for validation of simulation results. More specifically, the dataset, TU-03B, is used, because it provides turbulence measurements. The measurements were collected along a line (line A) that intersects the Askervein hill's highest point.

Maps of the Askervein hill were digitized and a computational mesh (the suc-

cessor mesh) was generated using terrain following coordinates. The topography of nearby hills was included. For LES simulations an additional computational domain was needed to generate the turbulent inflow for the actual Askervein hill simulation. The generated turbulent inflow quite closely matched the undisturbed profile from measurements. For the RANS simulation the velocity was specified at the inlet to the successor mesh. All simulated results were averaged over 40min. Since different 10min averages shows large scatter in calculated mean velocities, 40min timeseries seem to be the minimum.

The RANS simulation reproduced the results obtained earlier using the same CFD-solver. RANS was shown to underpredict speed-up on the hill top but did otherwise reproduce the speed-up measurements quite closely. For the RANS simulation it was possible to specify the inlet turbulence intensity. Upstream of the hill the predicted value of turbulent kinetic energy therefore matched the measurements quite closely. Downstream, however, RANS underpredicted the turbulence level.

Except for the point 400m downstream of the hill top, the LES model showed to be able to capture the speed-up well. The windprofile at the hill top was captured closely. 400m downstream, however, the LES model predicted a recirculation zone not observed in measurements. Similar results have been observed in other LES simulations. One explanation for this discrepancy could be that the actual wind over the Askervein hill is on the verge of separation. This separation is somehow triggered in the numerical simulation, perhaps because it uses a different surface roughness. Since the turbulence model is designed to handle flow in complex terrain, the lee-side discrepancy between measurements and simulation could be problematic, since the lee-side may influence prediction of flow around downstream hills. The LES results do, however, show good agreement with measurements when comparing turbulent kinetic energy and the individual variance components of velocity fluctuations. Overall, results compare well with measurements and the speed-up discrepancy is restricted to a single measuring point. However, further investigations are necessary in order to validate model behavior for complex flows.

Table 17. LES results taken along line A at 10m above ground level. Results are rotated so that u is directed along the local mean wind, v is transverse and w is in the vertical direction.

dist. HT $[m]$	Direction $[^o]$	Upwash $[^o]$	Speed $[ms^{-1}]$	$\langle u' \rangle$ $[ms^{-1}]$	$\langle v' \rangle$ $[ms^{-1}]$	$\langle w' \rangle$ $[ms^{-1}]$
RS	207.3	0.1	8.4	1.328	0.736	0.166
-850	207.5	−0.7	8.6	1.437	0.683	0.167
-500	202.7	3.7	7.4	1.481	0.773	0.161
-350	203.7	10.0	7.4	1.390	1.071	0.220
-200	205.0	16.0	9.7	1.257	1.194	0.278
-100	207.6	16.5	13.3	1.293	1.205	0.322
HT	209.0	0.5	16.1	1.319	0.979	0.246
100	207.9	−6.5	12.3	1.478	0.787	0.295
200	196.5	−10.2	5.1	2.461	1.343	0.667
400	112.1	4.1	0.4	1.771	1.748	0.555

8 Simulation of Wall Mounted Cube

Since atmospheric measurements of wind over complex terrain are sparse, a wind tunnel experiment of the flow about a wall mounted cube has been selected as test case. The flow is highly complex with several recirculation zones and contrary to streamlined bodies, like the Askervein hill, separation points are clearly defined by the sharp edges of the cube. Simulation of a wall mounted cube is therefore a good test case for validating the turbulence model's ability to capture the physics of the separated shear layers and complex wake regions behind bluff bodies.

The wind tunnel measurements by Castro and Robins [11][53] has been chosen to compare with simulation results, since they provide investigations of thick boundary-layer flows at relative high Reynolds numbers ($Re \approx 10^5$). The experiment therefore resembles atmospheric conditions. We consider the wall mounted cube an important validation case since it resembles flow over complex terrain and flow in the vicinity of large buildings. LES seems suitable to handle this kind of flow. For RANS the time-averaging applied and the use of the isotropic eddy-viscosity to model all the turbulent stresses, could lead to difficulties when simulating the transient and highly anisotropic flow around bluff bodies. Since LES accurately simulates most of the turbulent stresses, better results are expected.

Simulations of laboratory experiments are convenient since the boundaries are clearly defined. Measurements of flow about a cube in natural wind have, however, been performed, see Hoxey et al. [20], Richards and Hoxey [49], Richards et al. [51]. Numerical studies of flow past cubic obstacles can be found in Baetke and Werner [3], Richards and Quinn [50], Sørensen [56], Thomas and Williams [68], Wright and Easom [72], Yakhot et al. [73], while Ferziger and Peric [17] and Martinuzzi and Tropea [33] give a general description of the flow characteristics of the surface mounted cube.

8.1 Problem description

Even though the important length and timescales of the experiment [11] are different from the atmospheric scales dealt with previously, we reproduce the experimental scales, in order to make direct comparisons possible. The cube of height, $h_c = 0.2m$, is placed in a 2m high boundary layer, with the mean onset flow perpendicular to one of the cube faces. As seen on figure 51 the coordinate system is arranged with the x-axis aligned along the streamwise direction and the z-axis in the vertical while the center of the cube floor is placed at (x,y,z)=(0,0,0).

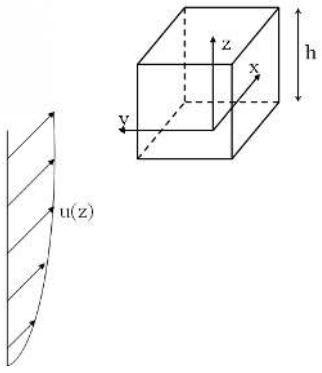

Figure 51. Problem setup showing the coordinate system and the onset flow.

The sharp edge at the rear of the cube (x=0.5h) allows shedding of small-scale vortices, which must be resolved. The computational grid therefore need to be refined in the vicinity of the cube walls to capture these structures. The computational domain must also be large enough so that near-cube flow is unaffected by domain boundaries. Both LES and RANS simulations are performed on the same numerical mesh.

At the domain inlet the equation variables must be specified. The inlet conditions for both LES and RANS are generated by running precursor simulations in a computational domain with a rough surface and cyclic horizontal boundary conditions. The fully developed equilibrium flows for both RANS and LES are saved and can subsequently be used as inflow for the successor simulations. When simulating flow about the surface mounted cube, it is important to distinguish between measurements performed with uniform onset flow from those performed within a boundary layer. One difference is the surface pressure distributions on the cube, which for the two are found to be markedly different [11]. Since we are mostly interested in atmospheric conditions, only thick boundary-layer flows are considered. Besides comparing the surface pressure from experiment and simulations, comparisons of downstream velocity and turbulence profiles are also performed.

8.2 Experimental data

Most wind tunnel studies use uniform onset flow, meaning that the level of turbulence intensity is low and that the boundary layer is very thin. In order for a wind tunnel experiment to resemble atmospheric conditions, special care must be given to the inflow. Castro and Robins [11][53] investigated the flow about a surface mounted cube in both uniform flow and in a simulated atmospheric boundary layer. Their wind tunnel measurements will be used as validation case.

The experiment was conducted in a $21.0 \times 9.1 \times 2.7m$ ($L \times W \times H$) wind tunnel. A cube of height, $h_c = 0.2m$, was installed on a false floor, which limited the height of the working section to H=2m. The cube height is thus one tenth of the boundary layer height $H = 10h_c$. The false floor was covered with roughness elements to simulate a roughness length of $z_0/h_c = 0.02$. The experiment was undertaken in order to investigate flow and plume behavior in the vicinity of large buildings [53]. In this view the experiment can be considered a 1/300 scale of a 60m high building in a 600m deep neutrally stratified boundary layer. Measurements of velocity, turbulence and surface pressure were conducted.

Since atmospheric conditions are most relevant for this work we only consider the measurements where the inflow resembles atmospheric conditions - in [11] this is referred to as case B. For this case a characteristic Reynolds number should be based on the mean onset velocity at cube height, u_h, the cube height, h_c, and the molecular viscosity

$$Re = \frac{u_h h_c}{\nu} \tag{99}$$

All surface pressure measurements were made at Reynolds numbers higher than $Re = 10^5$, and no Reynolds number dependency was experienced. Measurements in the wake of the cube were done at lower Reynolds numbers ($Re > 3 \times 10^4$) but again no Reynolds number effects were discernible. In order to allow the use of all measurements the presented simulations are performed at $Re = 10^5$. If a logarithmic velocity profile (38) is assumed then $u_{*0} = 0.77ms^{-1}$

The turbulence level, $TKE/u_{*0}^2 = 5.3 - 6.6$, was measured at $z/H = 0.05$ in the undisturbed onset flow [53]. Using (48) it is found that this is equivalent to $C_\mu = 0.023 - 0.036$ - close to the standard value of $C_\mu = 0.03$. Simulations will

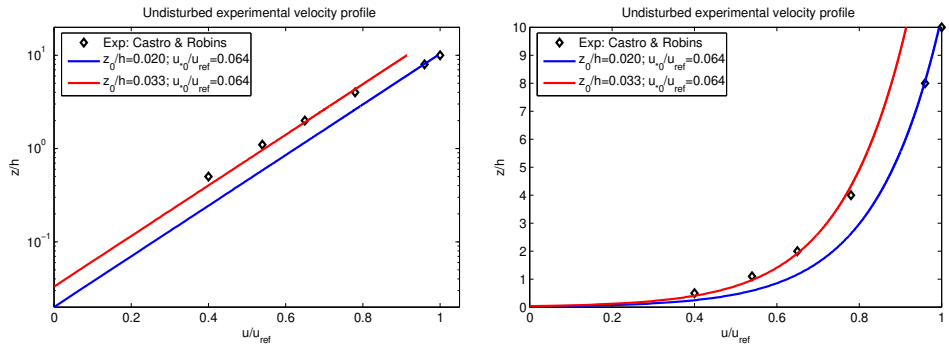

Figure 52. The undisturbed experimental velocity profile (diamonds) compared to different log-law fits. Left: logarithmic scale. Right: linear scale.

therefore be performed with the standard model constants for atmospheric flows (se table 1).

A windfield similar to the undisturbed windfield of the experiment needs to be generated by running a precursor. Since the precursor generates a near logarithmic velocity profile a logarithmic fit to the experimental data is necessary. Using the logarithmic velocity profile (38) and (48) the velocity and turbulence intensity near the wall normalized with a reference velocity can be written as,

$$\frac{\langle u \rangle}{u_{ref}} = \frac{1}{\kappa}\left(\frac{u_{*0}}{u_{ref}}\right)\ln\left(\frac{z}{h_c}\frac{h_c}{z_0}\right) \tag{100}$$

$$\frac{\langle k \rangle^{1/2}}{u_{ref}} = C_\mu^{-1/4}\left(\frac{u_{*0}}{u_{ref}}\right) \tag{101}$$

In order for the turbulence intensity to be the same for simulation and experiment the ratio u_{*0}/u_{ref} should be the same. For the experiment the reference velocity was taken at the top of the boundary layer, $u_{ref} = u(z = H)$. Fitting the logarithmic profile to the experimental data using $z_0/h_c = 0.02$ and $\langle u \rangle / u_{ref} = 1$ for $z = 10h_c$ it is found that $u_{*0}/u_{ref} = 0.064$ and the resulting logarithmic velocity profile is shown on figure 52 (blue line). As seen this logarithmic fit is quite poor. In order to capture the measured velocity better at cube-height, a larger surface roughness is needed. By increasing the the roughness length to $z_0/h_c = 0.033$ and keeping $u_{*0}/u_{ref} = 0.064$ a prober fit is achieved to a height of about $z/h_c = 5$ (see figure 52). This somewhat larger roughness length will be used for simulations. In atmospheric scale this would correspond to a roughness length of about $z_0 = 2m$.

Surface pressure measurements on the cube walls were performed during the experiment. In order to compare with simulations, the pressure coefficient, C_p, is defined

$$C_p = \frac{\langle p \rangle - \langle p_\infty \rangle}{\frac{1}{2}\rho {u_h}^2} \tag{102}$$

where $\langle p \rangle$ is the mean surface static pressure and $\langle p_\infty \rangle$ is the reference pressure measured at the inlet. Measurements of the streamwise turbulence intensity and velocity profiles were performed on the cube roof ($x/h_c = 0$) and at two downstream locations ($x/h_c = 1, x/h_c = 2$). The reference velocity, u_{ref}, used to normalize the velocity and turbulence intensity for the measurements is the upstream velocity at height, $z = 10h_c$. For simulations u_{ref} is the velocity that secures the logarithmic fit (see figure 52).

8.3 Numerical aspects

Computational mesh

Two meshes are necessary in order to perform simulations of the flow about a wall mounted cube. A precursor mesh and a successor mesh. As previously the precursor simulation generates the turbulent inflow for the actual cube simulation (the successor).

The cross-sectional plane of the precursor and successor meshes are identical in order to avoid spatial interpolation. Thereby the precursor flow can be used directly at the precursor inlet. The height of the computational domains has been chosen to $H = 10h_c$ where $h_c = 0.2m$ is the cube height. This is identical to the wind tunnel experiment, and should be adequate to avoid the influence of the top boundary on the local flow around the cube. Rectangular grids can be used for the simple geometry. Equidistant meshing is used in the height for the first 32 computational cells until cube height. From this height the cells are coarsened to a height from where constant mesh spacing ($\Delta = 0.03125m$) is applied. The domain width is $W = 32h_c$ and the transverse mesh stretching is similar to the one applied vertically. The domain widths are slightly smaller than used in the experiment, but the blockage ratio, defined as the ratio between the frontal area of the cube and of the tunnel cross section is only 0.003 (0.002 in the experiment). Therefore, we consider the near-cube flow unaffected by domain boundaries. A transverse plane of the successor mesh is seen to the left on figure 53.

In the streamwise direction the precursor uses equidistant grid spacing of 0.03125m and a domain length of $60h_c$. The recommended proportions of the precursor domain, 6H×4H×1H, is thereby nearly achieved. The constant spacing in the streamwise direction ensures a constant turbulent length scale (filter scale) of $\Delta = 0.03125m$ for the precursor. For the successor mesh, equidistant grid spacing is only used for the first 1m (32 cells) after the inlet ($x = -8h_c$) whereafter the cells are refined toward the cube. Since the successor mesh is refined in all directions near the cube, the near-cube filter scale decreases from $\Delta = 0.03125m$ to $\Delta = 0.00625m$. This fine mesh spacing is kept for about 4.5 cube-heights ($4.5h_c$) downstream whereafter the mesh spacing is coarsened towards the outlet ($x = 26h_c$). This provide a bufferzone between the outlet (specified as zero normal-gradient) and the cube. A streamwise section of the successor mesh is seen to the right on figure 53.

Using (43) with the standard model constants for atmospheric flows (table 1) it is found that the change from RANS to LES should happen at a height of

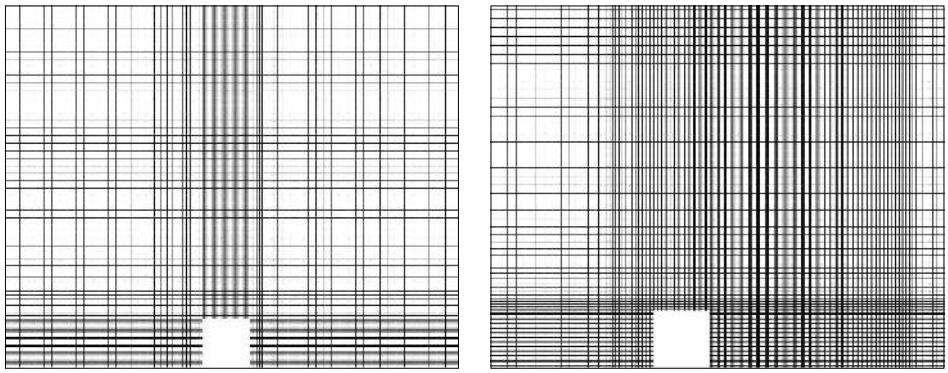

Figure 53. Part of the computational mesh used for the successor simulation. Left shows a cross-sectional plane (yz-plan) through the cube. Right, a streamwise plane (xz-plane) through the cube

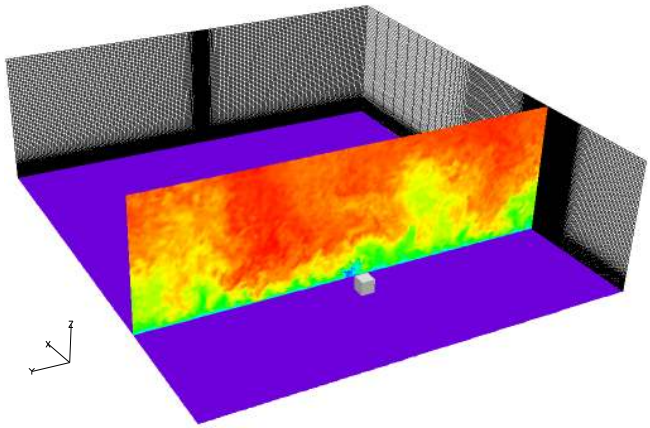

Figure 54. The cube successor mesh. A cross-sectional plane shows the instantaneous wind speed contours directly downstream of the cube

about $z_{ml} = 0.007m$. The height of the first near-wall cell for both precursor and successor is 0.00625m. Because the first near-wall cell is placed above the surface roughness, $z_0 = 0.0066m$, the total height is larger than z_{ml} and no RANS layer is formed. Thereby the logarithmic wall function, which relates the surface roughness to the surface stress does not come into play. This mistake could have been avoided by decreasing the height of the near-wall cells. To avoid the time consuming task of running a new precursor, the first near-wall cell has been forced to RANS instead. On figure 54 the computational domain of the successor mesh is seen and mesh details are found in table 18.

Table 18. Domain sizes and mesh details. The domains of sizes (L,W,H) are partitioned into (N_x,N_y,N_z) grid cells. z_1 is the average height of the first near-wall grid cell, and S is the maximum stretching ratio applied to the mesh near the wall. In the streamwise direction the successor mesh uses equidistant mesh spacings for the first 1m (32 cells) whereafter the cells are refined to $\triangle = z_1$ toward the cube. This fine mesh spacing is kept for about 4.5 cube-heights downstream whereafter the mesh spacing is coarsened towards the outlet.

Mesh	L [m]	W [m]	H [m]	N_x [-]	N_y [-]	N_z [-]	$\triangle$ [m]	S [-]	z_1 [m]
Cube successor	7.0	6.4	2.0	288	224	96	0.03125	1.00	0.00626
Cube precursor	12.0	6.4	2.0	384	224	96	0.03125	1.00	0.00626

Simulation parameters

In order to have a reference simulation, both RANS and LES simulations are run, using the same model constants. $C_\mu = 0.03$ is determined using (48) and the measured turbulence level of the undisturbed onset flow ($TKE/u_{*0}^2 = 5.3 - 6.6$). Simulations are performed with the standard model constants for atmospheric flows, se table 19.

Precursor simulations are run as channel flows with a streamwise pressure gradient of $\langle p \rangle / \partial x = -0.296 kgm^{-2}s^{-2}$ equivalent to $u_{*0} = 0.77ms^{-1}$ (55). The precursors are run until equilibrium flows for RANS and LES are achieved using a

time step of $\triangle t = 5 \cdot 10^4 s$. Since the successors are run with $\triangle t = 1.4 \cdot 10^{-4} s$, the time step of the precursor is changed accordingly before the generated windfield is stored. 2.8s of turbulence is stored (20000 time steps) and used as inflow for the successor simulation. The successor simulation is allowed 0.7s spin-up time before results are sampled over the last 2.1s.

Table 19. Model constants for simulations of the surface mounted cube. For RANS simulations $C_b = 0$

C_μ	$C_{\epsilon 1}$	$C_{\epsilon 2}$	σ_k	σ_ϵ	C_b	C_Δ
0.03	1.42	1.92	1.00	1.30	0.70	1.26

Table 20. Input parameters for surface mounted cube simulations used for both RANS and LES

Mesh	*Scheme*	z_0	$\triangle$t	u_{*0}
Cube	CDS4	0.0066m	0.00014s	$0.77 ms^{-1}$

8.4 Results

Inflow turbulence - precursor

The precursor results are shown on figure 55. Here it is seen that the RANS velocity profile is close to the targeted logarithmic profile with $u_{*0} = 0.77 ms^{-1}$. The LES profile, however, shows a clear speed-up in the transition region between the highly modeled wall region and the outer region. In the outer region the LES velocity profile is logarithmic with the correct slope, but with a too high velocity. The predicted friction velocity for LES is only $u_{*0} = 0.70 ms^{-1}$.

The reason for the speed-up must be due to the high drag. As seen, the velocity profile is correct at the near-wall cell - locked to RANS. The velocity shift is probably related to the ratio of $z_0/h_c \approx 3 \cdot 10^{-2}$ (proportional to the drag coefficient (73)). This ratio characterizes the degree of shearing at a height of interest. For comparison, the Askervein hill simulation was performed at $z_0/h_c \approx 0.03m/116m = 3 \cdot 10^{-4}$, i.e. a factor 100 smaller. For high values of z_0/h_c the bufferzone between the highly modeled wall region and the outer LES region moves closer to the surface for the same spatial resolution. Since the level of energy dissipation becomes very large near the surface the level of energy, which need to be re-injected by the stochastic backscatter model also increases. The simple backscatter model is clearly not capable of dealing with so high roughness levels.

Despite differences from the experimental onset flow, the generated velocity fields are used for the successor simulations. Using a reference velocity of $u_{ref} = 14.5 ms^{-1}$ for LES and $u_{ref} = 12.0 ms^{-1}$ for RANS the non-dimensional velocity fields match the measured onset flow reasonable well (see figure 56). As seen, however, the turbulence intensity for the LES simulation becomes much smaller than for the experiment.

Surface pressure

Figure 57 shows the pressure coefficient (102) on the cube surface along windward, roof and leeway side. The pressure coefficient (102) is made dimensionless with the mean onset velocity at cube height (LES: $u_h = 8.4 ms^{-1}$, RANS: $u_h = 6.6 ms^{-1}$). LES results are blue while RANS are red. The LES pressure distribution on the

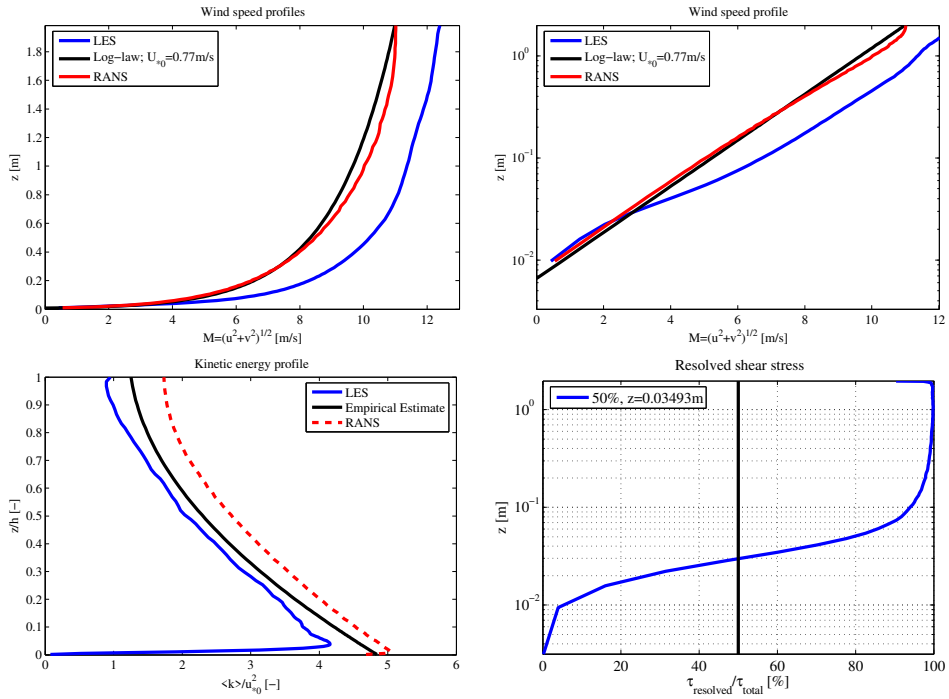

Figure 55. Precursor results for surface mounted cube. Top-left: Velocity profiles for RANS and LES compared to a logarithmic profile, $u_{*0} = 0.77ms^{-1}$. Top-right: Logarithmic plot of RANS and LES velocity profiles. Bottom-left: Profile of resolved and modeled turbulent kinetic energy for LES and RANS. The Empirical estimate by (88). Bottom-right: Amount of resolved shear stress for LES compared to the total.

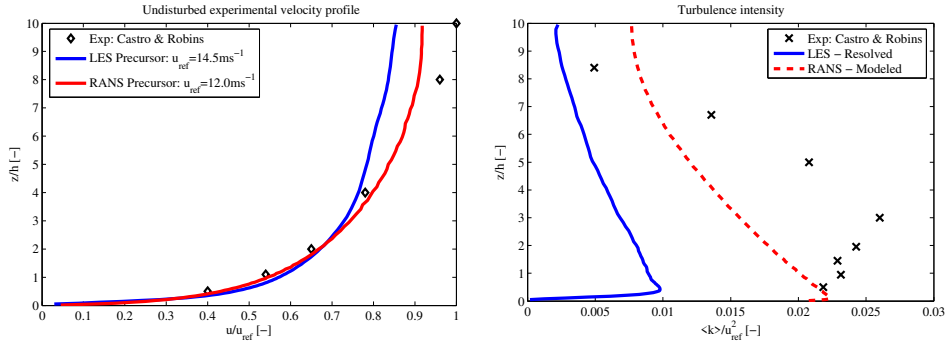

Figure 56. Precursor result for surface mounted cube normalized with reference velocity (RANS: $u_{ref} = 12.0ms^{-1}$, LES: $u_{ref} = 14.5ms^{-1}$). Left: Precursor velocity profiles for both RANS and LES fit measurements reasonable to about $z/h_c = 5$. Right: Turbulence intensity for RANS and LES compared with measurements.

windward side captures measurements very well, while RANS predicts a too high stagnation pressure. The height of the stagnation point is $z/h_c = 0.75$ and $z/h_c = 0.83$ for LES and RANS respectively.

For the experiment, the peak of the negative pressure on the roof exceeds the stagnation pressure on the windward side. This is to some degree reproduced by both RANS and LES. The pressure distribution from the experiment, however, recovers to a value close to zero along the roof and leeway side - this is not reproduced by simulations. The reason for this distinct underprediction may be

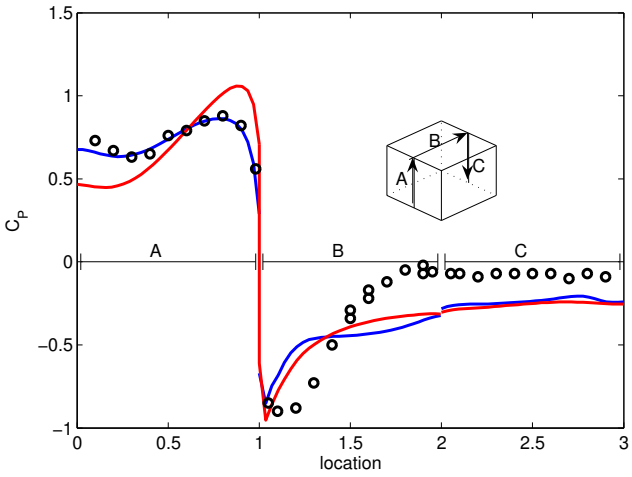

Figure 57. Surface pressure distribution along windward (A), roof (B) and leeway (C) side. LES results shown by blue lines, RANS by red lines

related to the conditions of the approach flow. Richards et al. [51] and Hoxey et al. [20] found that windward pressure was relatively unaffected by upstream conditions, while roof and leeway pressure was found to be very sensitive to the approach flow conditions. Generally, large variations in roof and lee side pressure distributions are found [51]. For uniform inflow the measured pressure distribution on the roof [11] is similar to simulation results.

Mean velocity

Figure 58,59 and 60 show mean flow velocity vectors at different planes for both RANS and LES simulations. Comparing the RANS and LES results, similarities but also differences are observed. On figure 58 the deceleration upwind of the cube is seen to cause a separation bubble or a horse-shoe vortex to form at the base of the cube. To clarify this, reverse flow is marked by blue velocity vectors. For the LES results the vortex extends about one cube height upstream, while it is smaller for RANS. On the lee side of the cube a wake region is observed with a marked velocity deficit extending several cube heights downstream. In this region a small recirculating region is observed for the LES results near the cube base similar to the one observed upstream. Differences in the wake region for LES and RANS are observed. For RANS one distinct separation bubble is observed, which extends from the trailing edge of the cube to about $2.2h_c$ downstream where it reattaches to the surface (estimated from velocity vectors). The wake recirculation length for LES is smaller, about $1.8h_c$, which is closer to $1.4h_c$ observed for cube in natural wind [49, 51].

For the experiment, the flow separates at the leading edge but reattaches again to the cube roof after a length of about $0.3h_c$. Figure 58 shows that for RANS the roof flow remain attached, while the LES flow separates near the leading cube edge and remain detached over the whole cube. The differences observed on the cube roof are probably due to the flow behavior being very dependent on the turbulence intensity, ($I =< k >^{0.5} / < u >$), of the onset flow. High mixing of the flow is achieved with high turbulence intensities, which leads to decreased reattachment lengths or even to the flow remaining attached to the roof. At about I=0.16 reattachment is observed experimentally [49] while at higher intensities no separation is observed (I=0.3). Since the LES simulations are performed with I=0.10 separation from the cube roof without reattachment is expected. Reattachment may be

observed intermittent but not in the mean. For the RANS simulation separation is not observed even though turbulence intensity is close to the experiment. It has been observed by several authors [50, 56, 72] that the $k-\epsilon$ RANS model is unable to predict the roof recirculation zone.

Figure 59 shows the velocity vectors for a horizontal slice near the cube base. Here it is again observed that the velocity deficit region in the cube wake is shorter for LES than RANS and that the horse-shoe vortex upstream of the cube is much stronger for LES. On the cube sides both RANS and LES predicts separation bubbles. For the plane shown, LES only predicts separation on one of the cube sides. This is due to the LES inflow being slightly asymmetric for the chosen average period.

Figure 60 shows the mean velocity vectors in a yz-slice at $x = h_c$. Here blue arrows denote negative w-velocity. It is seen that LES to a higher degree than RANS mixes high speed velocity from above the cube into the wake region. This may be the reason for shorter wake region for LES.

Comparison between measured and computed mean velocity profiles over the center of the cube ($x/h_c = 0$) and at two downstream locations ($x/h_c = 1$ and $x/h_c = 2$) are shown on figure 61. On the roof top RANS agrees well with measurements whereas LES agreement is less satisfactory due to the predicted separation. At x/h_c=1 LES and RANS gives similar results - they do not predict the high level of shear found in the measurements. For the LES data this must be related to incorrect velocity profile found on the cube top. Further downstream agreement is acceptable.

Turbulent kinetic energy

Measurement of the streamwise velocity fluctuation, u/u_{ref}, was performed during the experiment. This quantity cannot, however, be extracted from the $k-\epsilon$ RANS model. In order to compare RANS results with measurements we use an assumption of isotropy and instead compare the modeled turbulent kinetic energy to the measured fluctuation by $k^{0.5}/u_{ref} \approx u/u_{ref}$.

For LES the turbulence intensity of the onset flow is very low. However, since most turbulence in the wake of the cube is generated by shedding of vortices from the cube edges, the wake turbulence may be relatively independent on free stream turbulence. As seen on figure 62 this seems to be the case. LES predicts both the maximum turbulence intensity and the intensity level below cube height well. At some height above the cube only free stream turbulence exist why LES underpredicts in this region. RANS also captures the maximum intensity well, but over estimates the level below cube height. Only LES is able to estimate the quite narrow turbulence peaks of the measurements.

8.5 Closure

LES and RANS simulations of the flow about a surface mounted cube in a thick boundary-layer was conducted. Despite the simple geometry, the flow is highly complex with several vortical structures. The flow around bluff bodies are therefore good test cases when studying the turbulence model's ability to capture separated wake regions - regions also observed in atmospheric flows over complex terrain.

In order to generate turbulent inflow for the simulations, precursor simulations were run. Here, the difficulty in imposing experimentally-obtained inflow conditions for LES was learned. The turbulence model was found inadequate to model the very high levels of roughness of the experiment, and the generated wind field clearly lacked the high turbulence levels expected. Despite this discrepancy the generated velocity fields were used for cube simulations.

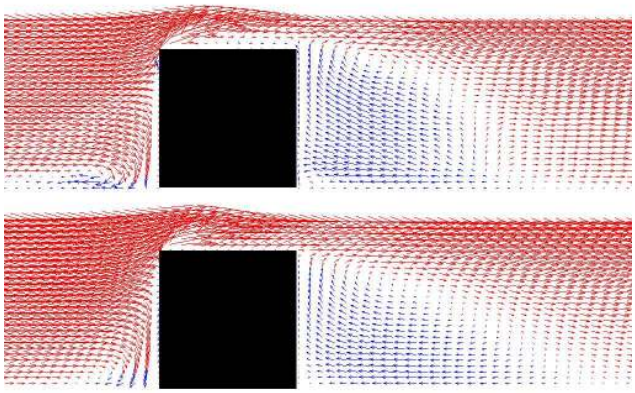

Figure 58. Slice in xz-plane ($y/h_c = 0.0$) for LES (top) and RANS (bottom). LES separates on the cube top while RANS remain attached.

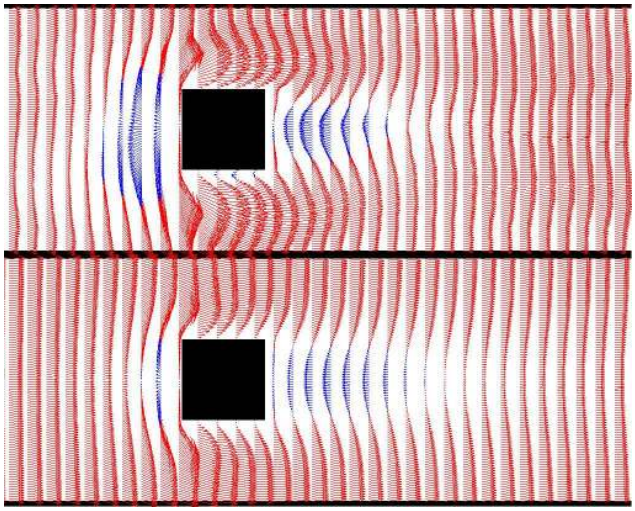

Figure 59. Slice in xy-plane near the cube base ($z/h_c = 0.008$), LES (top), RANS (bottom). The velocity deficit downstream extends further for RANS than LES.

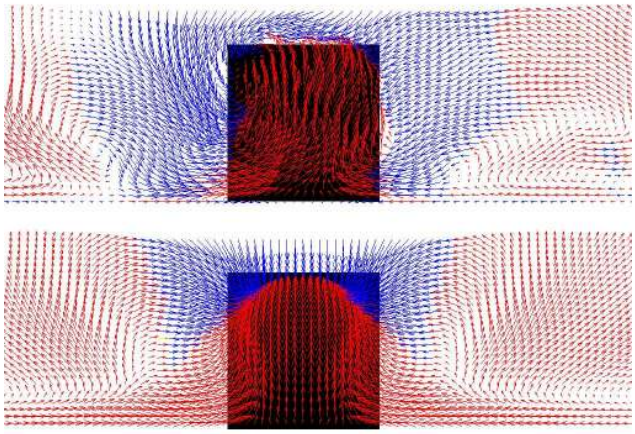

Figure 60. Slice in yz-plane ($x/h_c = 1.0$) for LES (top) and RANS (bottom). For LES, high speed flow is mixed down into the cube wake.

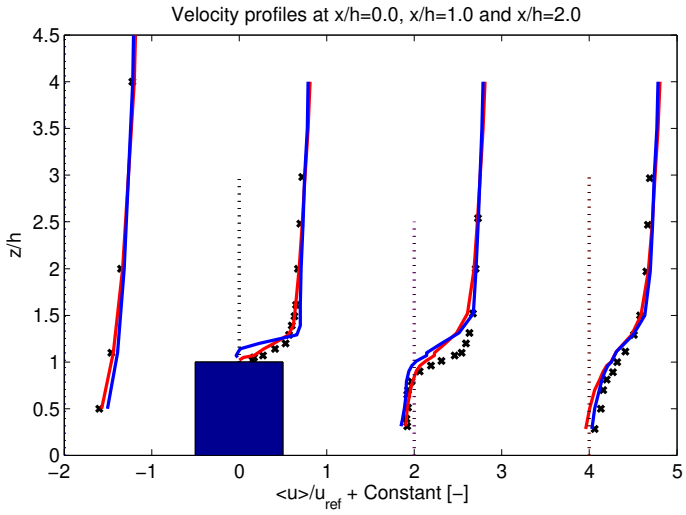

Figure 61. Velocity profiles at different values of x/h_c for $y/h_c = 0$. Crosses denote measurements while blue lines are LES results and red lines are from RANS. The constant added is -2.0 for the upstream profile, 0.0 for $x/h_c = 0.0$, 2.0 for $x/h_c = 1.0$ and 4.0 for $x/h_c = 2.0$.

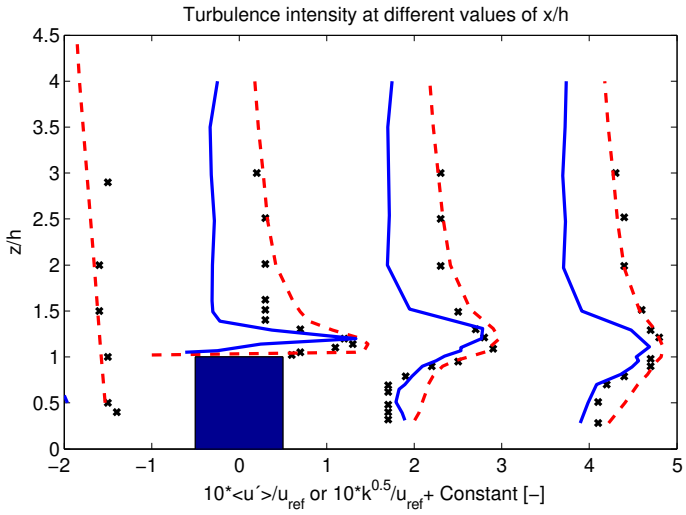

Figure 62. Turbulence intensity profiles from RANS (red lines) and LES (blue lines) compared with measurements (crosses). Profiles are taken at different values of x/h_c for $y/h_c = 0$. The constant added is -2.0 for the upstream profile, 0.0 for $x/h_c = 0.0$, 2.0 for $x/h_c = 1.0$ and 4.0 for $x/h_c = 2.0$.

For the successor simulations, RANS was shown to be able to reproduce the main flow features - the horse-shoe vortex at the cube base and the recirculation zones at the cube sides and wake. RANS did however fail to reproduce the roof separation and clearly overestimated the separation length downstream of the cube.

For LES increased turbulent mixing in the cube wake was observed compared to RANS. The increased mixing resulted in a reduced recirculation length for LES - better agreeing with measurements. Further more, the turbulence intensity and narrow turbulence peaks of the measurements were predicted well with LES. Duo to low upstream turbulence roof reattachment was not observed for LES. The windward pressure coefficient, which is relative independent on the conditions of

the onset flow, was very well predicted by LES. Both RANS and LES, however, underestimated the pressure at the cube top. Again, this may be explained by the low turbulence intensity of the onset flow.

From simulations results it can be concluded that the LES model is able to capture the physics of separated regions and that LES produce time-dependent and three-dimensional flow information, such as the Reynolds stresses, that cannot be extracted from RANS.

9 Conclusions

9.1 The developed turbulence model

This report has dealt with the development and validation of a turbulence model capable of simulating atmospheric flow over terrain. The main applications of interest are related to siting and load estimation of wind turbines, why the aim was a LES model capable of predicting realistic turbulent wind fields in complex terrain.

The finite-volume code, Ellipsys3D, which is based on the incompressible RANS-equations was the fundament for the work. By interpreting the finite-volume discretization of the NS-equation as a spatial filter, it was shown that LES- and RANS-equations are identical - only the turbulence modeling is different.

The high Reynolds number $k-\epsilon$-model is traditionally used for RANS simulations of flow over terrain. The model have universal applicability and have good numerical stability. Furthermore, it provides a method for dealing with rough surfaces - through the use of wall-functions. Therefore, it seemed natural to use this model as starting point for the development of a LES model. Inspired by the simplicity of DES, the $k-\epsilon$ RANS model was changed to a LES model, by simply changing the turbulent length scale build into $k-\epsilon$-equations. Combining the two models with a simple switch, the RANS model, with build-in wall function, was used near the rough surfaces thereby acting as boundary condition for LES used away from the wall. The model is solved on a single grid and the switch from RANS to LES happens automatically - it does not need to be predefined. Mesh generation is therefore easy - the model itself determines wether a region should be handled by LES or RANS. For instance, the near-wall mean velocity can be resolved using grid cells of very high aspect ratio, because the model detects this and switches to RANS.

In order to improve results a backscatter model was implemented. The model breaks up the unphysical turbulent structures from the RANS region and generates Reynolds stress carrying structures. Applying the backscatter model the velocity mismatch between the RANS and LES region was diminished. Both backscatter and turbulence model were designed to be independent on the value of C_μ. Thereby C_μ can be chosen following normal $k-\epsilon$ RANS practice - ensuring the correct level of modeled turbulent kinetic energy. By simulating decaying isotropic turbulence, two sets of model constants where derived, one for industrial flows and one for atmospheric flows. Furthermore, the LES model was shown to behave like a Smagorinsky model.

The traditional high Reynolds number $k-\epsilon$ RANS uses the Boussinesq hypothesis and assumes the turbulent stresses to be a product of the fluid strain and the isotropic eddy-viscosity. The Boussinesq hypothesis is invalid for flows where $uu \neq vv \neq ww$. The new LES model uses the same hypothesis, but since it only applies to the small isotropic subgrid-scale, the actual turbulence modeling is of minor importance. In order to get reliable results, however, the numerical technique was shown to be important. Imposing realistic and even experimentally-obtained inflow conditions was found extremely difficult. An inflow method was therefore implemented where a fully developed wind field from a separate precursor simulation could be used as inflow for the successor simulation. It was found that the flow equations should be descretized using central schemes and that the CFL-number should be $CFL = 0.25$ or smaller, for the second order time stepping algorithm used. The importance of the computational domain's outer dimensions was also demonstrated and the computational cost for the precursor as function of grid spacing was estimated.

9.2 Computed test cases

Four test cases was simulated in order two validate the behavior the turbulence model.

Simulation of decaying homogeneous and isotropic turbulence was the first test case. Simulation was performed in order to calibrate the turbulence model. It was found that only central schemes should be used for discretisation of the convective terms in the NS-equations. The turbulence model was able to simulate decaying turbulence, although results were sensitive to the initial turbulence field.

Secondly, simulations of the ABL over flat terrain was performed, with varying values of roughness. It was shown, that if C_Δ is correctly chosen, the turbulence model works like a Smagorinsky model - dissipating energy at the correct level, independently of C_μ. A big advantage with the proposed turbulence model is that it can be run in both RANS and LES mode. This was demonstrated - RANS and LES mean velocity profiles showed good agreement. LES results showed clear logarithmic velocity profiles with a smooth transition from the near-wall RANS-layer to the outer LES-layer. Generally, LES was able to reproduce the statistics from similarity theory.

Simulation of the flow over the Askervein hill was also performed and compared to measurements of Taylor and Teunissen [67]. RANS was shown to reproduce mean velocity speed-up, though slightly under-predicting at hill top. LES predicted the hill top speed-up well, but estimated a separation region in the lee-side of the hill. Measurement only showed intermittent separation. The turbulent kinetic energy on the lee-side was strongly under-predicted for RANS but well predicted for LES.

Simulation of flow about a surface mounted cube was conducted in order to study the turbulence model's ability to capture separated shear layers. Results were compared to measurements of Castro and Robins [11]. For this test case the precursor had difficulties in producing the desired onset wind for the LES simulation. The model was unable to produce the turbulent drag of the very rough wall. This resulted in an onset flow with too low turbulence intensity compared to measurements. Despite the discrepancies the generated velocity field was used for the cube simulations. Simulations showed that the LES turbulence model was able to capture the physics of the wake region. LES was able to predict the recirculation length and turbulence intensity better than RANS in this region.

9.3 Future work

Even though good results have been achieved, further atmospheric test cases should be performed. For the two terrain simulations presented, i.e. flow over the Askervein hill and about the wall mounted cube, the LES model have been prone to estimate flow separation. For the wall mounted cube, the roof separation without reattachment can be explained by the low turbulence level of upstream flow. Further test cases would, however, clarify this.

The ability to simulate different levels of roughness has been demonstrated. For very large values of roughness, however, the turbulence model has problems generating the required drag. A canopy model as suggested by Brown et al. [9], which enhances the near wall stress could be a solution.

Only neutrally stratified flows have been considered in this work. In order to expand the range of application, the turbulence model could be developed to allow non-neutral flows.

Dansk resumé

Dansk titel: "Large-Eddy Simulering af atmosfærisk vind over komplækst terræn"
Forfatter: Andreas Bechmann

Introduktion

En grundig forståelse af vinden i det atmosfæriske grænselag er vigtigt for en lang række praktiske problemer. Strukturelle belastninger på bygninger, forureningsspredning, placering af vindmøller og landbrugsproduktion er blot få af de omrder, der er afhængige af pålidelige vejr forudsigelser. Når en vindmølle skal opstilles, er den turbulente vind af afgørende betydning for den elektriske produktion og strukturelle belastning. Da landskabets topografi kan have kritisk betydning for vindens karakter, er det vigtigt med en forståelse af de lokale vindforhold - præcis der hvor vindmøllen skal placeres.

Lokale vindmålinger er hovedsagligt fortrukket; men ofte kan computermodeller, der simulerer vindforholdene, være et udmærket supplement. Vind simuleringer giver mulighed for parameter undersøgelser og leverer en detaljeret beskrivelse af vinden. Ofte er det sparsomt med vindmålinger, og ingeniører er da afhængige af computermodeller. For landskab bestående af bakker med lille stejlhed og små ruhedselementer, findes der modeller, som kan levere de nødvendige vind informationer til en belastningsanalyse; men sådanne modeller er upræcise for komplekst terræn. Da netop vindmøller tit placeres i komplekst terræn, er det vigtigt med en robust model, der kan klare disse forhold - udviklingen af en sådan model var målet med dette arbejde.

Baggrund for arbejdet

Projektet foregik i samarbejde mellem Institut for Mekanik, Energi og Konstruktion ved DTU og Afdelingen for Vindenergi ved RISØ og var en direkte videreudvikling af modeller allerede benyttet i forbindelse med strømning over komplekst terræn. CFD (Numerisk Fluid Mekanik) koden EllipSys3D udviklet af Michelsen [37, 37] og Sørensen [56] er grundlaget for arbejdet. EllipSys3D koden blev udviklet specifikt til at beregne strømninger over terræn; men benyttes i dag til en lang række formål. Koden er en inkompressibel 3D løser baseret på de Reynoldsmidlede Navier-Stokes ligninger (RANS). For terræn beregninger modelleres turbulens med $k - \epsilon$ modellen, og koden benytter krumme beregningsnet, som kan tilpasses det underliggende terræn. Koden er paralleliseret ved anvendelse af MPI (message passing interface), hvilket er vigtigt for de beregningstunge simulationer foretaget i dette arbejde.

I en lang række opgaver inden for CFD benyttes turbulensmodeller, der bygger på RANS-ligningerne. Til mange formål er RANS tilstrækkeligt og gennemprøvet; men i andre tilfælde, eksempelvis for separerede strømninger, fjerner de tidsmidlede ligninger for meget information om de turbulente strukturer og giver et forkert billede af strømningen. Vinden over komplekst terræn består i stor grad af områder domineret af separation, hvorfor RANS i disse tilfælde er utilstrækkelig. Ydermere, hvis de dynamiske belastninger på en vindmølle skal bestemmes, er det i sagens natur nødvendigt med en tidstro model. Det blev derfor besluttet at udvikle en turbulens model til EllipSys3D baseret på Large-Eddy Simulering (LES). Modsat RANS, som giver det tids-midlede vindfelt, er LES i stand til at give et tidstro vindfelt, hvor den største del af turbulensen er opløst. På trods af at metoden er beregningsmæssig tung, giver metoden en overvældende mængde information om strømningen, hvilket kan bruges i en lang række applikationer.

Den udviklede turbulens model

Høj Reynolds tal $k-\epsilon$ RANS modellen bliver traditionelt benyttet til at simulere vinden over terræn. Modellen er velafprøvet, numerisk stabil og kan benyttes til strømninger over ru overflader ved hjælp af logaritmelovrandbetingelser. Det virkede derfor naturligt at benytte denne model som udgangspunkt i udviklingen af en LES model. Inspireret af den simple DES-model, blev $k-\epsilon$ RANS modellen ændret til en LES model ved at udskifte den karakteristiske længdeskala, som er indbygget i $k-\epsilon$ ligningerne. Med en simpel funktion blev de to modeller kombineret således at RANS modellen, med indbygget logaritmelov, benyttes nær ru overflader og virker som randbetingelse for LES modellen, som aktiveres et lille stykke fra væggen. Den kombinerede model løses på et enkelt beregnings net, og skiftet mellem RANS og LES skal ikke defineres på forhånd - det sker automatisk. Netgenerering er derfor nemt, da modellen selv bestemmer om et område skal behandles med RANS eller LES. Er et område f.eks. for groft opløst til LES, opdager modellen selv dette og skifter til RANS.

For at forbedre resultaterne blev en "backscatter" model implementeret. Modellen forbedrer hastighedsfeltet ved at ødelægge de ufysiske turbulente hvirvler, som findes i RANS området - dermed opnås en "glat" overgang mellem RANS og LES området. Den udviklede turbulens og "backscatter" model blev konstrueret til at være uafhængig af modelkonstanten C_μ. Dette betyder, at C_μ kan vælges frit. C_μ kan f.eks. vælges således, at det modellerede turbulens niveau i RANS området passer med eksperimentelle målinger. Turbulens modellen blev kalibreret ved at simulere henfaldende isotropisk turbulens og modelkonstanter til industrielle og atmosfæriske strømninger blev udledt. Det blev også vist, at turbulens modellen opfører sig som en Smagorinsky model. Da RANS laget i den nye turbulens model ofte er meget tyndt, betegnes den nye model blot en LES model.

Høj Reynolds tal $k-\epsilon$ RANS modellen benytter Boussinesq' approksimationen, som antager, at forskydningsspændingerne er lig produktet af den isotropiske eddy-viskositet og strømnings deformationen. Boussinesq' approksimationen er ugyldig for strømninger hvor $uu \neq vv \neq ww$. Den nye model benytter stadig approksimationen; men eftersom at hovedparten af forskydningsspændingerne er opløste, er denne antagelse mindre betydelig. Mere betydningsfuld er de numeriske metoder, som benyttes til løsning af ligningssystemet. F.eks. er det meget vigtig at påtrykke et realistisk hastighedsfelt ved indløbsrenden til beregningsnettet. Derfor blev der under arbejdet udviklet en metode, hvor et fuldt udviklet hastighedsfelt fra en separat LES simulation kunne benyttes som indløbsbetingelse til terræn simuleringer. Vigtigheden af et beregningsnet der både opløser de største og mindste turbulente strukturer blev ligeledes undersøgt, og beregningstiden for en LES simulering blev estimeret.

Resultater

For at verificere turbulens modellen blev fire testtilfælde beregnet.

Henfaldne isotropisk turbulens var det første testtilfælde. Beregningen blev hovedsagligt foretaget for at kalibrere turbulens modellen. Turbulens modellen viste sig i stand til at simulere henfaldne turbulens; men resultaterne var afhængige af startbetingelserne. Beregningen viste desuden, at LES kun bør foretages med centrale skemaer.

Det andet testtilfælde var simulering af neutralt stratificeret atmosfæriske grænselag, som blev foretaget med forskellige overflade-ruheder. Det blev vist, at turbulens modellen virker som en Smagorinsky model, og at den dissiperer turbulent energi uafhængigt af C_μ - forudsat at C_Δ vælges korrekt. En stor fordel ved den udviklede turbulens model er, at den kan foretage både traditionelle RANS

beregninger samt LES beregninger. Dette blev illustreret, og god overensstemmelse mellem middel hastighedsprofilerne for RANS og LES blev fundet. LES var i stand til at skabe det forventede logaritmiske hastighedsprofil - med en glat overgang mellem det kraftigt modellerede væg-lag og det ydre lag. Generelt set var LES i stand til at genskabe resultater opserveret i atmosfæriske målinger.

Strømningen over Askervein bakken blev også beregnet, og resultaterne blev sammenlignet med målinger af Taylor og Teunissen [67]. RANS var i stand til at genskabe den målte speed-up værdi, undtagen nær toppen af bakken hvor værdien var underestimeret. LES bestemte den korrekte hastighed på toppen af bakken; men forudså et konstant separeret område bag bakken. I målingerne optræder separation kun uregelmæssigt. RANS underestimerede turbulensintensiteten nedstrøms for bakken, hvorimod LES ramte målingerne fint.

Det sidste testtilfælde var strømningen over en terning. Dette testtilfælde blev valgt for at undersøge turbulens modellens evner i separerede områder. Resultaterne blev sammenlignet med vindtunnel målingerne af Castro og Robins [11]. For dette test tilfælde havde turbulens modellen problemer med at skabe vindfeltet, der skulle benyttes som indløbsbetingelse. Modellen var ikke i stand til generere forskydningsspændingen svarende til væggens meget store ruhedsværdi. Resultatet blev et indløbshastighedsfelt med mindre turbulensintensitet end eksperimentet. På trods af denne uoverensstemmelse var LES modellen i stand til at beskrive det separerede område bag terningen godt. Separationslængden og turbulensintensiteten for LES viste sig i god overensstemmelse med målingerne.

Fremtidigt arbejde

På trods af gode numeriske resultater bør flere testtilfælde beregnes. Ud fra beregningerne af strømningen over Askervein bakken og terningen kunne det tyde på, at den udviklede LES model har en for stor tilbøjelighed til forudsige separation. For testtilfældet med terningen, kan den beregnede separation på toppen af terningen skyldes det lave turbulens niveau i vindfeltet opstrøms. Flere testtilfælde ville dog belyse problematikken.

Turbulens modellen var i stand til at simulere varierende overflade ruheder. For meget store ruheder havde modellen dog vanskeligheder. En skov-model der genererer ekstra forskydningsspænding, som foreslået af Brown [9], kunne være en løsning. For at udvide modellens anvendelsesområde kunne det også være interessant at udbygge modellen, så stratificerede strømninger kan håndteres.

References

[1] A. Andren, A. Brown, J. Graf, C.H. Moeng, P.J. Mason, F.T. Nieuwstadt, and U. Schumann. Large-eddy simulation of a neutrally stratified boundary layer: A comparison of four computer codes. *Quart. J. R. Met. Soc.*, 120: 1457–1484, 1994. 41, 56

[2] S.P. Arya. *Introduction to Micrometeorology"*, volume 79. Academic Press, International Geophysics Series, 2001. ISBN 0-12-059354-8. 2

[3] F. Baetke and H. Werner. Numerical simulation of turbulent flow over surface-mounted obstacles with sharp edges and corners. *Journal of wind engineering and industrial aerodynamics*, 35:129–147, 1990. 72

[4] E. Balaras, C. Benocci, and U. Piomelli. Two-layer approximate boundary conditions for large-eddy simulations. *AIAA paper*, 34(6):1111-1119, 1996. 10, 15

[5] J. Bardina, J.H. Ferziger, and W.C. Reynolds. Improved subgrid scale models for large eddy simulations. *AIAA paper*, 80-1357, 1980. 11

[6] F. Bertagnolio, N.N. Sørensen, and F. Rasmussen. New insight into the flow around a wind turbine airfoil section. *Journal of Solar Energy Eng.*, 127: 214–222, 2005. 2

[7] J. Boussinesq. Thorie de l'coulement tourbillant. *Mm. prs. par div. savants l'Acad. Sci. Paris*, 23:46-50, 1877. 11

[8] R.A. Brost, J.C. Wyngaard, and D. Lenschow. Marine stratocumulus layers. part II: turbulence budgets. *J. Atmos. Sci.*, 39:818–836, 1982. 44

[9] A.R. Brown, J.M. Hobson, and N. Wood. Large-eddy simulation of neutral turbulent flow over rough sinusoidal ridges. *Boundary-Layer Meteorology*, 98: 411–441, 2001. 85, 88

[10] F.A. Castro, J.M.L.M. Palma, and A. Silva Lopes. Simulation of the Askervein flow. part 1: Reynolds Averaged Navier-Stokes equations ($k-\epsilon$ turbulence model). *Boundary-Layer Meteorology*, 107:501–530, 2003. 61, 62, 68

[11] I.P. Castro and A.G. Robins. The flow around surface-mounted cube in a uniform and turbulent streams. *J. Fluid Mech.*, 79:307–335, 1977. 72, 73, 79, 85, 88

[12] D. R. Chapman. Computational aerodynamics, development and outlook. *AIAA paper*, 17:1293–313, 1979. 14

[13] F.K. Chow and R.L. Street. Evaluation of turbulence models for large-eddy simulations of flow over the Askervein hill. *16th Symposium on Boundary Layers and Turbulence, American Meteorological Society*, Paper 7.11, 2005. 61, 62

[14] G. Comte-Bellot and S. Corrsin. Simple eulerian time correlation of full- and narrow-band velocity signals in grid-generated 'isotropic' turbulence. *J. Fluid Mech.*, 48:273–337, 1971. 32, 33

[15] L. Davidson and S. Dahlstrom. Hybrid LES-RANS: An aproach to make LES applicable at high Reynolds number. *Int. J. of Comp. Fluid Dynamics*, 19: 415–427, 2005. 10, 15

[16] J. W. Deardorff. Stratocomulus-capped mixed layers derived from a three-dimensional model. *Boundary-Layer Meteorology*, 18:495–527, 1980. 12

[17] J.H. Ferziger and M. Peric. *Computational Methods for Flud Dynamics*. Springer, Germany, 3rd edition, 2002. ISBN 3-540-42074-6. 72

[18] S. Ghosal. An analysis of numerical errors in large-eddy simulations of turbulence. *Journal of Computational Physics*, 125:187–206, 1996. 22

[19] S.E. Gryning, A.A.M. Holtslag, S.J. Irwin, and B. Sivertsen. Applied dispersion modelling based on meteorological scaling parameters. *Atmospheric Environment*, 21(1):79–89, 1987. 43, 44

[20] R.P. Hoxey, P.J. Richards, and J.L. Short. A 6m cube in an atmospheric boundary layer flow. Part 1. full-scale and wind-tunnel results. *Wind and Structures*, 5:165–176, 2002. 72, 79

[21] R.I. Issa. Solution of implicitly discretized fluid flow equations by operator-splitting. *Journal of Computational Physics*, 62:40–65, 1986. 21

[22] J. Johansen and N.N. Sørensen. Airfoil characteristics from 3D CFD rotor computations. *Wind Energy*, 7:283–294, 2004. 2

[23] J.C. Kaimal and J.J. Finnigan. *Atmospheric Boundary Layer Flows*. Oxford University Press, 1994. ISBN 0-19-506239-6. 2

[24] P.K. Khosla and S.G. Rubin. A diagonally dominant second-order accurate implicit scheme. *Computers Fluids*, 2:207–289, 1974. 23

[25] A.G. Kravchenko and P. Moin. On the effect of numerical errors in large eddy simulations of turbulent flows. *Journal of Computational Physics*, 131: 310–322, 1997. 22, 56

[26] B.E. Launder and D.B. Spalding. The numerical computation of turbulent flows. *Comput. Meths. Appl. Mech. Eng.*, 3:269–289, 1974. 2, 3, 10, 12, 17, 18, 44

[27] A. Leonard. Energy cascade in large-eddy simulations of turbulent fluid flows. *Adv. in Geophys.*, 18:237–248, 1974. 7, 8

[28] M. Lesieur and O. Metais. New trends in large eddy simulations of turbulence. *Annual Review of Fluid Mechanics*, 28:45, 1996. 6

[29] D.C. Leslie and G.L. Quarini. The application of turbulence theory to the formulation of subgrid modelling procedures. *J. Fluid Mech.*, 91:65–91, 1979. 16

[30] D.K. Lilly. The representation of small-scale turbulence in numerical simulation experiments. *Proceedings of the Tenth IBM scientific computing symposium on environment sciences*, pages 195–210, 1967. Thomas J. Watson Research Center, Yorktown Heights. 13

[31] T.S. Lund. The use of explicit filters in large eddy simulation. *Computers and Mathematics with Applications*, 46:603–616, 2003. 23

[32] J. Mann. Wind field simulation. *Prob. Engng. Mech.*, 13(4):269–282, 1998. 35, 39

[33] R. Martinuzzi and C. Tropea. The flow around surface-mounted, prismatic obstacles placed in fully developed channel flow. *Journal of Fluids Engineering*, 115:85–92, 1993. 72

[34] P.J. Mason. Large-eddy simulation of the convective atmospheric boundary layer. *J. Atmos. Sci.*, 46:1492–1516, 1989. 41

[35] P.J. Mason. Large-eddy simulation: A critical review of the technique. *Quart. J. R. Met. Soc.*, 120:1–26, 1994. 6

[36] P.J. Mason and D.J. Thomson. Stochastic backscatter in large-eddy simulations of boundary layer. *J. Fluid Mech.*, 24:51–78, 1992. 16, 17, 41, 51

[37] J.A. Michelsen. Basis3d - a platform for development of multiblock PDE solvers. Technical report AFM 92-05, Technical University of Denmark, 1992. 2, 5, 21, 86

[38] J.A. Michelsen. Block structured multigrid solution of 2D and 3D elliptic PDE solvers. Technical report AFM 94-06, Technical University of Denmark, 1994. 2, 5, 21

[39] R.E. Mickle, N.J. Cook, N.O. Jensen, J.R. Salmon, P.A. Taylor, G. Tetzlaff, and H.W. Teunissen. The askervein hill project: Vertical profiles of wind and turbulence. *Boundary-Layer Meteorology*, 43:143–169, 1988. 63

[40] C.H. Moeng. A large-eddy-simulation model for the study of planetary boundary-layer turbulence. *J. Atmos. Sci.*, 41(13):2052–2062, 1984. 12, 41

[41] F.T.M. Nieuwstadt and R.A. Brost. The decay of convective turbulence. *J. Atmos. Sci.*, 43:532–546, 1986. 41

[42] N.V. Nikitin, F. Nicoud, B. Wasistho, K.D Squires, and P.R. Spalart. An approach to wall modeling in large-eddy simulation. *Phys. Fluid*, 12:1629–1632, 2000. 15, 41, 51

[43] H.A. Panofsky and J.A. Dutton. Atmospheric turbulence models and methods for engineering applications. *John Wiley and Sons, New York*, 1984. 17

[44] P. Piomelli and E. Balaras. Wall-layer models for large-eddy simulations. *Annu. Rev. Fluid Mech.*, 34:349–374, 2002. 14

[45] P. Piomelli, E. Balaras, H. Pasinato, K.D. Squires, and P.R. Spalart. The inner-outer layer interface in large-eddy simulations with wall-layer models. *Int. J. Heat and Fluid Flow*, 24:538–550, 2003. 17, 41, 49

[46] S.B. Pope. *Turbulent Flows*. Cambridge Univ. Press, Cambridge, England, U.K., 2000. 6

[47] G.D. Raithby, G.D. Stubley, and P.A. Taylor. The Askevein Hill project: A finite control volume prediction of three-dimensional flows over the hill. *Boundary-Layer Meteorology*, 39:247–267, 1987. 17

[48] C.M. Rhie. *A numerical study of the flow past an isolated airfoil with separation*. Ph.d. thesis, University of Illinois, 1981. 21

[49] P.J. Richards and R.P. Hoxey. Flow reattachment on the roof of a 6 m cube. *Journal of Wind Engineering*, 94:77–99, 2006. 72, 79

[50] P.J. Richards and A.D. Quinn. A 6 m cube in an atmospheric boundary layer flow. Part 2 computational solutions. *Wind and Structures*, 5:177–192, 2002. 72, 80

[51] P.J. Richards, R.P. Hoxey, and L.J. Short. Wind pressures on a 6 m cube. *Journal of Wind Engineering*, 89:1553–1564, 2001. 72, 79

[52] L.F. Richardson. *Weather prediction by numerical process*. Cambridge: Cambridge University Press, 1922. 10

[53] A.G. Robins and I.P. Castro. A wind tunnel investigation of plume dispersion in the vicinity of a surface mounted cube - i. the flow field. *Atmospheric Environment*, 11:291–297, 1977. 72, 73

[54] P. Sagaut. *Large Eddy Simulation for Incompressible Flows*. Springer-Verlag, Heidelberg, Germany, 2001. 6, 7

[55] J Smagorinsky. General circulation experiments with the primitive equations: 1.the basic experiment. *Mon. Weather Rev.*, 91:99–164, 1963. 4, 13

[56] N.N. Sørensen. General purpose flow solver applied to flow over hills. Technical Report Risø-R-827(EN), Risø National Lab., Roskilde, Denmark, 1995. 2, 5, 15, 21, 61, 62, 64, 66, 68, 72, 80, 86

[57] N.N. Sørensen. HypGrid2D—a 2-D mesh generator. Technical report, Risø-R-1035(EN), Risoe National Laboratory, 1998. 29, 64

[58] N.N. Sørensen and J.A. Michelsen. Drag prediction for blades at high angle of attack using CFD. *Journal of Solar Energy Eng.*, 126:1011–1026, 2004. 2

[59] N.N. Sørensen, J.A. Michelsen, and J.A. Schreck. Navier-Stokes prediction of the NREL phase VI rotor in the NASA Ames 80 ft $\times$ 120 ft wind tunnel. *Wind Energy*, 5:151–169, 2002. 2

[60] P.R. Spalart. Trends in turbulence treatments. *AIAA paper*, 2306, 2000. 29

[61] P.R. Spalart, W-H. Jou, M. Strelets, and S.R. Allmaras. Comments on the feasibility of LES for wings, and on a hybrid RANS/LES approach. *1st AFOSR Int. Symp. Eng. Turb. Modelling and Measurements, May 24-26, Corsica*, 1997. 4, 10, 13, 15, 27, 41

[62] R.B. Stull. *An introduction to boundary layer meteorology*. Kluwer Academic Publishers, 1988. ISBN 9022727694. 2, 6, 43, 44

[63] P.P. Sullivan, J.C. McWilliams, and C.-H. Moeng. A subgrid-scale model for large-eddy simulation of planetary boundary layer. *Boundary-Layer Meteorology*, 71:247–276, 1994. 41, 51

[64] G.I. Taylor. The spectrum of turbulence. *Proc. R. Soc. London, Ser. A*, 164, 476, 1938. 33

[65] P.A. Taylor and H.W. Teunissen. The askervein hill project: Overview and background data. *Boundary-Layer Meteorology*, 39:15–39, 1987. 61, 63

[66] P.A. Taylor and H.W. Teunissen. Askervein '82: Report on the september/october 1982 experiment to study boundary-layer flow over askervein, south uist. *Atmos. Environ. Service, Downsview, Ontario*, Technical Report MSRB-83-8, 1983. 61, 62

[67] P.A. Taylor and H.W. Teunissen. The askervein hill project: Report on the sept./oct. 1983, main field experiment. *Atmos. Environ. Service, Downsview, Ontario*, Technical Report MSRB-84-6, 1984. 61, 62, 63, 67, 85, 88

[68] T.G. Thomas and J.J.R. Williams. Simulation of skewed turbulent flow past a surface mounted cube. *Journal of wind engineering and industrial aerodynamics*, 81:347–360, 1999. 72

[69] A. Travin, M. Shur, and M. Strelets. Physical and numerical upgrades in detached-eddy simulation of complex turbulent flows. *412 EUROMECH colloqvium on LES of complex transitional and turbulent flows, Munich*, Oct. 2000. 13, 15, 38

[70] O. Undheim, H.I. Andersson, and E. Berge. Non-linear, microscale modelling of the flow over Askervein hill. *Boundary-Layer Meteorology*, 120:477–495, 2006. 61, 62

[71] N. Wood. Wind flow over complex terrain: a historical perspective and the prospect for Large-Eddy modelling. *Boundary-Layer Meteorology*, 96:11–32, 2000. 3

[72] N.G. Wright and G.J. Easom. Non-linear $k - \epsilon$ turbulence model results for flow over a building at full-scale. *Applied Mathematical Modelling*, 27: 1013–1033, 2003. 72, 80

[73] A. Yakhot, H. Liu, and N. Nikitin. Turbulent flow around a wall-mounted cube: A direct numerical simulation. *Int. J. Heat and Fluid Flow*, 2006. In press. 72

[74] O. Zeman and N.O. Jensen. Modification of turbulence characteristics in flow over hills. *Quart. J. R. Met. Soc.*, 113:55–80, 1987. 17

[75] S.S. Zilitinekevich and I.N. Esau. Resistance and heat-transfer laws for stable and neutral planetary boundary layers: Olde theory advanced and re-evaluated. *Quart. J. R. Met. Soc.*, 131:1863–1892, 2005. 44

Risø's research is aimed at solving concrete problems in the society.

Research targets are set through continuous dialogue with business, the political system and researchers.

The effects of our research are sustainable energy supply and new technology for the health sector.